Behaviour of Reduced-Scale Reinforced Concrete Masonry Shear Walls and Components

BY

KEVIN J. HUGHES

B. Eng.

A Thesis

Submitted to the School of Graduate Studies

In Partial Fulfillment of the Requirements

For the Degree

Master of Applied Science

McMaster University

MASTER OF APPLIED SCIENCE (2010)

(CIVIL ENGINEERING)

McMaster University

Hamilton, Ontario

TITLE: Behaviour of Reduced-Scale Reinforced Concrete Masonry Shear Walls and Components

AUTHOR: Kevin J. Hughes, B. Eng. (McMaster University)

SUPERVISORS: Dr. Wael W. El-Dakhakhni

Dr. Robert G. Drysdale

NUMBER OF PAGES: xiv, 200

ABSTRACT

Reduced-scale models have become an attractive alternative to full-scale experimental laboratory testing due to both physical and financial restrictions. In order to have confidence in the ability of a reduced-scale model to replicate full-scale prototype behaviour, test data from reduced-scale research must be correlated and compared to test results of full-scale, prototype, materials. The overall goal of the following thesis is to provide a detailed comparison between third-scale models and full-scale prototype masonry materials, assemblages and wall components. The study includes a total of three phases of experimental testing. The first phase focuses on the individual elements that make up a reinforced concrete masonry shear wall. Elements examined include: third-scale model concrete blocks, mortar, grout and reinforcing steel. The second phase of the research project focuses on testing different configurations of masonry assemblages in an attempt to combine individual third-scale model elements into a composite assemblage to correlate behaviour to that of previously tested full-scale assemblages. The third and final phase of research compares two third-scale reinforced masonry shear walls to full-scale walls testing previously at McMaster University. In general, the third-scale model specimens showed good relation to full-scale prototypes for both the individual components and shear walls.

ACKNOWLEDGEMENTS

I would like to thank Dr. Wael El-Dakhakhni and Dr. Robert Drysdale for their continued support and encouragement throughout this research thesis.

The financial support from the Department of Civil Engineering at McMaster University, the National Sciences and Engineering Research Council of Canada, and the Canada Masonry Design Centre is sincerely appreciated.

This research could not have been completed without the support of the ADL laboratory technicians Dave Perrett and Kent Wheeler, it is very much appreciated.

Special thanks to Bennett Banting, Joe Wierzbicki, Marwan Shedid, and Jordan Vandervelde for all of your contributions to this experimental program.

The continued support of the Canadian Concrete Masonry Producers Association and David Stubbs from the Canada Masonry Design Centre are graciously acknowledged.

TABLE OF CONTENTS

LIST OF FIGURES

LIST OF TABLES

1 INTRODUCTION

1.1 Background

Masonry is one of the oldest and most popular forms of construction. It performs well under compressive loading but does not possess a high tensile capacity. While the use of masonry walls to resist gravity loads is typical, the use of reinforced masonry shear walls to resist lateral loading due to wind and seismic excitation can be just as effective. The current building code, NBCC 2005, penalizes the use of reinforced concrete masonry to resist seismic loads when compared to reinforced concrete shear walls. The NBCC uses a force modification factor, R_d, to reflect the ability of a structural system to exhibit inelastic response when subject to seismic excitation. The seismic, ductility-related, force reduction factor is lower for brittle structural systems and higher for more ductile systems. The NBCC also defines a material over-strength factor, R_o, which quantifies the individual reserve strength of Seismic Force Resisting System (SFRS) (Mitchell et. al, 2003). The material over-strength factor and the ductility related factors assigned to each SFRS reduce the design load on the system by a factor of their product. The NBCC assigns factors $R_d = 2.0$ and $R_o = 1.5$ for moderately ductile reinforced masonry shear walls while assigning factors $R_d = 3.5$ and $R_o = 1.6$ for ductile reinforced concrete shear walls. The result is that reinforced masonry shear walls must be designed to resist 1.87 times the load of a reinforced concrete shear wall in the same seismic region. This penalty is largely due the fact that historically, worldwide, unreinforced masonry structures have not performed well in seismic regions. Over the years, the use of concrete masonry as a structural building material, in seismic zones, compared to steel or reinforced concrete has decreased largely due to this perception. In an attempt to regain some of the lost ground over the years, recent research has shown, through repeated laboratory experiments, that concrete block masonry shear walls can be a

cost effective alternative to reinforced concrete shear walls when properly detailed.

1.2 Motivation for Research

Laboratory space restrictions and financial limitations are the typical reasons that reduced-scale modelling has been adopted as an alternative to full-scale testing. The challenge when performing experimental testing on reduced-scale models is to relate the results to a prototype or full-scale specimens so that the data becomes usable. This is where an investigation of all the individual components that make up the reinforced concrete masonry composite material is required. Recently, McMaster University has had success with the modeling of half-scale masonry shear walls (Long, 2006), (Banting et al., 2009), (Shedid, 2009) and it is the intent of this research program to provide the same level of confidence with respect to third-scale masonry.

1.3 Literature Review

The following sections highlight key concepts from past research completed with regards to reduced-scale modelling, reduced-scale masonry, masonry assemblage testing and the flexural behaviour of shear walls.

1.3.1 Reduced-scale Modeling

A structural model, as defined by Janney et al. (1970), is "*an assembly of individual structural elements built to a reduced scale that require laws of similitude in order to interpret test results*". Harris and Sabnis (1999) classify several different types of structural models; however this thesis focuses exclusively on two different model types: the *direct* model and the *strength* model.

In order for a structural model to be classified as a *direct* model it must be geometrically similar to the full-scale prototype. The loads applied during testing must be applied in a similar manner as they would be applied to the full-scale

prototype. As loading is applied during testing, all quantifiable measurements of a direct model including stresses, strains, and deformations should correlate well with the full-scale prototype (Harris and Sabnis, 1999).

A *strength* model, which has been adapted in the current study, is a *direct* model that is made up of reduced-scale individual material components that exhibit similar properties as their individual full-scale equivalents. The end result is a reduced-scale model that can accurately predict the behaviour of a prototype structure up to failure. A *true* reinforced concrete masonry strength model would require the individual constituent elements including the block, mortar, grout and steel reinforcing to exhibit similar material properties to their full-scale prototype equivalents. The more individual elements that a structural element possesses, the more complicated it becomes to produce an accurate *strength* model.

DIMENSIONAL ANALYSIS

The current study focuses on using third-scale masonry blocks to construct *strength* model representations of the full small masonry assemblages and shear wall specimens previously tested at McMaster University by Shedid (2006) and Long (2006). In order to produce an accurate structural model, the concept of dimensional analysis needed to be explored. Harris and Sabnis (1999) define a *true* model as one that "*satisfies every requirement of a complete dimensional analysis*". This includes scaling of the stress and strain (see Figure 1-1) of the prototype material in addition to the length, area, etc. Figure 1-1 provides a comparison of the variation in material stresses between prototype, σ_p, and *true* model, σ_m, at the same level of measured strain. At the same level of measured strain, ε, the stress exhibited by a *true* reduced-scale model will reflect its dimensional scaling factor and is lower than exhibited by the prototype.

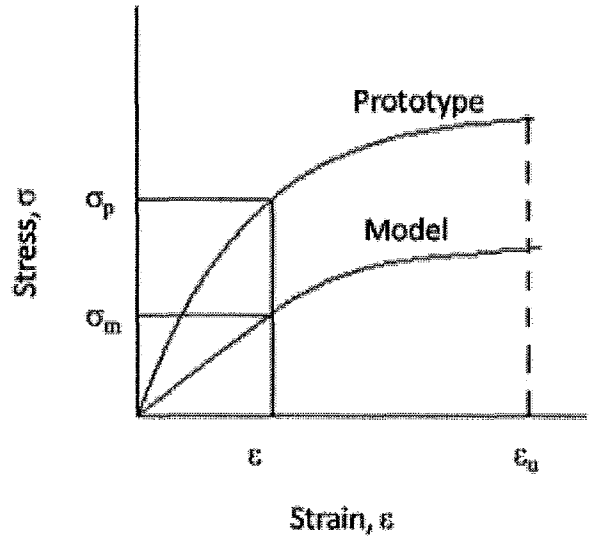

Figure 1-1: Stress-strain comparison of prototype and *true* model

However, Harris and Sabnis (1999) suggest that when modelling materials for which the stress due to self-weight of the material is not significant, a *practical true* model can be used. A *practical true* model assumes that the stress-strain relationship of the prototype material is identical to that of the model. This technique has been used successfully for various reduced-scale masonry research projects that will be discussed later in the chapter.

A practical true model uses a scale factor, S_L, to relate geometric and loading conditions between model and prototype materials. As mentioned earlier, the scale factor used throughout this research project is $S_L = 1/3$. Using this scale factor, the applied force on the third-scale model specimens was $S_L^2 = (1/3)^2 = 1/9$ that of the one on the prototype. The scale factor used for area was the same as that for force, once again indicating the fact that the scaled stress would be equal to prototype stress allowing for direct correlation to full-scale behaviour. A summary of the dimension analysis factors and a comparison between a true model and a practical true model are presented in Table 1-1.

Table 1-1: Summary of Scale Factors for Masonry Models (Harris and Sabnis, 1999)

Group	Quantity	Dimension	True Model	Practical True Model
Loading	Concentrated load, Q	F	$S_\sigma S_L^2$	S_L^2
	Moment, M	FL	$S_\sigma S_L^3$	S_L^3
Geometry	Linear dimension, l	L	S_L	S_L
	Displacement, δ	L	S_L	S_L
	Area	L^2	S_L^2	S_L^2
	Volume	L^3	S_L^3	S_L^3
Material Properties	Masonry unit stress, σ_m	FL^{-2}	S_σ	1
	Masonry unit strain, ε_m	1	1	1
	Elastic Modulus, E_m	FL^{-2}	S_σ	1
	Poisson's ratio, ν_m	1	1	1
	Stiffness, K	FL^{-1}	$S_\sigma S_L$	S_L

SIZE EFFECTS

An important aspect when dealing with structural models is the impact of the *size effects* on the model test results. The term, *size effect*, originates from a statistical theory based on the concept that the greater the size, the greater the probability of a localized point of weakness (Bazant & Chen, 1996). Prior to the 1980's little attention was paid to scaling and size effect and failure was quantified exclusively in terms of stresses and strains. In 1996, Weibull developed the theory of size effect that applied primarily to structures that failed in one isolated weak spot. Weibull's *size effect* theory did not directly apply to quasi-brittle such as concrete and masonry that do not experience failure in one isolated region. The failure mechanism of a quasi-brittle material is much more complicated. As a quasi-brittle fracture (cracking) typically initiates stress redistribution as it occurs. This stress redistributed typically continues up until failure (Bazant & Chen, 1996).

Currently there are three basic theories of scaling accepted in solid mechanics: the Weibull statistical theory (1996), the stress redistribution and

fracture energy release theory (Bazant, 1983) and finally the theory of crack fractality (Carpinteri, 1995). The scaling theory most applicable to quasi-brittle materials such as concrete and masonry is the fracture energy release theory (Bazant, 1983). Bazant's theory of *size effect* on quasi-brittle materials due to fracture energy release is based on the assumption that the crack lengths in both large and small structures are similar. Figure 1-2 describes an illustrative example included to further describe the theory behind Bazant's theory of *size effects* for quasi-brittle materials. As shown in Figure 1-2, when comparing structures experiencing similar cracking, a greater proportion of energy release occurs in the stress relief zone (defined by h) of a larger structure. The energy redistributed as a result of fracture is proportional to the hatched, fracture process zone, which is proportional to size of structure, D. The resulting energy release is proportional to $D^2\sigma_N^2/E$, where σ_N is the nominal stress applied to the material and E is Young's modulus. Conversely, if a structure is very small, the triangular stress relief zones will have negligible area compared to the crack band. Therefore, Bazant et al. (1996) suggests that *size effects* do not occur within extremely small structures.

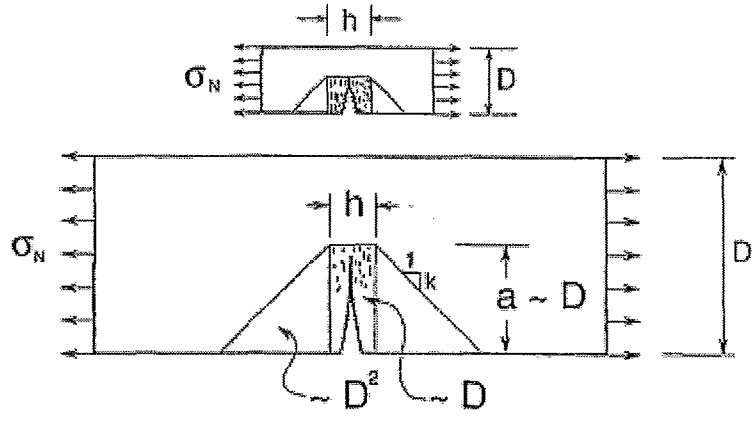

Figure 1-2: Approximate zones of stress relief caused by fracture in both small (model) and large (prototype) specimens ((Bazant & Chen, 1996)

The result is a softening effect on the post-peak load descending branch of the model load-deflection curve. Smaller structures typically experience a slow post-peak curve descent while larger structures have a steeper descent (see Figure 1-3). Larger structures characteristically exhibit a "snapback" at which energy is released suddenly during its steep decent, this "snapback" is less apparent in smaller structures (Bazant & Chen, 1996). Bazant et al. (1996) defines the ductility of a structure as the ratio between deflection at the point at which stability is lost, to elastic deflection. Figure 1-3 is a comparison of the nominal stress to relative deflection relationship of structures of varying sizes.

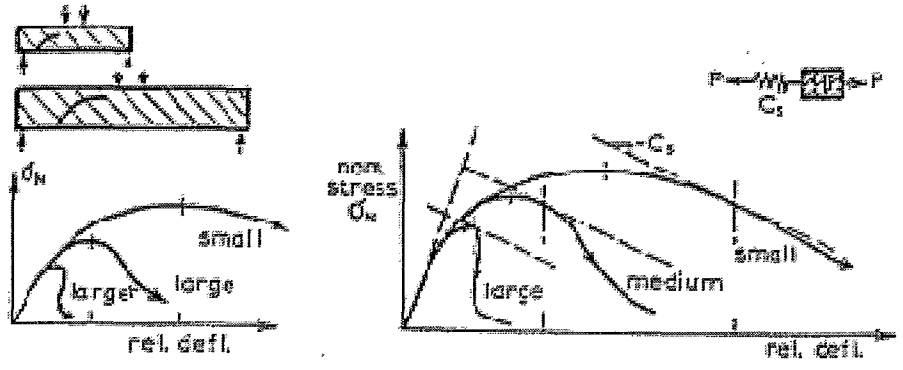

Figure 1-3: Load-deflection curve of quasi-brittle specimens of different sizes (Bazant & Chen, 1996)

Based on Bazant's definition of ductility and the prolonged post-peak descending branch of smaller structures load-deflection curves (Figure 1-3) it is clear that the smaller the structure, the more ductile the response.

1.3.2 Previous Reduced-scale Masonry Research

Reduced-scale model masonry research using quarter, third and half-scale concrete blocks has had great success since the early 1970's when Drexel began focusing on a reduced-scale masonry research program. Since then many

researchers have had success using reduced-scale masonry including: Hamid, Abboud and Harris (1985), Hamid and Abboud (1986), Abboud, Hamid and Harris (1990), Elshafie, Hamid, and Nasr (2002), Long, Hamid, and Drysdale (2005), Long (2006) and Huang, Chen, Shi and Gao (2009). Past testing of reduced-scale masonry has included both masonry assemblage (prism) testing and shear-wall specimens.

MODEL MASONRY ASSEMBLAGES TESTING

A research program involving the compression testing of forty nine quarter-scale concrete block prisms were completed by Hamid et al. (1985) in an attempt to correlate results to full-scale prototype prisms. It was assumed that the reduced-scale material properties were equal to the full-scale prototype. The main goals of the research project were to comment on the typical model prism failure mode, the stress-strain relationships of the model prisms compared to full-scale prototypes, the impact of mortar and grout strength and finally the geometry of the prisms. The research findings indicated that the failure modes of the model prisms were generally quite similar to those of full-scale prisms (Hamid et al., 1985). The failure mode of the model prisms changed from splitting to shear as the *h/t* ratio of the prisms approached 2.0 (due to the confinement of blocks in assemblages with lower aspect ratios). The mortar joints within the model prisms were found to have a greater impact of the compressive strength of the prisms compared to full-scale prototype prisms. The impact of mortar strength was attributed to the variability in size of mortar joints for model masonry (Hamid et al., 1985). The compressive strengths of the prisms were found to increase as the grout and mortar strengths increased. The impact of the mortar strength was much less for grouted prisms. Generally, the study completed by Hamid et al., confirmed the ability of quarter-scale model masonry to reasonably predict the behaviour of masonry prisms.

The possibility of using reduced-scale masonry to model the effect of shear and in-plane tension was explored by Hamid and Abboud (1986) through an experimental program that examined reduced-scale units and assemblages. The average shear strengths of the ungrouted model specimens were lower than the prototype strength as were the tensile splitting prisms. This strength reduction was attributed to the fast curing time associated with reduced-scale mortar joints (Hamid et al., 1986). The coefficients of variation associated with the quarter-scale test results were consistent with those from the full-scale prototypes, indicated the reliability of quarter-scale model masonry test results. In general, the results were favourable and similar to the quarter-scale compressive prism testing program confirmed the ability of reduced-scale masonry to model full-scale behaviour.

A half-scale model masonry research project at McMaster University by Long et al. (2005) examined the ability of half-scale masonry units to represent full-scale properties. Both full-scale and half-scale 190 mm block units and assemblages were tested as part of the research project. In general, both hollow and grouted masonry prisms showed excellent correlation between half and full-scale specimens. The strength and stress-strain relationships of half-scale grouted and ungrouted prisms showed very good similarity to full-scale specimens. The observed failure mode of the half-scale 4 course, running bond compressive prisms was diagonally cracking through the face shells and horizontal cracking through the blocks (Long et al., 2005). This failure mechanism was consistent with that noticed by Hamid et al. (1985).

MODEL SHEAR WALL TESTING

Thirteen third-scale reinforced concrete masonry shear walls were tested by Elshafie, et al. (2002) to examine the strength and stiffness of third-scale model masonry shear walls with openings. Elshafie et al. (2002) found excellent

correlation between post-peak stiffness models previous developed to relate the theoretical stiffness at yield to experimentally measured stiffness values.

In a half-scale masonry shear wall research program completed by Long (2006) a total of four half-scale model shear walls were compared to full-scale models tested by Shedid (2006). Two of the shear walls modelled by Long (2006) were designed to exhibit a flexural failure mode. In general Long (2006) found that the half-scale model shear walls exhibited similar load-displacement responses, failure modes and cracking patterns to the full-scale walls. It was found that due to the grout voids found in some wall specimens, the maximum aggregate size of grout should be limited to that of concrete sand. The strain-gradient effect and size effects were found to have a significant impact of the post-peak response of the shear wall specimens. The half-scale walls appeared to experience less damage at the same displacement levels of the full-scale prototypes. As a result, the ductility measured for half-scale was higher than the full-scale prototype walls (Long, 2006).

Similar to Long (2006) and Elshafie et al. (1992), Huang et al. (2009) have successfully used reduced-scale masonry to model the both grouted and grouted masonry assemblages tested under compressive loading and joint shear conditions. A quarter-scale "similar" model, or practical true model (Harris and Sabnis, 1999), was used to represent full-scale shear wall specimens. Huang et al. (2009) performed monotonic shear testing on quarter-scale model, two-storey concrete reinforced masonry shear walls and found that the shear capacity of the model walls were within 10% of the full-scale model prototypes. In general, Huang et al. (2009) suggested that practical true masonry models can effectively represent the behaviour of full-scale masonry shear walls. This suggestion was consistent with the findings of Long (2006) for the use of half-scale model masonry.

1.3.3 Concrete Masonry Shear Wall Research

In addition to resisting gravity loads, concrete masonry shear walls can be used to carry lateral loads due to wind and seismic excitation down to the foundation of a building. While historically unreinforced masonry shear walls have not performed well under seismic loading, the addition of both flexural (vertical) and shear (horizontal) reinforcing allows masonry shear walls, loaded in the in-plane direction, to deform into the inelastic range and ultimately exhibit a ductile failure mode.

Failure of unreinforced shear walls, loaded in the in-plane direction, can be characterized by four modes: rocking, sliding, diagonal tension and compression. Tension controlled rocking failure is a result of high lateral load and low axial compression. As cracking occurs at the bottom bed joint of the wall rocking failure occurs. Sliding failure occurs when the shear capacity of the masonry mortar joints is exceeded. Sliding failure typically occurs when walls are experiencing high lateral, but low axial loads. Diagonal tension cracking occurs as a result of high compressive axial loads and high applied lateral loads. Finally, compression failure occurs when the wall is loaded under high axial compression exceeding the strength of the masonry (Drysdale and Hamid, 2005).

Failure of reinforced shear walls can be divided into two groups: flexural and shear dominated failure. The flexural failure mode is a more ductile, and as a result more desirable, failure mode. Flexural failure is characterized by bed joint cracking, the yielding of vertical tensile reinforcement, and finally by compressive failure localized to the corners of the wall (Drysdale & Hamid, 2005). A test shear wall experiencing flexural failure has been provided in Figure 1-4. The post-peak stiffness and strength loss experienced by a flexural wall is steady and stable.

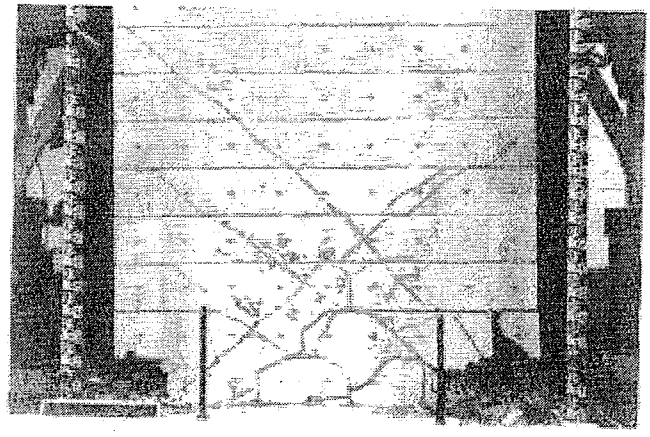

Figure 1-4: Shear Wall Experiencing Ductile Flexural Failure Mode (Shing, 1989)

The shear failure mode of reinforced masonry shear walls is characterized by diagonal tension failure (see Figure 1-5). Stiffness degradation occurs very quickly with a shear failure mode (Drysdale and Hamid, 2005). This quick strength and stiffness degradation is what characterizes the shear failure mode as a brittle when compared to the flexural mode.

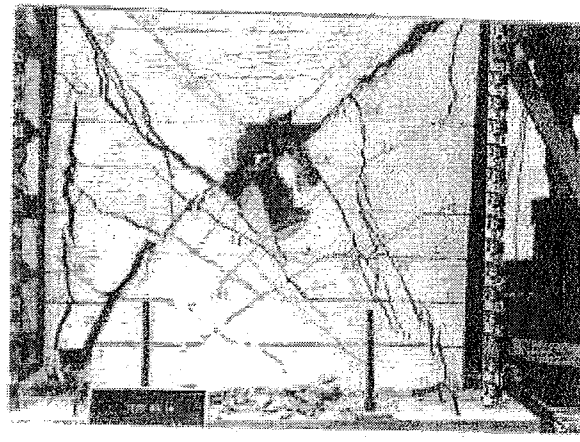

Shear Failure Mode
(Courtesy of P. Shing)

Figure 1-5: Shear Wall Experiencing Brittle Shear Failure Mode (Shing, 1989)

Masonry shear walls have been extensively researched and it has been shown that, when properly detailed, solid cantilever walls are capable of ductile behaviour. In order for a reinforced masonry shear wall to exhibit flexural behaviour it must be adequately reinforced to resist shear forces resulting from seismic excitation. If a shear wall is detailed such that the shear resistance of the wall is greater than the applied shear force, a brittle shear failure mode can be prevented, allowing the wall to exhibit inelastic deformations and ultimately fail in a ductile manner.

Past research by Priestly (1986), Shing, Noland, Kalmerus and Spaeh (1989), Lefas, Kotsovos and Ambraseys (1990), Ibrahim and Suter (1999), Voon and Ingham (2006), and Shedid (2006) have clearly demonstrated the ductility of a properly designed flexural reinforced concrete masonry shear wall.

Priestley (1986) explored the strength and ductility of reinforced masonry shear walls under seismic loading. Priestley (1986) presented the notion that ultimate strength theory be used in the design of masonry shear walls. Priestley

adopted the capacity design approach to masonry shear walls suggesting that by insuring the shear capacity of the wall exceeded the maximum applied lateral load, a wall could be allowed to exhibit flexural behaviour. The effectiveness of both vertical flexural reinforcing and horizontal shear reinforcing is increased when it is well distributed. Priestley also suggested that the shear resistance of a masonry wall within the plastic hinge region should be ignored and that the applied shear force must be resisted by only reinforcement in this region (Priestly, 1986).

Shing et al. (1989) confirmed the notion that shear walls that experienced a flexural failure mode were more ductile than those experience shear failure modes. The impact of axial load was found to increase the flexural strength capacity but decrease the ductility of a shear wall and as a result deemed and undesirable loading condition for a shear wall under seismic excitation (Shing et. al, 1989) (Lefas et al., 1990). Through a number of experimental tests of shear wall panels, Shing, et al. (1990) confirmed that the flexural strength and ductility can be reasonably predicted through the use of simple flexural beam theory.

A shear wall test program including five shear walls tested under fully reversed cyclic loading conditions by Ibrahim et al., (1999) continued to comment on the ductility of reinforced concrete shear walls. It was found that by decreasing the aspect ratio, through increasing the length of the wall, and increasing the applied lateral load, wall specimens seemed to experience primary diagonal tension cracking at the same lateral displacement values. It was also confirmed that the increase in vertical reinforcing increased the flexural capacity while an increase in horizontal (shear) reinforcement did not have much of an impact on the capacity of the walls (Ibrahim et al., 1999).

Voon and Ingham (2006) explored the impact of amount and distribution of shear reinforcing, level of axial compressive stress, type of grouting and finally aspect ratios on the ductile response of in-plane reinforced concrete masonry

shear walls. It was concluded that distributing the shear reinforcement evenly throughout the height of the wall increased the effectiveness of the shear reinforcing. The effect of axial compression stress was consistent with that found by Shing et al. (1989) and Lefas (1990). The decrease in ductility was attributed to the reduction in post-cracking deformation capacity (Voon et al. 2006). It was found that the shear strength of a shear wall is significantly reduced for partially grouted walls compared to fully grouted. Voon et al. (2006) showed that as the aspect ratio of shear walls decreased, the shear strength increased.

Research by Shedid (2006) and Shedid, et al. (2009) made several findings with respect to the ductility of reinforced concrete masonry shear walls. Shedid et al., (2009) found that the flexural strength of a shear wall is more heavily influenced by an increase in the amount of flexural reinforcement than an increase in compressive axial load. The displacement ductility, μ_Δ, (ratio of ultimate displacement to yield displacement, see appendix C) was highly dependent on the amount of flexural (vertical) reinforcing. The displacement ductility tended to decrease with an increased amount of flexural reinforcement (Shedid, 2006). It was shown that the plastic hinge (region of inelastic deformations) height, h_p, seemed to decrease with an increase in flexural reinforcement (Shedid, 2006).

1.4 Research Scope

The overall goal of the following thesis is to provide a detailed comparison between third-scale model and full-scale prototype masonry materials, assemblages and wall components. The study included a total of three phases of experimental testing.

The first phase focused on the individual elements that make up a reinforced concrete masonry shear wall. Elements examined included third-scale model concrete blocks, mortar, grout and reinforcing steel. The specific goal of this phase of research was to compare all third-scale elements to those used in past research studies completed by Shedid (2006) and Long (2006).

The second phase of the research project focused on testing different configurations of masonry assemblages in an attempt to combine individual third-scale model elements into a composite assemblage to relate behaviour to full-scale assemblages tested by Shedid (2006), Long (2006) and others. Assemblages were selected and tested to represent components of shear walls designed to exhibit flexural failure. A total of eighty assemblages were tested in this phase.

The third and final phase of research combined all elements of the previous two phases in the form of two third-scale reinforced masonry shear walls. The experimental results were meant to be direct models of full-scale walls tested previously by Shedid (2006) at McMaster University.

1.5 Thesis Outline

The following thesis has been organized into the following five chapters. Chapter 2 discusses the mechanical and physical properties of the individual third-scale model materials that were used throughout the research project and provides a direct comparison to full-scale prototype material properties. Chapter 3 describes a thorough masonry assemblage testing program that examines the major structural wall sections that are found in a reinforced shear wall experiencing flexural behaviour. Chapter 4 describes the details of the third-scale model shear wall testing program including wall characteristics and testing procedure. Chapter 5 discusses the experimental results of the two model shear wall specimens tested within this research program and provides a detailed comparison to the full-scale prototype walls tested by Shedid (2006). Finally Chapter 5 summarizes the findings of the research project and provides conclusions and recommendations for future research.

2 INVESTIGATION OF THE THIRD-SCALE MATERIAL PROPERTIES

2.1 Introduction

Reinforced concrete masonry is a composite construction material composed of concrete blocks, mortar, grout and steel reinforcement. In order to structurally model full-scale construction using reduced scale components, the individual reduced-scale materials must be examined and ultimately compared to their corresponding full-scale prototypes. The performance of the composite third-scale model will be compared to full-scale assemblage and shear wall specimens in later chapters. A detailed examination of the individual third-scale components that make up reinforced masonry shear walls is provided in this chapter along with a comparison to their respective full-scale materials. The materials that will be examined are the model concrete blocks, mortar, grout and steel reinforcement.

2.2 Third-Scale Model Concrete Block Production

The main component of a reinforced concrete masonry wall is obviously the concrete block. The blocks examined in this research are third-scale models of the standard 20 cm block available in Canada. The model block proportions were designed in accordance with the CSA A165.1 standard. The block production process will be discussed in this section along with the different trial mix proportions used during the block production phase of research.

2.2.1 Production of Model Block

Third-scale model blocks were produced using an industry standard Columbia block machine shown in Figure 2-1. The mould used to produce the blocks was designed to make eight blocks at a time. The mould layout is shown in Figure 2-2. The blocks were produced at a manufacturing plant where the

expertise of skilled block producing technicians was relied on heavily during the production process. Concrete blocks are manufactured from a zero-slump concrete mix of cement, aggregate and just enough water to allow for hydration (usually a water to cement ratio of around 40 %).

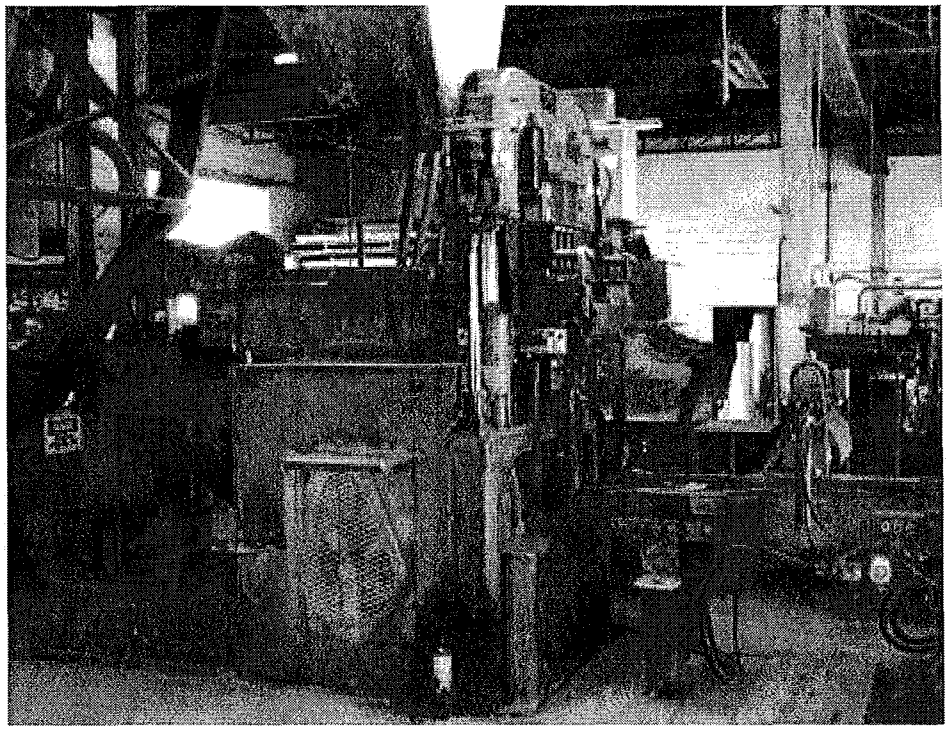

Figure 2-1: Columbia Block Machine

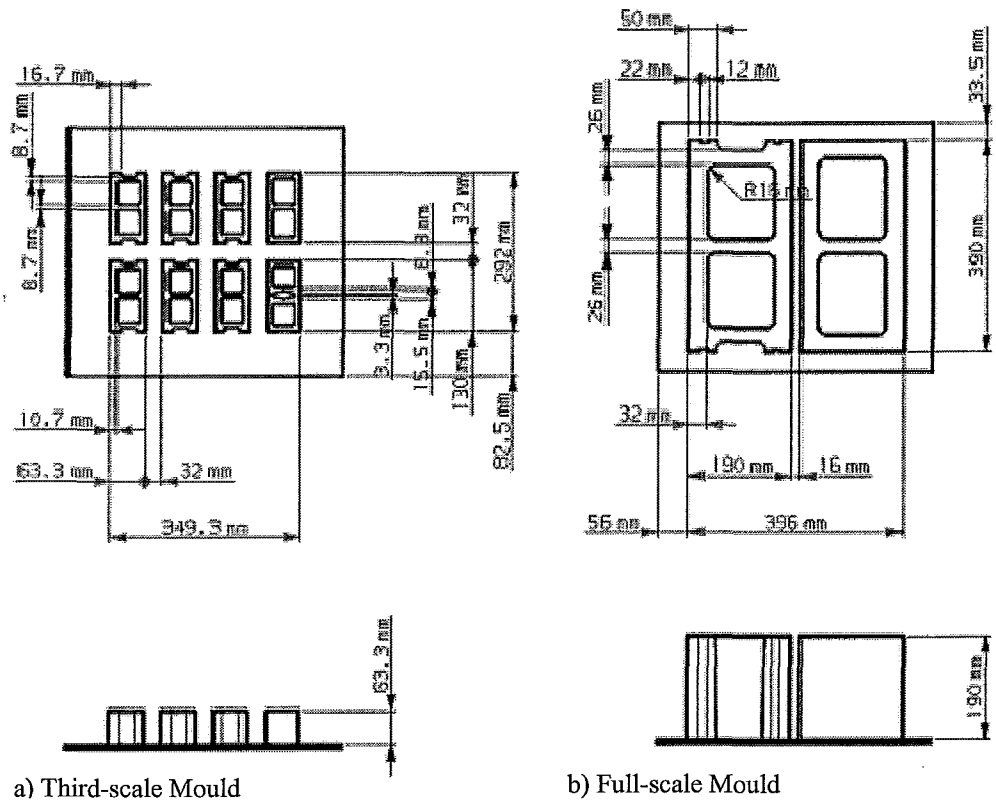

a) Third-scale Mould

b) Full-scale Mould

Figure 2-2: Mould Dimensions (Columbia Machine Inc., 2008)

The aggregates used for the concrete block mix during both phases of block manufacturing were stored outside and, as a result, were not dry at the time of mixing. Consequently there was no pre-determined amount of water added to each batch. The moisture content of the batch was monitored using an integrated computer system built into the mixer in order to ensure consistency between batches. In general, the water added to each batch was approximately 0.45 to 0.50 the cement content. The skilled block machine operator, who was in charge of the third-scale block production, relied on his extensive experience to verify the adequacy of the batch moisture content. As a rule of thumb, a clump of block mix should not expel any visible water when squeezed by hand; however the batch sample should produce a slight film when held (Grimo, 2008).

During the trial phase of block production, the individual batch materials (including water) were weighed and mixed in a small concrete mixer with an approximate capacity of 100 kg shown in Figure 2-3. Material was mixed for approximately five minutes. The trial batches were then transported to the block machine using a wheel barrow. The material was then dumped into the machine, 20 kg at a time. Specific details with respect to the mix proportions corresponding to each trial mix are discussed in Section 2.2.2.

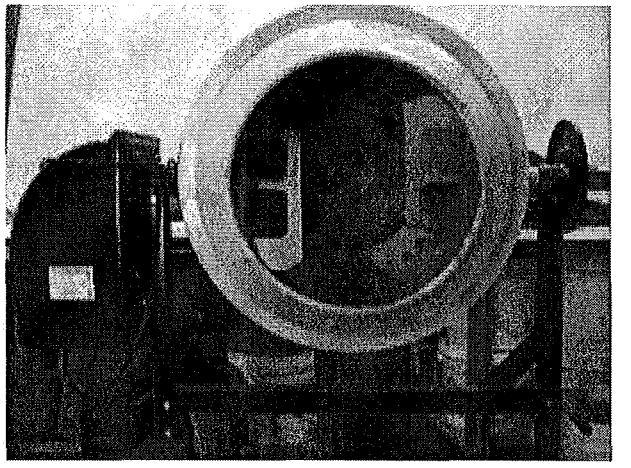

Figure 2-3: Small Concrete Mixer

The block material used for mass production was mixed using and industrial grade mortar mixer, similar to that shown in Figure 2-4, with an approximate capacity of 900 kg. The material was collected from the storage yard using a front-end loader and weighed by the block machine operator. As previously stated, the water was added automatically as the mixer monitored the moisture content within the batch. Just as with the trial batches, material was mixed for approximately five minutes. The large quantity of block material produced during each production batch was dumped from the mixer on to a conveyor belt and transported to a large hopper where the material was slowly fed into the material feed drawer of the block machine, (see Figure 2-5).

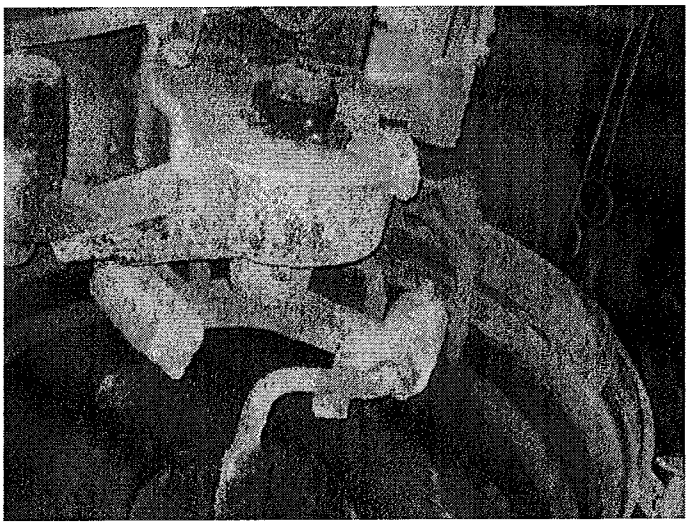

Figure 2-4: Mortar Mixer (similar to mixer used during block production)

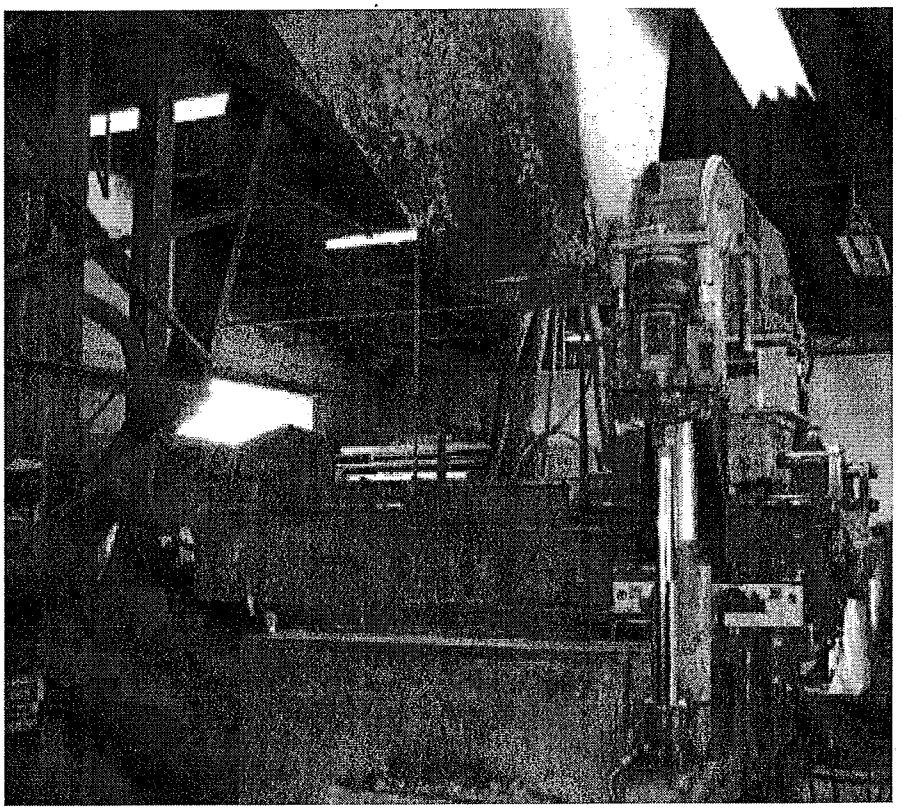

Figure 2-5: Columbia Block Machine Hopper (above feed drawer)

The loading of the material into the feed drawer of the block machine was the first step of the fully automated block production cycles. The material was then pushed forward over the top of the empty block mould where the machine head pressed and vibrated the very stiff material into the mould. As the material was positioned over the top of the mould, the palette table was raised to the underside of the mould to allow for filling. There were adjustable height pins on the machine head that stopped the vibration once the material in the mould reached its desired height. The blocks were then pushed down and out of the mould and onto a pallet by the block extruding machine head. The entire cycle took approximately eight seconds. Variables such as vibration rate, pressure palette table, and compaction pin height were all adjusted in order to produce a workable block. There were five common issues that required constant monitoring during block production; they are described in the following table (Columbia, 2009).

Table 2-1: Common Block Production Troubleshooting Issue (Columbia, 2009)

Issue	*Explanation*
Feather edge on bottom (Figure 2-6 a)	-Pallet table pressure too high
Loose, flaky bottom (Figure 2-6 b)	-Pallet table pressure too low - Mix too dry
Block sucking in (Figure 2-6 d)	-Mix too wet
Wall cracks (Figure 2-6 e)	-Take-away conveyor elevator improperly aligned with pallet table
Porous Block (Figure 2-6 c)	-Material segregated in the hopper -Improper block mix composition

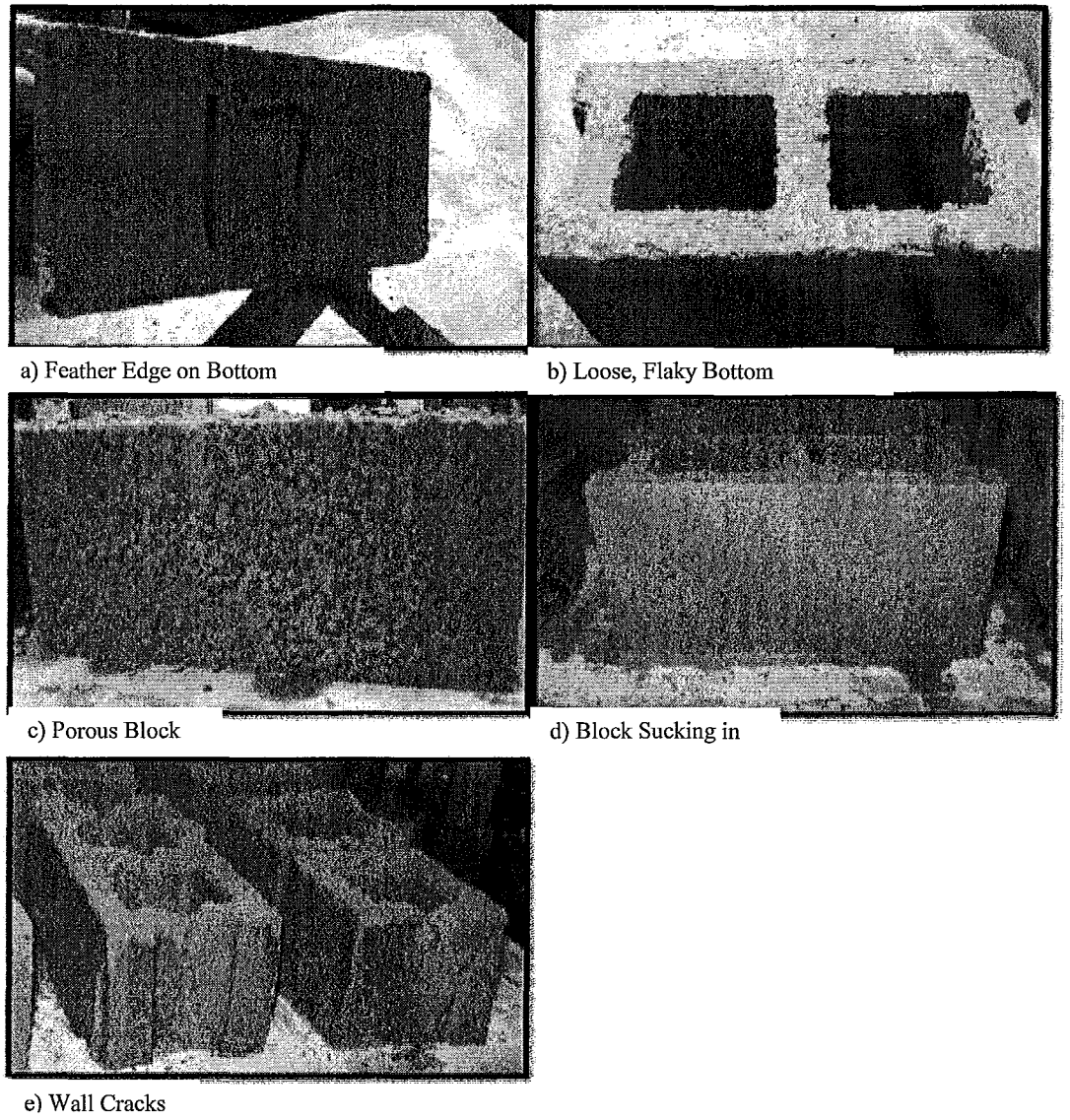

a) Feather Edge on Bottom

b) Loose, Flaky Bottom

c) Porous Block

d) Block Sucking in

e) Wall Cracks

Figure 2-6: Common Block Production Issues Encountered

As the blocks exited the production machine they were transported, using an automated conveyor, to a series of curing racks. Once the racks were full, they were moved by forklift to a steam-curing chamber. Each rack was capable of holding 288 blocks (see Figure 2-7). All of the blocks were steam-cured at atmospheric pressure for a 24 hour period. This type of low pressure curing is

designed to accelerate the curing process (Drysdale and Hamid, 2005). After the 24 hour steam-cure the blocks were stacked on to wooden pallets, wrapped in plastic and stored outside the facility until they reached 28-day strength. The curing process described was the same as that used for full-scale blocks produced at the same manufacturing plant.

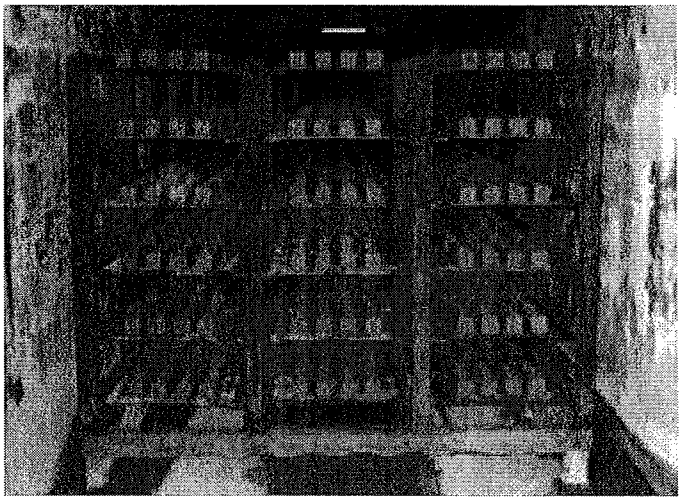

Figure 2-7: Block Curing Racks

2.2.2 Different Concrete Block Mix Designs

The purpose of the mix design phase was to find a reliable block mix that could be mass produced and eventually used to construct experimental specimens described in Chapter 2 and 3 of the thesis. There were a total of six mix designs selected for the preliminary stage of block production. The preliminary mix design was based on a benchmark mix established by Harris et al. (2005). This baseline mix proportions (by weight) were 1 part Type 10 Portland cement: 0.5 water: 5 sand. This mix was expected to yield block strengths in the range of 20 to 25 MPa. It was understood at this time that a typical full-scale concrete block mix would have approximately half of the cement to aggregate ratio; however it was assumed that the extremely small aggregates being used would require a

significantly larger amount of cement to properly cover the additional surface area.

A rigorous block strength sensitivity analysis, with respect to the mix proportions, was deemed unnecessary given the success of third-scale modelling completed at Drexel University (Harris et al., 1990). The main variable between the different mixes presented in this report was the size of the aggregate used. The intent was to compare the impact of varying aggregates on the compressive strength of the third-scale model blocks. The maximum aggregate size in all cases needed to be less than half of the minimum dimension in the mould; this would create a reasonably isotropic mix and allow for proper compaction. The smallest mould dimension is approximately 9.0 mm (see Figure 2-2) and is located in the middle web at the bottom of the block. It is for this reason that the largest aggregate used in any of the trial mixes passed through a 5.0 mm sieve; this is consistent with the full-scale aggregate limitations specified in ASTM C33-07 (ASTM, 2007). The other parameters that were varied during the preliminary mix design were the amount of cement used and the addition of a super-plasticizer.

After some preliminary experimentation, it was decided that the aggregate used for the block concrete mix would be a combination of masonry sand (fine aggregate) and an asphalt sand referred to as HL3 (coarse aggregate). It was thought that combining these two aggregates would allow for some variability in the gradation of aggregate used as opposed to simply using a single source concrete sand, that has been traditionally used in reduced-scale block production. The batch size of each mix was approximately 100 kg and mixed in a small concrete mixer. The first four mixes attempted had varying ratios of fine to coarse aggregate. The fifth mix had a lower cement to sand ratio and the sixth mix was identical to mix five with the addition of a super-plasticizer. Details and comments about the six different mixes are provided in Table 2-2.

Table 2-2: Trial Mix Details

Mix #	Mix Proportions (by weight) C : S : W	Aggregate Composition (%)	Compaction (material in to mould)	Finish (external)
#1	1 : 5 : 0.5	100% MS*	-No problems	-No problems
#2	1 : 5 : 0.5	50 MS, 50 HL3	-No problems	-Larger aggregate affecting the upper surface of the block during moulding
#3	1 : 5 : 0.5	100% HL3**	-height pins had difficulty making contact -material not compacting as previous mixes	-External texture noticeably coarser than previous mix
#4	1 : 5 : 0.5	67 MS, 33 HL3	-No problems	-No problems
#5	1 : 7.15 : 0.5	67 MS, 33 HL3	-No problems	-No problems
#6	1 :7.17 : 0.5 + additive	67 MS, 33 HL3	-No problems	-No problems

MS = masonry sand
****HL3 = asphalt aggregate***

As described in Table 2-2, during production there were a number of voids present in blocks from Mixes #2 and #3. The voids drastically affected the external finish of the top of the model blocks. The upper surface of the block after compaction was full of holes along both the webs and face shells of the blocks. This was attributed to the content of HL3 asphalt aggregate added to each of the mixes. This defect can be seen clearly in Figure 2-8 as the dark marks among the concrete debris on the top of the block. The problem was no longer visible during Mix 4.

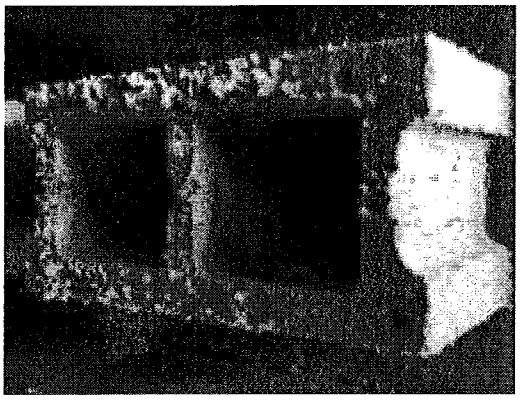

Figure 2-8: Block Voids Present in Mix #2 and #3

Mix #3 was the only mix that presented an issue with respect to compaction of the material. It was noticed that the material was taking longer to fill the mould as the height pins were slower to make contact. It was originally thought that simply too much material was being placed into the feed drawer at once, but after the quantity of material added was closely monitored the problem remained. The block surface produced in Mix #3 was noticeable coarser than those from other mixes (see Figure 2-9). These issues were attributed to the aggregate being composed entirely of HL3 asphalt sand.

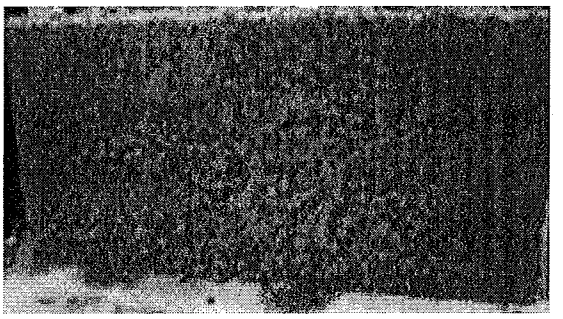

Figure 2-9: Texture of Mix #3 Block

In Mix #5, the cement to sand ratio was decreased to allow for a more typical full-scale ratio. The mix proportions are as follows: 1 cement: 0.6 water:

7.15 sand. The aggregate used in this mix was the same 67% masonry sand, 33% HL3 asphalt sand used in Mix #4.

The only difference between Mixes #5 and #6 was the addition of a super-plasticizer additive. The amount of additive used was approximately 50 g per 100 kg of cement. The purpose of adding a super-plasticizer was to allow for the material to better fill the mould and ultimately provide crisp edges on the block produced. The super-plasticizer increases the workability of the block mix without increasing the water content. A comparison of all the different blocks produced has been presented in Figure 2-10.

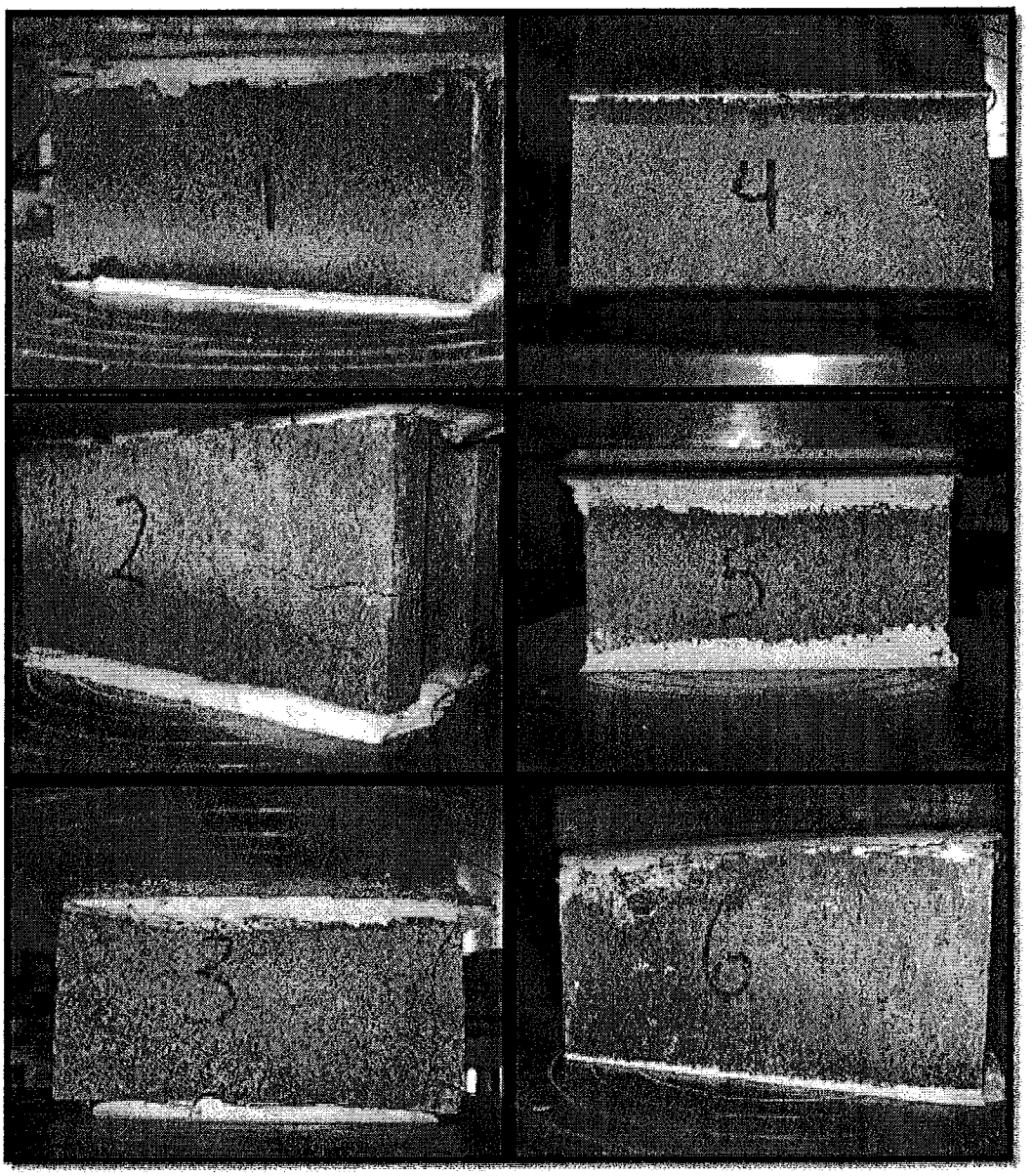

Figure 2-10: Summary of Different Blocks Produced

The gradation of the material used as aggregate in the trial concrete block mixes are shown in Figure 2-11. The purpose of this gradation curve is to compare aggregate used in trial block mixes with that developed at Drexel University by Abboud et al. (1990).

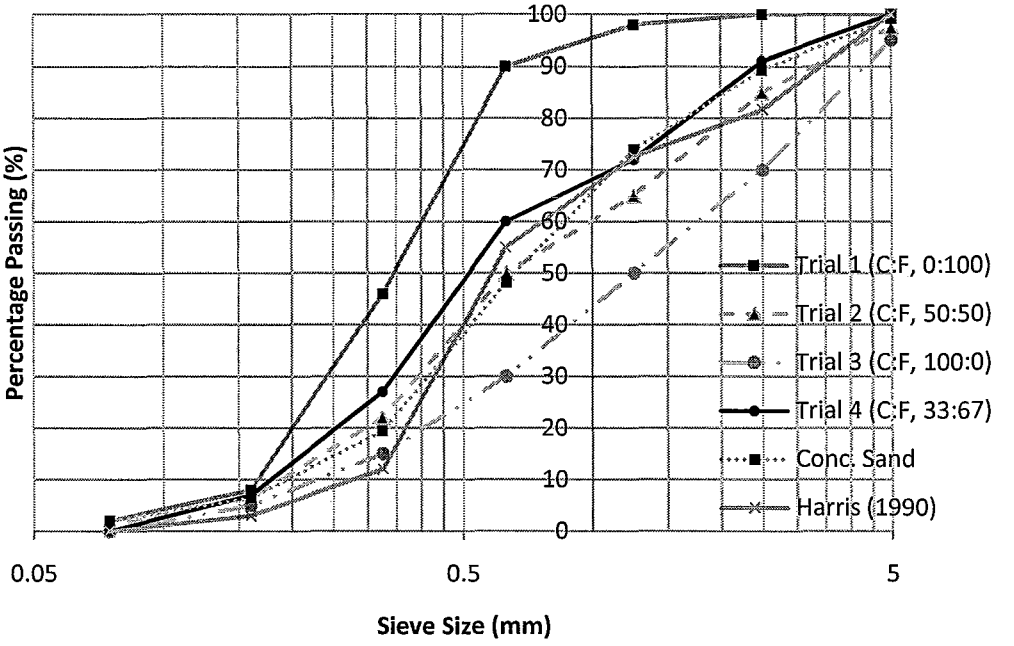

Figure 2-11: Trial Block Mix Aggregate Gradation

2.2.3 Impact of Aggregate Size on Material Strength

The impact of aggregate size on the compressive strength is reported in this section. The compressive strength after 1-day steam curing and after 28 days of air curing is summarized in Table 2-3 and Table 2-4 respectively. The significance of testing the trial blocks after 1-day steam curing becomes more apparent when the decision on the final mix to be used for mass production is discussed in detail.

As shown in the tables, the concrete blocks reach a relatively high strength (approximately 50% of 28-day) after the 1 day of steam curing. The thin face shells of the model blocks may have allowed curing to occur more rapidly than typical of prototype blocks. This shorter curing duration could explain the high model block strengths observed after 1-day. A similar phenomenon was observed

with the production of half-scale blocks tested at McMaster University by Long (2006).

Table 2-3: Compressive Strength of Trial Mix Blocks After 1 day of Steam Curing

Specimen	Trial 1	Trial 2	Trial 3	Trial 4	Trial 5	Trial 6
1	10.39	6.75	10.39	11.42	4.15	6.23
2	10.91	10.39	13.50	15.32	4.15	5.71
3	10.64	8.05	14.54	15.06	4.67	5.71
Average (MPa)	10.6	8.4	12.8	13.9	4.3	5.9
Coefficient of Variation C.O.V. (%)	2.5	22.0	16.9	15.6	7.0	5.1

Table 2-4: Compressive Strength of Trial Mix Blocks after 28 Days

Specimen	Trial 1	Trial 2	Trial 3	Trial 4	Trial 5	Trial 6
1	19.38	22.88	25.57	24.28	8.35	9.35
2	19.85	24.28	32.45	24.52	8.41	10.39
3	17.98	26.62	27.32	25.45	9.81	10.65
4	20.20	18.45	16.69	23.82	9.11	---
5	20.43	22.18	---	25.68	11.79	---
Average (MPa)	19.6	22.9	25.5	24.7	9.5	10.1
C.O.V. (%)	5.0	13.1	25.7	3.2	14.9	6.8

Looking at the data presented in Table 2-3 and Table 2-4, it is apparent that the average block strengths corresponding to individual trial mixes were somewhat variable after 1-day; however the average strengths after 28 days were much more consistent. It should be noted that the coefficient of variation (C.O.V.) for specimens from Mix #1 to #4 tested after 1 day averaged 21.4% and after 28 days averaged 11.4%. The strength gain versus time trend is shown in Figure 2-12. After 1 day, the trial block mix compressive strengths averaged 49% of their 28-day strength and after 14 days averaged 69% of the 28-day strength.

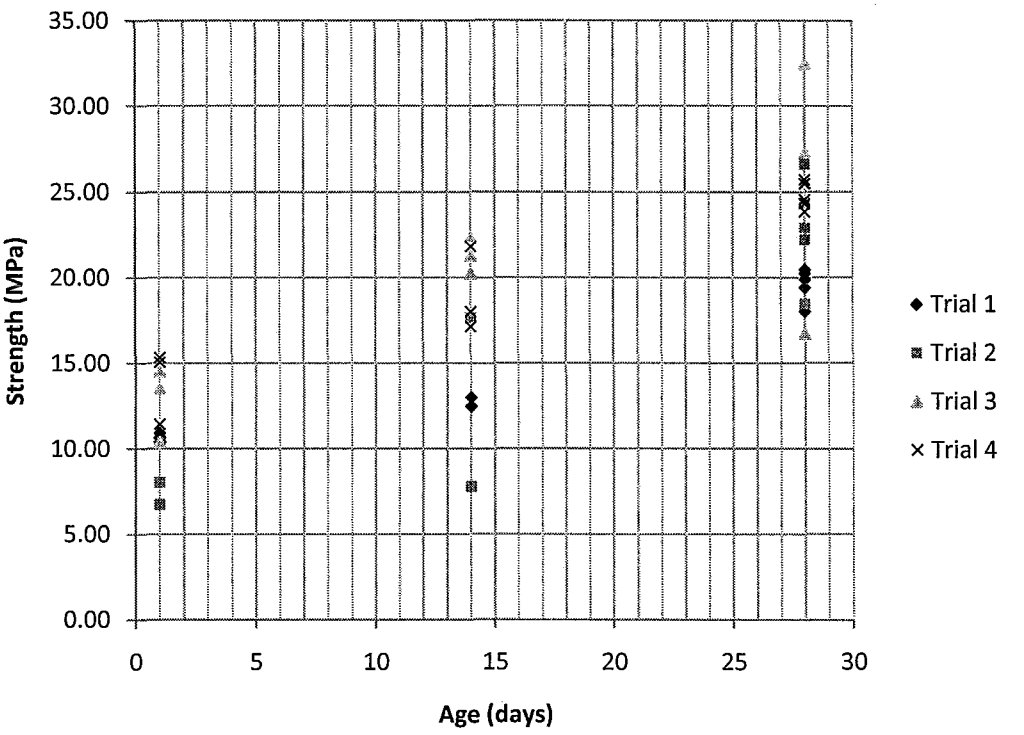

Figure 2-12: 28-Day strength gain of trial blocks

After examining the compressive strengths of blocks obtained from the mix design phase, of the following observations can be drawn. Certain aggregates produced a higher C.O.V. within the test data making the mix unreliable. This is apparent in Mixes #2 and #3 where the C.O.V. was as high as 25.7 % at the 28-day strength. Mix #1 produced a more consistent strength, but was a little below the 25 MPa desired strength. Mixes #5 and #6 produced strengths far below the 25 MPa mark and as a result it was concluded that the concrete mix proportions used for the first four mixes was adequate. The impact of the super-plasticizer additive was shown to be a slight increase in strength, approximately 5 % after 28-days. This increase in strength was attributed the quality improvement of the block with the use of the super-plasticizer.

2.2.4 Final Mix Design Selected for Block Production

The mix design selected for production was based on the compressive strength tests after 1-day of block steam curing. Due to the time constraints of having blocks produced at a manufacturing facility with only one available block machine, for a limited period of time, a decision on the final mix had to be made based on the 1-day strength evaluation. It was hypothesized that, based on a water to cement (w/c) ratio ranging between 0.4 to 0.5, after 1-day of steam curing the model blocks would be close to 40% of their 28-day strength (Johansen, 2006). Another important factor that was taken into consideration was the C.O.V. between the compressive strengths. It was desirable to have a mix that produced consistent compressive strengths. As mentioned earlier, it was assumed that an extensive mix design sensitivity analysis with respect to cement content was deemed unnecessary due to previous success with this mix proportion. In addition, the main focus of this experimental program was to validate the use of third-scale blocks to model masonry assemblages in order to use them to evaluate flexural behaviour of shear walls; an extensive block mix design optimization was outside the original scope of this work.

The 28-day compressive strength of the concrete blocks was expected to be approximately 25 MPa. Mix #4, with the proportions by weight 1 cement: 5 aggregate: 0.5 water was selected to be used for mass production. The physical and mechanical properties of the blocks used for the remainder of this experimental program will be discussed in detail in the following section. The final aggregate gradation of the model blocks was within the limits of ASTM C404 -07 (ASTM, 2007), size No. 1, as shown in Figure 2-13. It should be noted that the 28-day compressive strength of Mix 4 was 24.7 MPa with a C.O.V. of 3.2% (Table 2-4), only 1.2 % lower than the design strength.

During the production of the final block specimens it was noticed that the mix was not compacting sufficiently in the mould. It was decided that the

addition of a 5 mm steel lip around the top of the mould would allow for more material to enter the mould and result in better compaction. The mould used in this study had never been previously used to produce third-scale blocks, so some minor adjustments were required to produce a workable block. This addition can be seen in Figure 2-14.

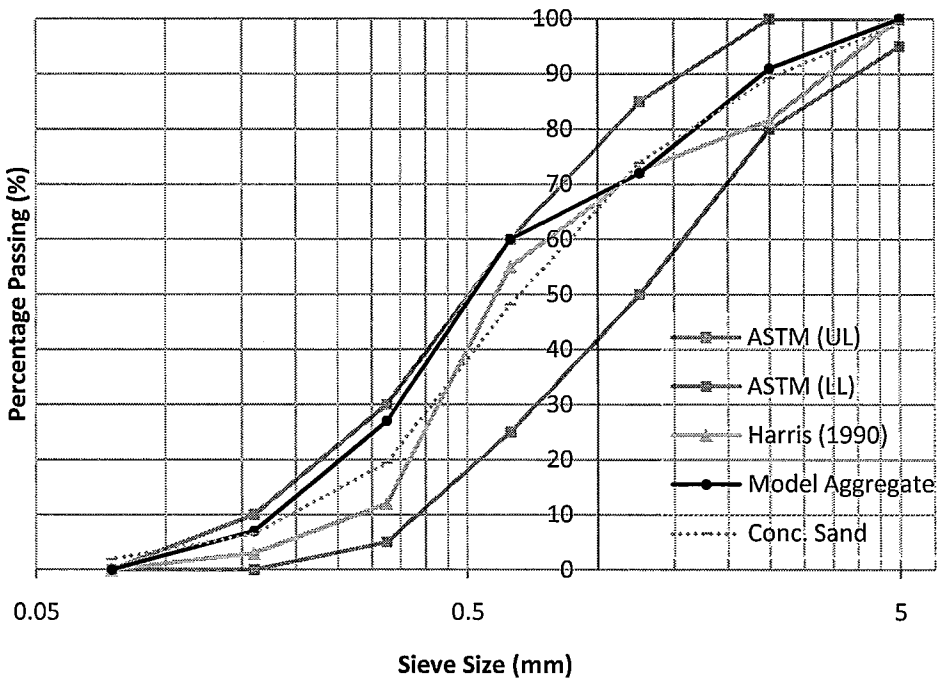

Figure 2-13: Model Block Aggregate Gradation

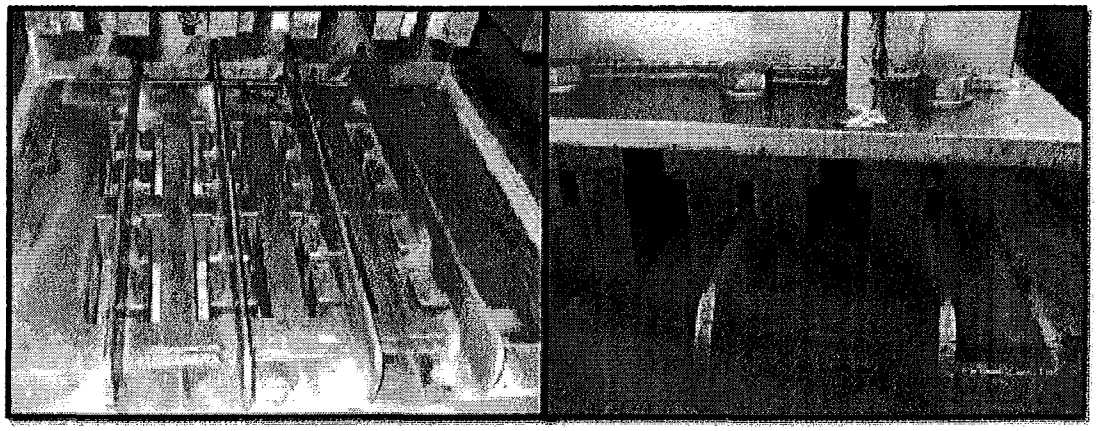

a) Mould Before "lip" Addition

b) Mould After "lip" Addition

Figure 2-14: Third-scale Block Mould Alteration

2.3 Material Properties of the Model Blocks

Specific details with respect to both the physical and mechanical properties of the final model blocks produced are discussed in the following section. Compressive strength, density, volume, absorption, tensile splitting and compressive strength of blocks loaded parallel to the bed face are examined. For the purposes of scaling, each material property has been compared to an equivalent full-scale test performed by others. Full-scale testing comparisons were completed by Khalaf (1989), Long (2005), and Shedid (2006).

2.3.1 Geometric Properties of Model Block

As mentioned previously, the reduced-scale blocks used in this research were third-scale models of a standard 20 cm concrete block with a 32 mm face shell thickness. Three types of blocks were produced to be used during specimen construction: stretcher units with frogged-ends, end units and half end units (see Figure 2-15 and Figure 2-16 for model block dimensions). To facilitate demoulding, the blocks had tapered flanges and webs comparable to those of the full-scale prototype blocks.

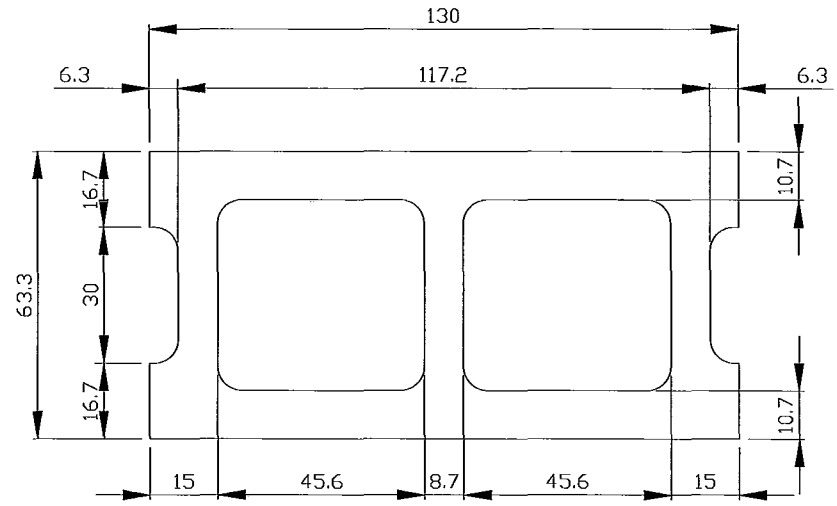

a) Top View of Model Stretcher Unit

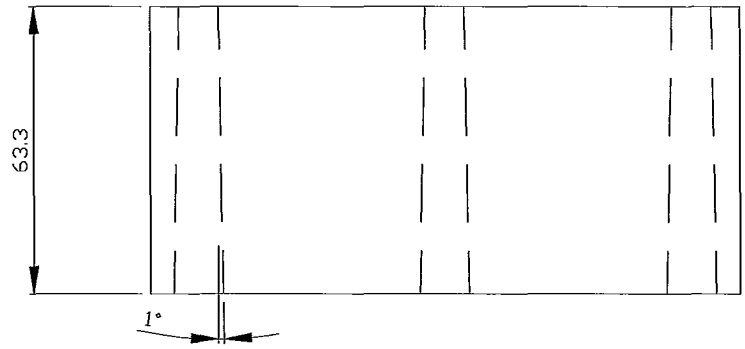

b) Side View of Model Stretcher Unit

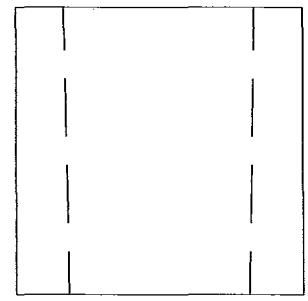

c) End View of Stretcher

Figure 2-15: Model Stretcher Dimensions

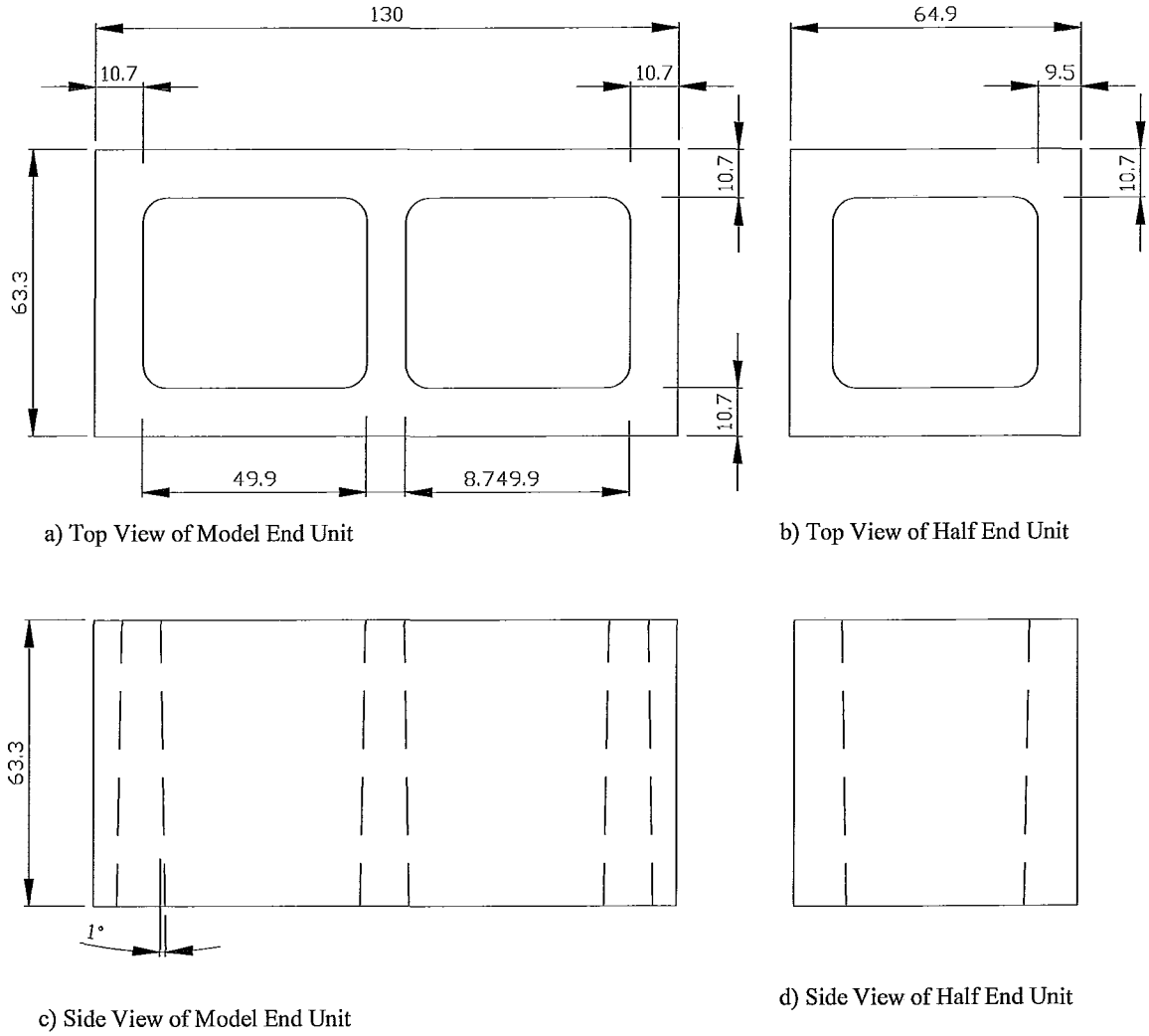

a) Top View of Model End Unit

b) Top View of Half End Unit

c) Side View of Model End Unit

d) Side View of Half End Unit

Figure 2-16: Model End-unit Dimensions

2.3.2 Density, Volume, and Absorption

Density, volume and absorption characteristics of the model blocks were determined following the ASTM C140-08 (ASTM, 2008) standard in order to compare these non-structural properties of the blocks with the full-scale prototypes. The results from the standard tests are shown in Table 2-5. The table shows results from all three types of blocks produced: regular stretcher blocks (*R*),

end unit blocks (*E*), and half end units (*H*). The height of each unit was taken as the average of four measurements made with a digital micrometer.

Table 2-5: Summary of Density, Volume and Absorption Testing of Third-Scale Blocks

Specimen	Height (mm)	Absorption (kg/m^3)	Absorption (%)	Density (kg/m^3)	Net Volume (mm^3)	Net Area (mm^2)
R-1	63.8	115.9	5.25	2210	276,000	4326
R-2	62.8	123.2	5.63	2188	273,999	4395
R-3	64.3	131.9	5.95	2232	273,000	4268
Average	63.86	123.7	5.61	2210	274,333	4330
C.O.V. (%)	1.2%	6.5%	6.24%	1.0%	0.56%	1.46%
E-1	63.6	154.1	7.26	2124	266,000	4186
E-2	63.3	172.9	8.46	2045	266,000	4202
E-3	62.8	185.3	9.06	2046	259,000	4127
Average	63.2	170.8	8.26	2072	263,666	4172
C.O.V. (%)	0.65%	9.19%	11.10%	2.18%	1.53%	0.95%
H-1	63.9	131.6	6.01	2190	152,000	2378
H-2	64.3	137.3	6.31	2176	153,000	2381
H-3	64.4	137.3	6.25	2196	153,000	2377
Average	64.2	135.4	6.190	2188	152,666	2379
C.O.V. (%)	0.35%	2.42%	2.56%	0.46%	0.38%	0.09%

The third-scale results presented in Table 2-5 represent the material characteristics of the third-scale blocks produced with the final mix proportion that will be used for the remainder of this experimental program. The block densities and absorption properties all well within the guidelines in ASTM C140-08. Table 2-6 and Table 2-7 compare the full-scale 20 cm concrete blocks tested as part of Long's (2006) experimental program to those previously listed in Table 2-5. The difference between the full-scale and third-scale density is negligible. However, the third-scale models had absorption values that were 13.0% below their full-scale prototype. This physical characteristic of the model block became more apparent during the construction of model shear wall specimens described later in this research program. It was noticed during the shear wall construction

that the walls did not "bleed" water the same way that full-scale or half-scale walls did during grouting of the walls. It was this observation that made it clear that the model blocks were less absorptive than the prototype blocks.

Table 2-6: Full-Scale Density Comparison (full-scale data from Long, 2006)

Specimen	Density (kg/m^3)		Comparison
	Third-Scale	Full-Scale (Long, 2006)	(% difference)
1	2210	2171	---
2	2188	2167	---
3	2232	2166	---
Average	**2210**	**2166**	**2.0%**
C.O.V. (%)	**1.0%**	**0.2 %**	

Table 2-7: Full-Scale Absorption Comparison (full-scale data from Long, 2006)

Specimen	Absorption (kg/m^3)		Comparison
	Third-Scale	Full-Scale (Long, 2006)	(% difference)
1	115.9	140.1	---
2	123.2	141.3	---
3	131.9	138.2	---
Average	**123.7**	**139.8**	**13.0%**
C.O.V. (%)	**6.5%**	**1.1%**	

2.3.3 Compressive Strength

The compressive strength testing of the model blocks was carried out in accordance with ASTM standard C140-08 (ASTM, 2008). Each specimen was hard capped with hydro-stone (gypsum) and loaded with a steel bearing plate on top and bottom of the specimens. Typical failure mechanism of the block was characterized by asymmetric shear-compression failures within the face shells, shown in Figure 2-17. This failure mechanism corresponds well to typical full-

scale block and that of previous third-scale block compression testing completed by Assis et al. (1989).

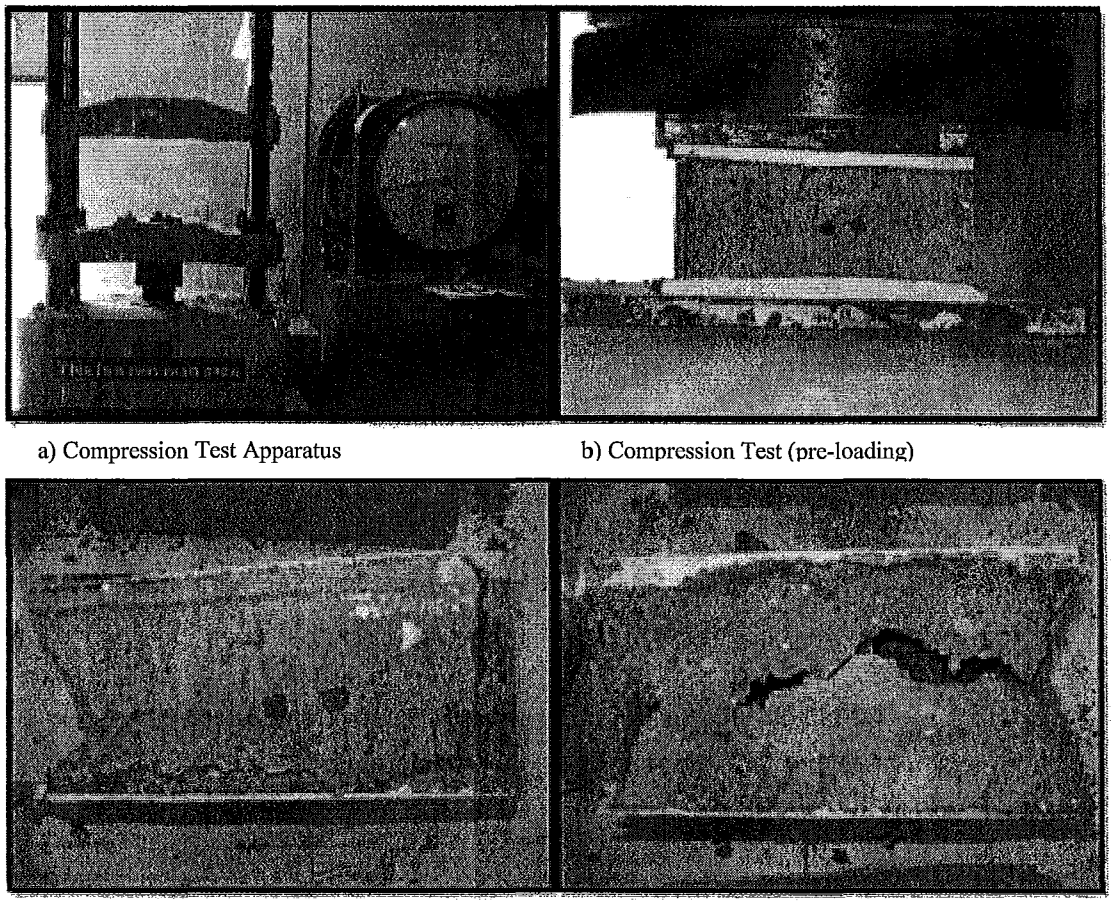

a) Compression Test Apparatus

b) Compression Test (pre-loading)

c) Typical Failure Mechanism

d) Typical Failure Mechanism (loaded beyond failure)

Figure 2-17: Typical Compression Failure Mechanism

The results of the compressive testing are shown in Table 2-8.

Table 2-8: Compressive Strength of Model Blocks

Specimen	Compressive Strength (MPa)
C-1	56.5
C-2	53.4
C-3	57.6
C-4	55.2
C-5	51.1
Average	**54.8**
C.O.V. (%)	**4.72**

Compressive strength based on average net area of 4,330 mm^2

Table 2-9 provides a comparison to the full-scale prototype blocks tested by Long (2006) and Shedid (2006). Although the density and absorption properties of the model blocks remain consistent with those of the prototype, the compressive strengths of the model blocks used for the remainder of this experimental program are much higher than the prototype blocks.

Table 2-9: Full-Scale Compressive Strength Comparison

Specimen	Compressive Strength (MPa)		
	Third-Scale$^{\times}$	Full-Scale* (Long, 2006)	Full-Scale$^{¥}$ (Shedid, 2006)
1	55.9	26.7	25.32
2	52.9	21.3	23.69
3	57.0	25.1	25.41
4	54.6	---	---
5	50.6	---	---
Average	**54.2**	**24.4**	**24.81**
C.O.V. (%)	**4.72%**	**11.4%**	**3.89%**

$^{\times}$ *Based on average net area = 4,330 mm^2*
**Based on average net area = 40,335 mm^2*
$^{¥}$*Based on average net area = 42,500 mm^2*

It is obvious from the results in Table 2-8 and Table 2-9 that the compressive strengths of the model (54.2 MPa) are much higher than their intended design strength of 25 to 30 MPa. Unfortunately, there were two main

inconsistencies between the original and final block production processes that ended up drastically increasing the block compressive strength.

The first difference was the quantity of material mixed in each batch. The exact quantities, as mentioned earlier increased from approximately 100 kg during the trial mix batches to 900 kg during final production. The impact of this difference on the strength of the model blocks is attributed to the larger mortar mixer used to mix the batches of larger quantity. It was concluded that the drum mixer most likely did not provided adequate cement coating of the aggregate. This phenomenon would cause inconsistency within the block mix and allow for "weak" spots to be present within the actual blocks and ultimately result in a significant reduction in the compressive strength of the units. The larger, mortar mixer used for final production would have allowed for a much more consistent mixing of the cement and concrete aggregate, allowing the block material to reach its full strength potential. A similar trend was found during a third-scale block mix design sensitivity analysis performed in August, 2009 at McMaster University (Banting, Heerema, and El-Dakhakhni, 2010). A comparison of model blocks tested by Banting et al. (2010) where the block material was mixed using a small (50 kg) drum mixer and a large (200 kg) concrete mixer is shown in Figure 2-18. Banting noticed a 52.1% 28-day strength increase for air-cured blocks and a 54.1% increase for the water-cured blocks. These results clearly reinforce the fact that a small drum mixer does not provide adequate mixing of the aggregate, cement and water and, as a result the mix does not reach its compressive strength potential.

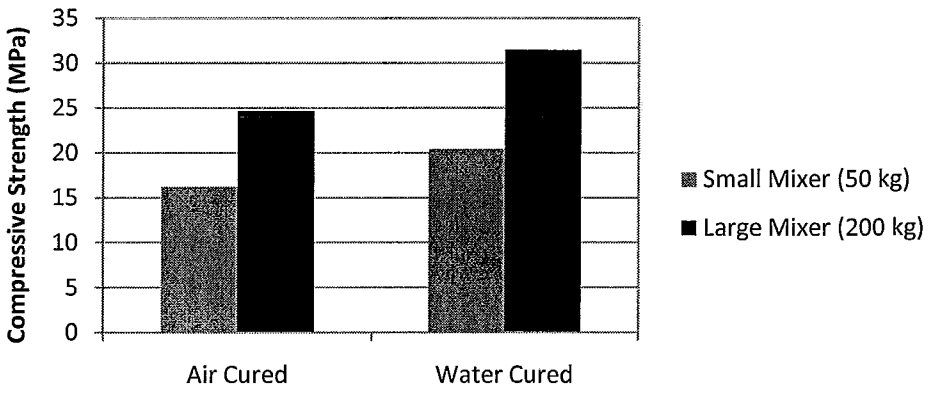

Figure 2-18: Impact of Mixer Type on Compressive Strength

The second major difference between the blocks produced using the original mixes and those of the final production mix was the addition of the previously mentioned steel lip around the top of the block mould. The presence of that addition allowed more material into the mould and provided a denser block and ultimately increased the compressive strength of the model units. The impact of the steel lip additions on the block density and absorption properties are shown in Table 2-10.

Table 2-10: Impact of Mould Addition on Density and Absorption

Specimen	Density (kg/m^3)		Absorption (kg/m^3)	
	without "lip"	with "lip"	without "lip"	with "lip"
1	2149	2210	141.8	115.9
2	2053	2188	167.9	123.2
3	2156	2232	144.4	131.9
Average	**2119**	**2210**	**151.1**	**123.7**
C.O.V. (%)	**2.7%**	**1.0%**	**9.5%**	**6.5%**

As shown in Table 2-10, the addition of the steel lip on the model block mould increased the density of the blocks by an average of 4.3% while the absorption of the model blocks decreased by 19.5%. The compressive strength of blocks tested after 28 days increased from 39.6 MPa for the blocks prior to the

addition of the steel lip to 54.2 MPa after. The data presented in Table 2-10 all pertain to blocks produced using the large (900kg) mortar mixer.

Moreover the drastic strength difference between the model blocks and the prototype can be attributed in part to high cement to aggregate ratio and to the increased density resulting from the block mould alteration. When mass producing large quantities of reduced-scale blocks it is imperative that a comprehensive study including both aggregate selection and cement content be carried out, with attention paid to the quality of the mixing process and batch size, in order to obtain model blocks of a desired strength. The impact of the high block strength on the f'_m of the masonry assemblages will be discussed later in Chapter 3.

2.3.4 Tensile Splitting

Tensile splitting tests were performed to ASTM C1006-07 (ASTM, 2007) standard. The results from this test are summarized in Table 2-11. All specimens tested had a similar failure mechanism, illustrated in the Figure 2-19. The tensile splitting failure is denoted by a distinct vertical crack along the line of loading. There were no visible voids or any other imperfection noted in the specimens during the time of the test. The results of the tension splitting tests have been compared to those of full-scale units tested by Long (2006) and summarized in Table 2-11.

Table 2-11: Full-Scale Tensile Splitting Comparison

Specimen	Tensile Splitting, f_t (MPa)		Comparison
	Third-Scale	Full-Scale (Long, 2006)	(% difference)
1	2.01	2.48	---
2	1.86	2.55	---
3	2.48	--	---
4	2.57	--	---
Average	**2.2**	**2.48**	**12.7%**
C.O.V. (%)	**15.5**		**---**

a) Tensile Splitting Specimen b) Typical Failure Mechanism

Figure 2-19: Typical Tensile Splitting Failure Mechanism

2.3.5 Compressive Strength Parallel to Bed Face

The results of the compressive strength parallel to the bed face of the model masonry units are shown in Table 2-12. The purpose of this test is to simulate the compressive force applied parallel to the bed face of blocks in the compression zone of reinforced masonry beams (Khalaf, 1989). The individual blocks were loaded parallel to their bed joints, see Figure 2-20 below. Compressive strength values found in the following table are based on an area net area of 2,160 mm^2. This area represents the two face shells that are carrying the compressive load in this case.

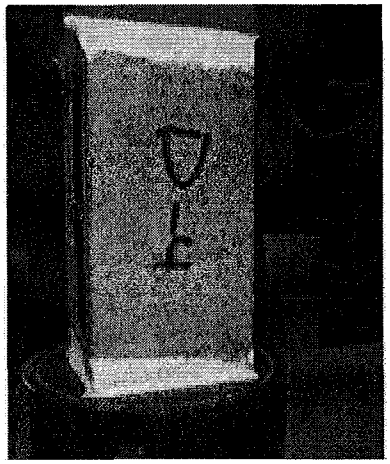

a) In-plane Compressive Test Setup

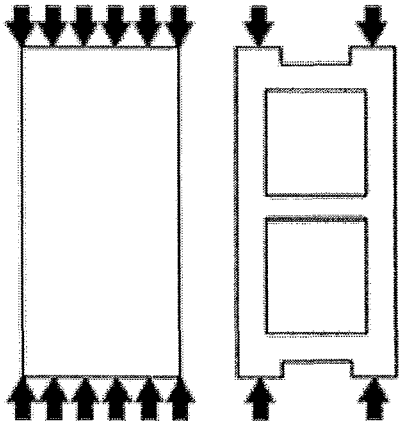

b) Block Loaded on Face Shells

Figure 2-20: Setup of In-Plane Compressive Strength Tests

These results summarized and compared to full-scale unit testing completed by Khalaf (1989) in Table 2-12.

Table 2-12: In-Plane Compressive Strength of Blocks (full-scale data from Khalaf (1989))

Specimen	Compressive Strength of Blocks Loaded Parallel to Bed Joint			
	Third-Scale (MPa)	Percentage of f'_{b1} (%)	Full-Scale (MPa)	Percentage of f'_{b2} (%)
1	39.9	73.6	19.4	63.8
2	40.5	74.8	23.1	76.0
3	33.9	62.6	19.0	62.5
4	40.2	74.2	23.6	77.6
5	42.8	78.9	23.3	76.6
Average	**39.5**	**72.8%**	**21.7**	**71.3%**
C.O.V. (%)	**8.35%**	---	**10.5%**	---

Compressive strength of model block normal to the bed joint, f'_{b1} = 54.2 MPa
Compressive strength of full-scale block normal to bed joint, f'_{b2} = 30.4 MPa (Khalaf, 1989)

The results from the compressive strengths of the blocks tested parallel to the bed joint were similar to those testing in the traditional fashion (normal to the bed joint) in that the strengths were very high. However, data presented by

Khalaf (1989) suggests that the compressive strength of a 20 cm block parallel to the bed joint is typically 71.3% of the compressive strength normal to the bed joint. When comparing the ratios of compressive strengths normal and parallel to the bed joints of the third-scale model blocks a ratio of 72.8% was found. This is almost identical to the trend presented in Khalaf's (1989) data.

The failure mode of the blocks tested in this manner was characterized be some local crushing near the legs of the block followed by complete destruction of the block as one face shell usually failed first (see Figure 2-21).

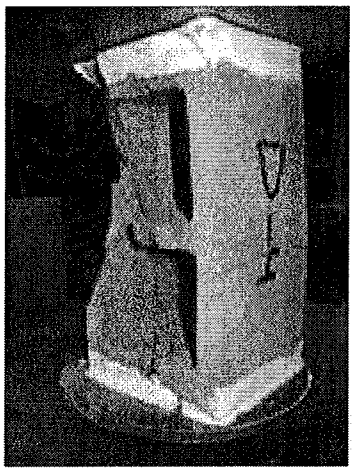

Figure 2-21: Typical Failure Mechanism for In-Plane Compression

2.3.6 Comments about the Model Blocks

In general, the blocks that were ultimately mass-produced and used for the remainder of this experimental program, in both assemblage and final wall specimens, were much stronger than the prototype strength. The impact of variations between preliminary and final production was not fully known until after the final blocks were produced. Time was a factor in the production of the model blocks, as the plant where the blocks were manufactured had to shut down for a week to accommodate the third-scale mould installation and block production. The high block strength was attributed to the high cement content

present in the mix; however the other material properties (density, absorption) of the block remained fairly consistent with those of the full-scale prototype. In fact, had the amount of cement used been reduced, it is believed the blocks would have correctly mimicked both the material and the physical properties of the prototype block.

2.4 Model Mortar

The impact of aggregate size and cement type on the compressive strength of mortar will be discussed in the following section. The maximum aggregate diameter used for mortar was obviously required to be smaller than the 3.3 mm bed joints used in both the masonry shear walls and assemblages that will be described later in the thesis. The aggregate selected (shown in Figure 2-22) was bagged masonry sand that had been sieved to ensure that all aggregate passed through the 1.25 mm diameter sieve. The strength of the mortar used for each type of assemblage and finally for the shear wall specimens will be described in Chapters 3 and 4, dedicated to their respective phases in the research program.

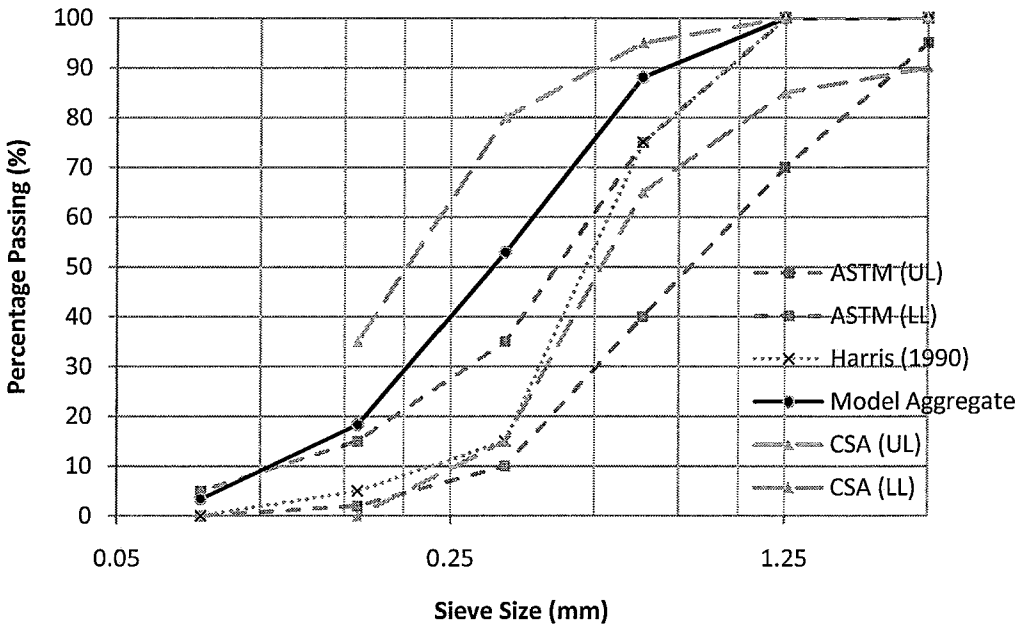

Figure 2-22: Gradation Curve of Aggregate Used in Model Mortar

Four different Type S Portland cement-lime mortars were produced and tested to compare the impact of sieving out aggregate larger than 1.25 mm as well as using either Type 10 or Type 30 cement on the compressive strength of mortar. Type 30 (high-early strength Portland) cement had been used previously in Drexel University in studies using both third-scale and quarter-scale blocks (Hamid et al., 1990). Type 30 cement was compared to Type 10 (normal Portland) cement in order to document the impact of the two cement types on the sieved aggregate and ultimately on the compressive strength of the mortar. Six 51.4 mm mortar cubes were tested, as per ASTM C109-08 (ASTM, 2008) standard, for each mix at 7 days, and at 28 days in order to compare compressive strengths of the different mixes. The mortar mixes quantities, by weight, were 1:0.2:3.53 (cement: lime: sand). The average flows recorded for each of the 4 mixes was very consistent, varying from 126% to 133%. The results from the compressive strength tests are shown in Figure 2-23.

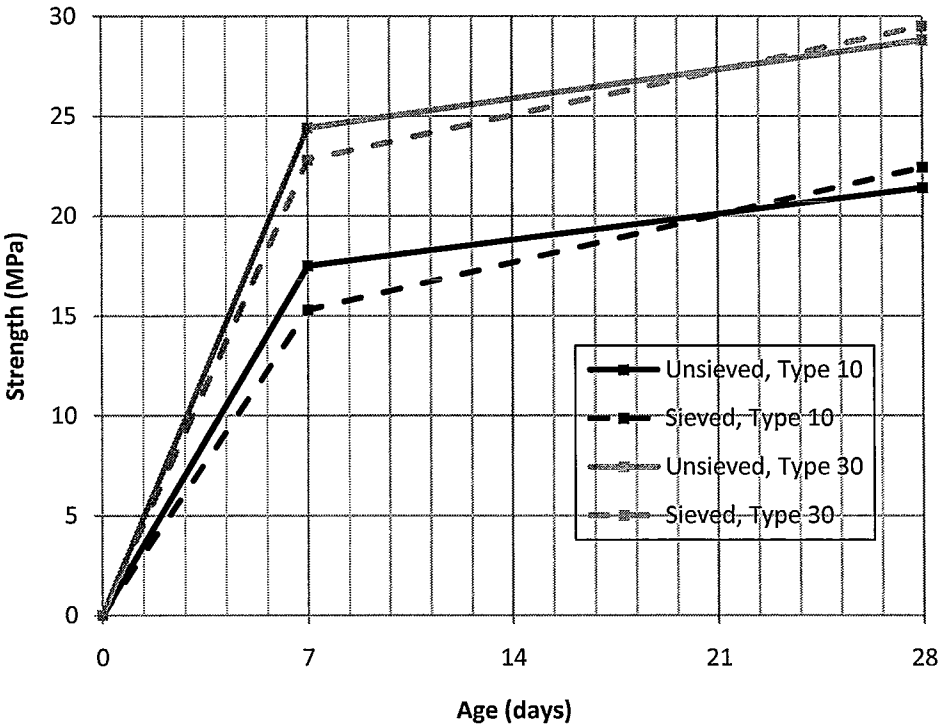

Figure 2-23: Comparison of Four Mortar Mixes

The difference between the mortar mixed using sieved mortar sand and from the mix using unsieved sand was negligible for both cement types. However, there was a 25% 28-day compressive strength increase in the mortar mixed using Type 30 (high-early strength) Portland cement. Typically, high-early strength and regular Portland cements, with the same water to cement (w/c) ratios, reach the same strength after 28 days (Johansen et al., 2006). The strength gain within the mortar cube specimens was attributed to the comparatively finer cement particles that exist within high-early strength Portland cement. It was thought that the finer particles would allow for a more thorough coating of the fine aggregate particles for the same weight of cement. The conical failure mechanism was consistent throughout testing (see Figure 2-24).

Figure 2-24: Typical Mortar Cube Failure Mechanism

2.5 Model Grout

There was a total of 7 grout mixes tested during the course of this research program. Details with respect to grout mixes and strengths can be found in this section. The main focus of this section was to examine the effect of aggregate size on compressive strength. There was also some examination and comparison to grout mixes of varying strengths developed at Drexel University by Abboud et al. (1990). The aggregate used within the model grout was required to be small enough that it would not provide difficulties when grouting the small cells of the model blocks. Previous half-scale grout produced for half-scale shear wall research programs carried out by Long (2006) and Shedid (2009) both used regular concrete sand as the grout aggregate without difficulty. Grout used for reduced-scale masonry specimens at Drexel University, in 1990, used masonry sand with aggregate larger than 1.25 mm removed. Type 10, regular Portland cement was used as the cement mix component for all grout mixes described in Table 2-13.

Table 2-13: Summary of Grout Mixes Tested

Mix #	Description of Mix	Mix Proportions (by weight) cement: lime: sand: water	Aggregate Selection	Slump (mm)	Compressive Strength** (MPa)
1	Drexel (GW)*	1 : 0 : 4.25: 1.29	masonry sand	255	20.3
2	Drexel (GN)*	1 : 0.04 : 2.81 : 0.84	masonry sand	265	27.0
3	McMaster	1 : 0.04 : 3.9 : 0.85	masonry sand	265	17.6
4	McMaster	1 : 0.04 : 3.9 : 0.85	concrete sand	270	19.5
5	McMaster	1 : 0.04 : 3.9 : 0.85	sieved concrete sand aggregate < 2.5 mm	262	22.0
6	Drexel (GW)*	1 : 0.04 : 3.9 : 0.85	sieved masonry sand aggregate < 1.25 mm	280	16.5
7	Drexel (GN)*	1 : 0.04 : 3.9 : 0.85	sieved masonry sand aggregate < 1.25 mm	275	19.8

**Grout Mixes, Drexel (GW) & (GN) were adopted from* (Abboud et al., 1990)
***Compressive strengths are the average of 3 non-absorptive cylinders tested as per ASTM C1019-08 (ASTM, 2008)*

The aggregate selected for the grouted assemblage and shear wall testing that will be described later in this report used concrete sand with aggregate larger than 2.5 mm sieved out. It was thought that this aggregate would provide an equivalent reduced-scale fine grout. The gradation of the model grout aggregate can be seen in Figure 2-25.

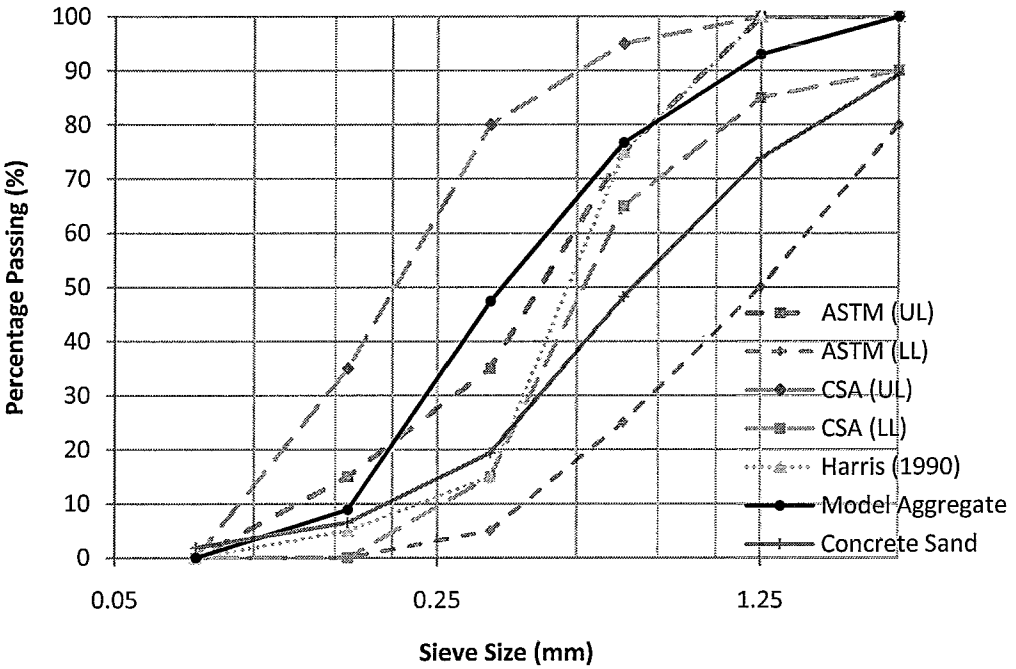

Figure 2-25: Gradation Curve of Aggregate Used in Model Grout

A summary of the compressive strengths of the various model grouts tested is provided in Table 2-13. Compressive strength test were carried out in accordance with ASTM C1019-08 (ASTM, 2008). In general, three different grout mixes, of varying strengths, were examined and then the impact of the aggregate size on the compressive strength was examined.

A comparison between the different grout mix strengths is shown in Figure 2-26. A trend of increasing strength with respect to aggregate size was noticed as the aggregate size is increased within both Drexel model grout mixes. The strength gain recorded as the aggregate size increased from sieved masonry sand to unsieved masonry sand was 23% and 36% for Drexel (GW) and (GN) mixes, respectively. The impact of the aggregate size on compressive strength is shown more clearly in Figure 2-27. As the aggregate size increased from

unsieved masonry sand to sieved concrete sand and finally to unsieved concrete sand the trend of the compressive strength related to each aggregate was increasing. However, the grout mixed using the sieved concrete sand had a higher compressive strength than the unsieved, going against the expected trend. Overall, there was a 12.8% compressive strength difference between the fine grout using regular concrete sand and the model grout using sieved concrete sand.

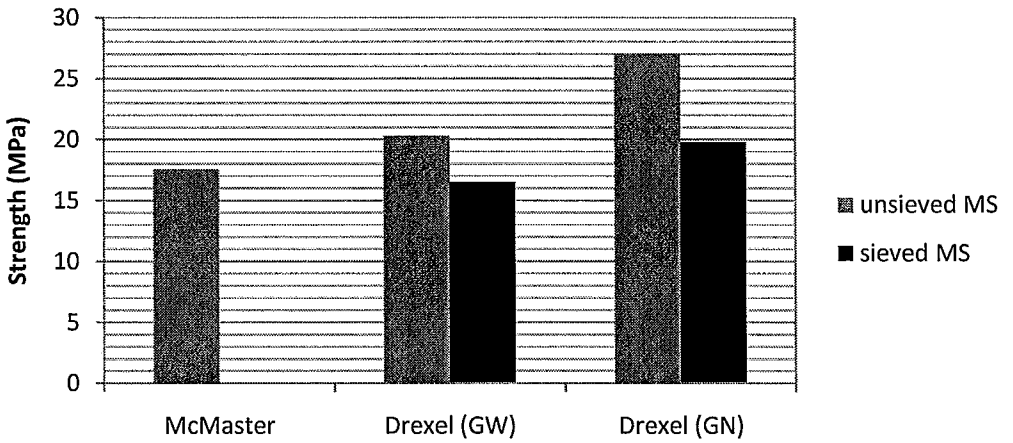

Figure 2-26: Comparison of Different Grout Mix Strengths

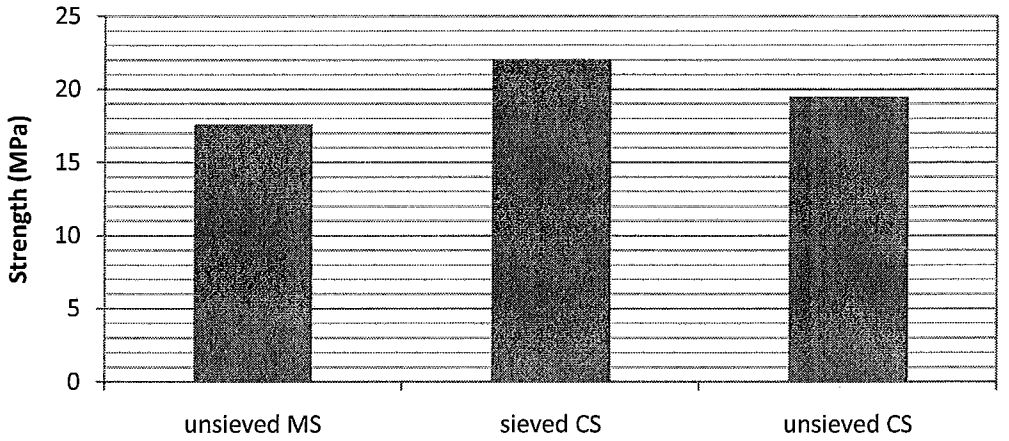

Figure 2-27: Impact of Aggregate Size on Compressive Strength of Grout

2.6 Model Reinforcing Steel

A deformed wire, D7, provided by Laurel-LEC steel in Brantford, Ontario was used to model the prototype steel used by Shedid (2006). The nominal area of the D7 deformed wire is 45 mm^2; this area corresponds to a full-scale bar with an approximate area of 405 mm^2 (in between a 20M and a 25M bar). The stress strain relationship of the model steel compared to regular No. 20 and 25 bars is shown in Figure 2-28. The deformed wire was tested in accordance with ASTM E111-04 (ASTM, 2004).

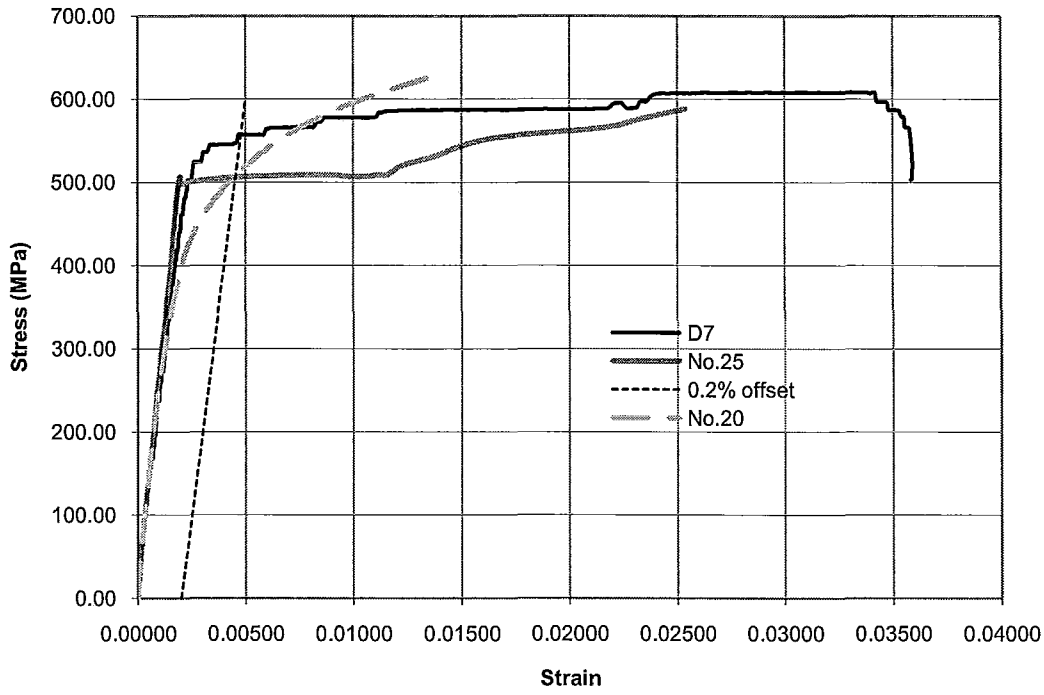

Figure 2-28: Stress-Strain Comparison of Model D7 to Prototype No.20 and No.25

The average tensile strength at yield of the D7 steel, from three tests, was 540 MPa with a C.O.V. of 1.4%. This compares well with the No. 20 and No. 25 yield stresses of 504 and 503 MPa, respectively (Shedid, 2006). The yield strength was determined by the 0.2% offset method shown in Figure 2-28. The strain of the D7 bar at yield, ε_{sy}, was 0.0027 and the maximum strain, ε_{su}, recorded at bar rupture was 0.035, approximately 13 times the yield strain. The elastic modulus, E_s, of both the model and prototype steel was 200 GPa (as shown in Figure 2-28).

A smooth wire, W1.7, was used as model horizontal reinforcing. The nominal area of the smooth wire was 11 mm^2. The prototype equivalent of this diameter bar would be a 10M reinforcing bar, with a nominal area of 100 mm^2. The stress strain relationship of the smooth wire compared to the prototype No. 10

rebar is shown in Figure 2-29. The average tensile strength of the W1.7 wire was 680 MPa. This was much higher than the prototype No. 10 rebar strength of 491 MPa as tested by Shedid (2006) but consistent with other available full-scale bars in Canada; Shedid (2006) used 25M bars with f_y = 625 MPa for one full-scale shear wall specimen in his research. The elastic modulus of both the model steel wire and the prototype rebar was 200 GPa. The shear wall specimens that will be described later in this research program were over designed in shear in order to allow for a more ductile, flexural response.

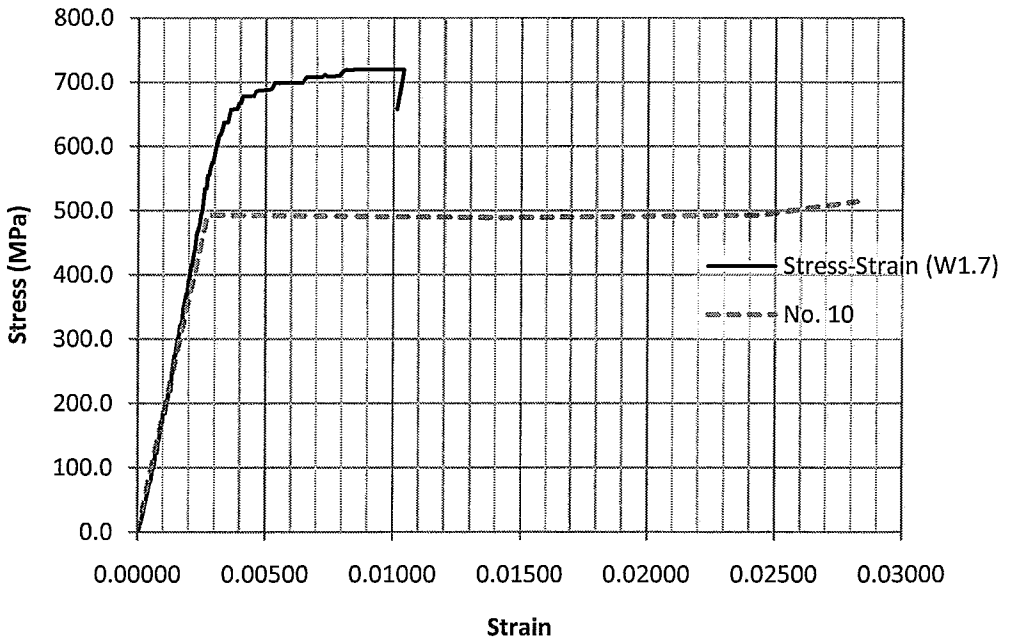

Figure 2-29: Stress-strain relationship of model W1.7 steel wire compared to No. 10 rebar

The different sizes of model reinforcing bars used throughout this thesis are shown in Figure 2-30. The diameter of each bar is shown for comparison purposes.

Figure 2-30: Model Reinforcing Bars Compared to 10M Rebar

2.7 Conclusions

The individual components that make up a reinforced concrete block shear wall include the block, mortar, grout and steel reinforcing. A successful reduced-scale model must be composed of individual elements with material properties closely corresponding to those from their respective full-scale prototypes. This chapter examined each individual model element and provided a comparison to its full-scale equivalent.

The non-structural material properties of the model block represented those of the full-scale extremely well. The difference in densities between the third-scale model and full-scale prototype block tested by Long (2006) was negligible. There was a 13% reduction in the model blocks absorption capability when compared to the prototype.

Unfortunately, the compressive strength of the model blocks used for the remainder of this research program was 54.2 MPa, over 100% stronger than the prototype blocks. However, as mentioned previously, there were two significant changes between the preliminary and final block production phases that ended up increasing the block strength. The blocks produced before the addition of the steel lip on the top of the mould were much closer to the prototype compressive

strength at 39.6 MPa. Had the cement to aggregate ratio been reduced to something more typical of a full-scale concrete block mix, the compressive strengths of the model blocks would have been much closer to the design strength of 25 MPa.

The impact of aggregate size on the compressive strength of mortar was negligible for both mixes using Type 10 (regular Portland) and Type 30 (high early-strength Portland) cements. However the use of Type 30 cement increased the average compressive strength of the mortar cubes by 25%. Based on the afore-mentioned fact, if Type 30 cement is used in mortar, the ratio of cement to aggregate can be decreased. However, using Type 10 cement will produce model mortar that is negligibly different than the prototype mortar, except for the obvious aggregate reduction necessary depending on the desired mortar joint height.

The impact of aggregate size on the compressive strength of grout was clearly shown as an increasing trend as the aggregate size increased. In general, the compressive strengths of the model grout related very well to the full-scale fine grout prototype. There was only a 12% difference in strength between the model and prototype grout.

The model reinforcing steel showed a good material correlation to the full-scale prototype steel. The modulus of elasticity of the steel used for both horizontal and vertical reinforcing was the same, 200 GPa. The tensile strength of the model vertical steel was approximately 8% stronger at yield and approximately 20% stronger at ultimate. The steel was not heat-treated as it had a similar stress-strain curve to the prototype steel (shown in Figure 2-28). In general, the model steel showed excellent correlation to the prototype vertical reinforcing up until approximately 10 times yield strain. The impact of the ultimate strain of the model steel will be discussed in greater detail with the shear wall tests described in Chapter 4.

3 ASSEMBLAGE TESTING PROGRAM

3.1 Introduction

A total of eighty third-scale assemblages were tested during the assemblage component of the experimental program. Sixty assemblages were designed to be tested in compression and twenty assemblages were designed to test shear strength of the model walls. All assemblages described in this chapter were constructed by a skilled mason. The primary goal of this phase of the experimental program was to provide a comparison to existing full-scale assemblage testing. After it was established that the assemblage characteristics were reasonably representative of those from full-scale specimens, a number testing variations, including mortar strength, grout strength, and the addition of vertical reinforcement, were carried out to fully analyse the behaviour of third-scale masonry to be used in cantilever shear walls.

The specific types of assemblages tested were based on the major load resisting mechanisms of a reinforced concrete masonry shear wall designed to exhibit flexural behaviour. Theoretically, a shear wall subject to an in-plane lateral load would carry the same shear load over the entire height of the wall while the two extreme ends of the wall are subject to either tensile of compressive forces depending on the direction of the overturning moment. A schematic of these forces is shown in Figure 3-1.

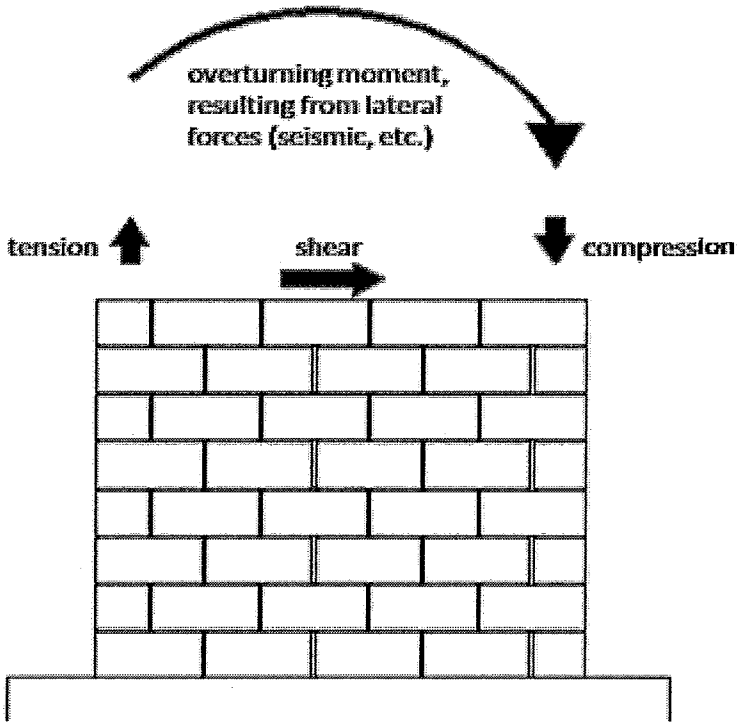

Figure 3-1: Typical Shear Wall Behaviour

Both shear and compression assemblage specimens are shown in their respective locations within a typical reinforced concrete masonry shear wall, in Figure 3-2, to illustrate the way they would be forced to respond to a typical overturning moment caused by lateral (in-plane) forces due to seismic excitation. The typical dimensions the assemblages have also been provided in Figure 3-2. The compressive prisms are four courses high by one block long (CSA S304.1, 2004), and the shear triplet specimens are 3 courses high (Drysdale and Hamid, 2005). The modified shear triplet shown in Figure 3-2 a) is rotated 90 degrees prior to be testing under compressive loading. More detail with respect to each prism is described later in this chapter.

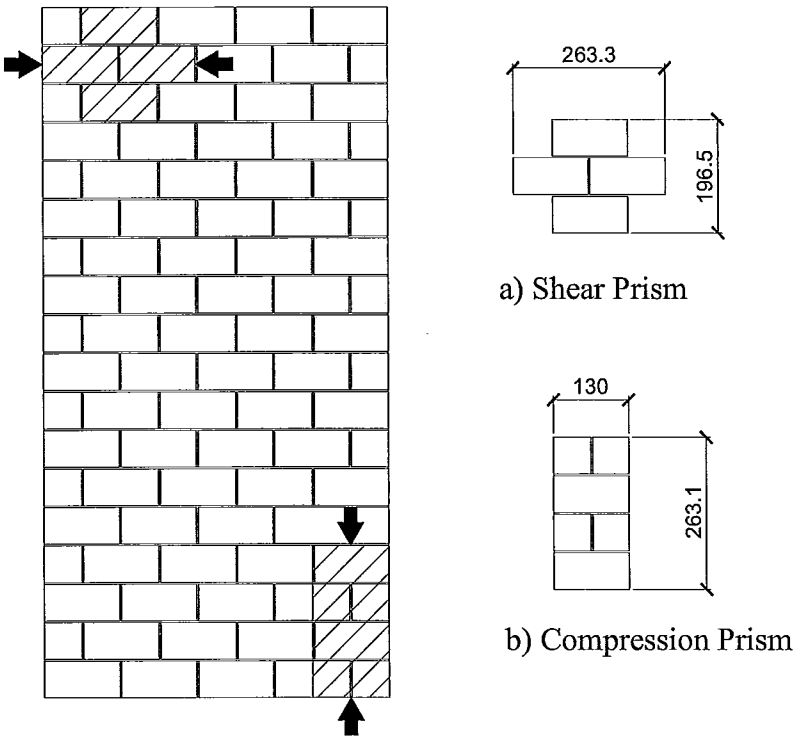

Figure 3-2: Model Prism Types and Dimensions

3.2 Compressive Strength

A total of sixty prisms were tested in compression. The effect of aggregate size in both mortar and grout on the compressive strength of the masonry assemblages was examined. The impact of increasing the vertical steel reinforcing ratio on the impact of compressive strength was also examined.

All prisms were constructed by a skilled mason and were designed using either two full stretcher blocks combined with 4 half stretcher blocks or 2 full end units combined with 4 half end units (see Figure 3-3). The resulting prisms were all four blocks high by one block long, providing an aspect ratio of two. It should

be noticed that, from Chapter 2, the compressive strength of the individual model concrete block units averaged 54.2 MPa. The specific details regarding the dimensions of the prisms constructed are outlined in Figure 3-3.

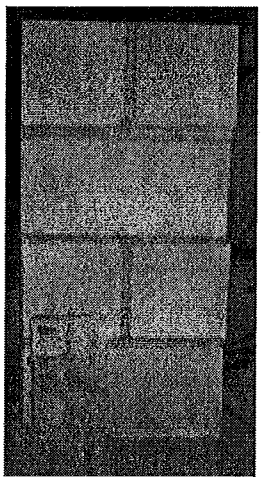

Figure 3-3: Third-scale Prism compared to Full-scale Prism

In general, there were three different types of prisms tested in compression: ungrouted, grouted and grouted-reinforced prisms. There were five specimens constructed and tested for each prism variation. In total there were 15 ungrouted, 30 grouted, and 15 grouted and vertically reinforced masonry assemblages tested in compression. Testing was carried out in accordance with ASTM standard C1314-07. The average strain was recorded for each prism using two linear variable displacement transducers (LVDTs), one on each side of the prism. The testing apparatus is shown in Figure 3-4. The specific material properties of interest within this phase of the research program were the compressive strength, the elastic modulus, and the strain at ultimate load for each prism variation.

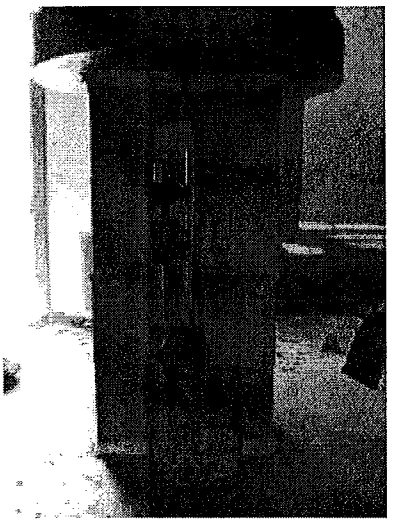

Figure 3-4: Prism in Axial Compression Testing Apparatus

3.2.1 Ungrouted Masonry Assemblages

The ungrouted specimens were created to compare the impact of mortar strength on the compressive strength as well as the impact of using end units instead of stretcher units within the assemblage. The details with respect to the ungrouted masonry assemblages are shown in the following table.

Table 3-1: Summary of Ungrouted Prism Specimens

Specimen	Mortar Strength	Grout mix		Grout Strength	Comments	Prism Comparison
UE1	31.9	none	-	-	end units	UU1
UU1	31.2	none	-	-	stretcher units	UE1, UU2, GU1
UU2	15.3	none	-	-	stretcher units	UU1

The results from the compressive strength tests are presented in Table 3-2. Each specimen listed in the table represents the average results of five ungrouted assemblages tested under compressive loading.

Table 3-2: Summary of Ungrouted Prism Compression Test Results

Specimen	Mortar Strength (MPa)	f'_m (MPa) [c.o.v. (%)]	ε_{mu}ult [c.o.v. (%)]	Measured E_m(MPa) [c.o.v. (%)]	Code (S304.1) E_m(MPa) [% difference]
UE1	31.9	42.4 [5.9%]	0.00230 [12.5%]	27853 [5.9%]	36016 [29% higher]
UU1	31.2	45.5 [5.9%]	0.00232 [7.0%]	28594 [14.2%]	38677 [35% higher]
UU2	15.3	37.3 [6.4%]	0.00237 [9.3%]	24104 [5.7%]	31742 [32% higher]

The average compressive strengths of the ungrouted prisms are much higher than the full-scale prototypes tested by Long (2006). Long recorded an average compressive strength of 23.0 MPa, using full-scale units. As can be noticed from Table 2-9, in Chapter 2, the average compressive strength of the prototype blocks used by Long (2006) was 24.4 MPa. As mentioned previously, the blocks used in the construction of these prisms had a compressive strength of 54.2 MPa, approximately 215% higher than the prototype blocks. The varying block strengths between the full-scale and model ungrouted prisms made it difficult to compare the strength results; it was for this reason that the prism strengths were compared to a mathematical model developed by (Koksal, Karakoc, and Yildirim, 2005) to compare the trend of material strength gain. The equation for ungrouted prism strength (f'_m) as a function of mortar strength (f_{mr}) and block strength (f_{bl}) follows:

$$f'_m = 1.57\, ln\,(f_{mr}) + 0.75\, f_{bl} \quad \text{(Koksal, et al., 2005);} \qquad \textit{Eq. (3-1)}$$

where $ln(x)$ = the natural logarithm of x,

Table 3-3: Experimental Comparison to Koksal's Model

Specimen	f'_{mr} (MPa)	f'_{bl} (MPa)	f'_m (MPa) [measured]	f'_m (MPa) [Koksal et al, 2005]
Third-scale model (UE1)	31.9	50.2	**42.4**	**43.0**
Third-scale model (UU1)	31.9	54.0	**45.5**	**46.0**
Third-scale model (UU2)	15.3	54.0	**37.3**	**45.0**
Full-scale prototype (Long, 2006)	24.4	24.4	**23.0**	**23.3**

As shown in Table 3-3, the mathematical model developed by Koksal et al. (2005) is quite accurate at predicting ungrouted prism strengths based on the individual material properties of the assemblage. The ability of the Koksal et al. model to predict the compressive strength of the third-scale assemblages with reasonable accuracy confirms the comparable material strength to prism strength between full-scale and third-scale unreinforced assemblages. It should be noted that the model does not rely heavily on the mortar strength to contribute to the overall compressive strength of the assemblage; this is illustrated by the fact that the mathematical model overestimated the prism strength of UU2. Experimentally, as the mortar strength increased by approximately 50%, from 15.3 MPa to 31.9 MPa, the compressive strength of the ungrouted prism increased by 22%. This trend is consistent with that found by Hamid, et al. (1985) with quarter-scale masonry assemblage testing. This fact indicates that mortar joints are of greater importance in reduced-scale masonry than in full-scale, where the joint sizes can be easily controlled during construction (Hamid, et al, 1985). A small absolute variation in a mortar joint in a reduced-scale model is equivalent to a much larger variation in a full-scale wall, and based on these results, impacts the ungrouted masonry compressive strength.

The compressive strengths of the ungrouted prisms constructed with stretcher and half stretcher units were 7.3% stronger than the prisms that were composed of end unit blocks. This was an expected result due to the slightly

lower compressive strength of the end units compared to the regular stretcher units.

The experimentally determined elastic modulus of the various ungrouted prisms were much lower than the CSA S304.1 prediction, this is a result of the extremely high block strength used in the construction of the assemblages.

The average stress-strain relationships for each of the three ungrouted compressive types are displayed in Figure 3-5. The stress-strain relationships of the three different series show good correlation as is evident from the properties examined in Table 3-2. There was a slight decrease in the measured elastic modulus between the specimens with varying mortar strength. As the mortar strength decreased 50%, the modulus of elasticity decreased by 15.7%.

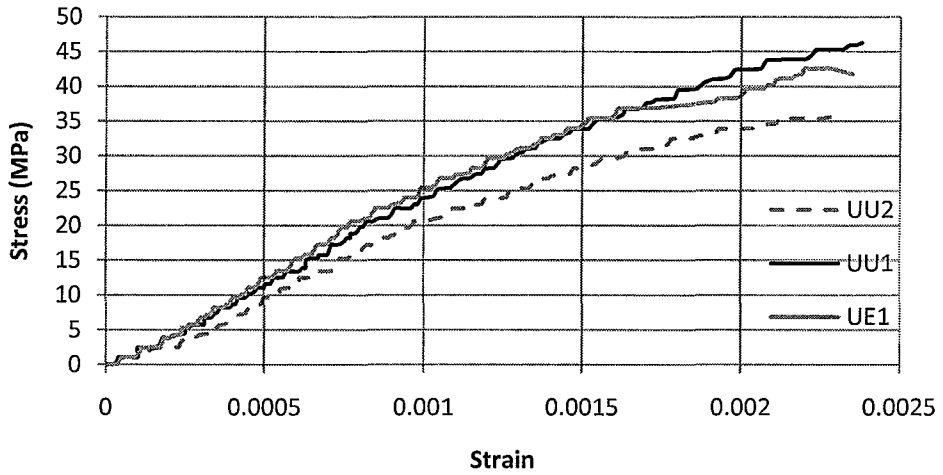

Figure 3-5: Ungrouted Prism Comparison

The failure modes were consistent between the three different types of ungrouted compression prisms. The typical failure mechanism was characterized by cracking down the side webs of the prisms (see Figure 3-6). In most cases, failure occurred very quickly in a brittle manner, making it difficult to record the descending portion of the stress-strain relationships shown in Figure 3-5.

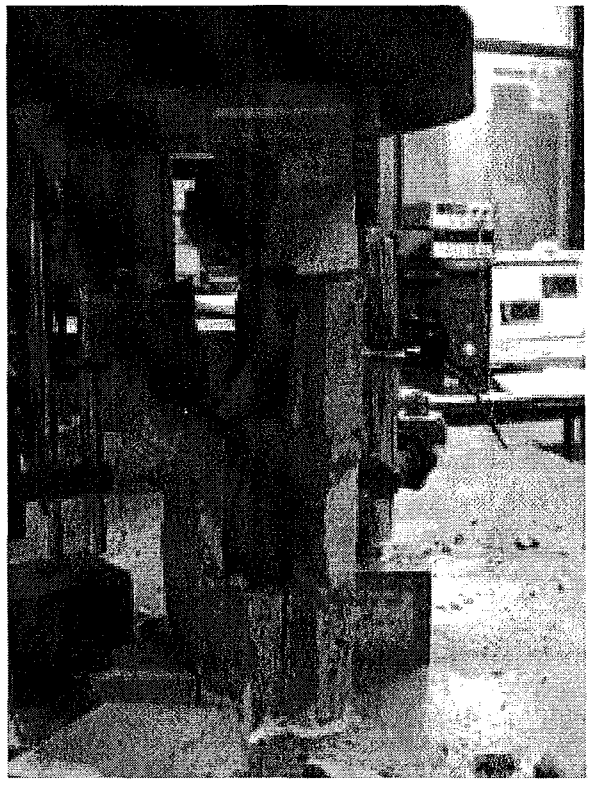

Figure 3-6: Typical Ungrouted Prism Failure Mechanism

3.2.2 Grouted Masonry Assemblages

The grouted compression prisms were designed in order to observe the effect of varying grout strengths, and more specifically the impact of the varying aggregate used within the grout mixes on the compressive strength of masonry, f'_m. The different specimen types have been summarized in Table 3-4. The grout mix numbers referenced in Table 3-4 relate back to the grout properties described previously in Chapter 2.

Table 3-4: Summary of Grouted Prism Specimens

Specimen	Mortar Strength	Grout mix		Grout Strength	Comments	Prism Comparison
GE1	31.9	McMaster	5	22.8	end units	GU1
GU1	31.9	McMaster	5	22.8	stretcher units	GR1 to GR3, GU2 to GU5
GU2	31.9	Drexel (GW)	1	20.3	stretcher units	GU1, GU3, GU4, GU5
GU3	31.9	Drexel (GN)	2	27.0	stretcher units	GU1, GU2, GU4, GU5
GU4	31.9	McMaster	3	17.6	stretcher units	GU1, GU2, GU3, GU5
GU5	31.3	McMaster	4	19.5	stretcher units	GU1, GU2, GU3, GU4

The experimental results from the grouted prism compressive strength tests have been summarized in Table 3-5. Each listed result represents the average of five assemblages tested.

Table 3-5: Summary of Grouted Prism Compression Test Results

Specimen	Grout Strength (MPa)	f'_m (MPa) [c.o.v. (%)]	ε_{mu} ult [c.o.v. (%)]	Measured E_m(MPa) [c.o.v. (%)]	CSA S304.1 E_m(MPa) [% difference]
GE1	22.8	28.1 [6.8%]	0.00221 [8.9%]	18,666 [8.5%]	23,847 [28% higher]
GU1	22.8	23.7 [4.1%]	0.00199 [10.9%]	16,509 [7.9%]	20,147 [22% higher]
GU2	20.3	22.2 [6.6%]	0.00205 [12.0%]	15,200 [9.7%]	18,882 [24% higher]
GU3	27.0	22.6 [7.9%]	0.00199 [8.2%]	16,228 [4.1%]	19,238 [19% higher]
GU4	17.6	21.3 [11.1%]	0.00196 [9.3%]	16,578 [9.9%]	18,120 [9% higher]
GU5	19.5	23.0 [5.4%]	0.00200 [15.9%]	16,277 [7.9%]	19,533 [20% higher]

In general, as the grout strength increased, the prism strength increased. The following graph displays the impact of grout strength on the compressive strength of both model and prototype prisms. The graph compares quarter-scale model and full-scale prototype testing completed by Hamid et al. (1985) to the third-scale results displayed in Table 3-5. As shown in Figure 3-7, as the grout strength increased there was a moderate increase in the total prism compressive strength. In general, the slope of the trend line for the third-scale data was found to be in between that of the quarter-scale model and full-scale prototype. This result was consistent with the trend found by Hamid (1985) in similar model to prototype comparative testing.

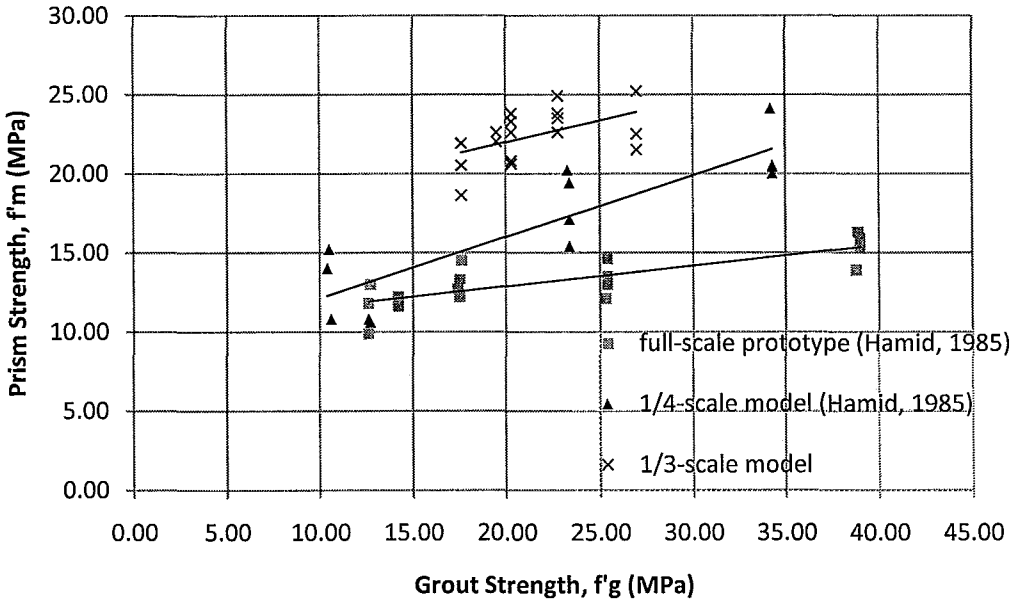

Figure 3-7: Effect of Grout Strength on Compressive Strength of Model and Prototype Prisms

As with the ungrouted prisms, the 54.2 MPa block strength was used in the construction of grouted compression prisms and as a result the use of a mathematical model was required to relate this third-scale model experimental

work to previous full-scale prototype testing completed by others. In this case an equation developed by Priestly (1986) was used to relate the third-scale model compressive strength to a full-scale prototype. Priestly's model was selected because it was used previously by Hamid et al. (1985) to validate the use of quarter-scale model blocks as a direct full-scale model. Priestly's equation for grouted prism strength (f'_m) as a function of grout strength (f_g), block strength (f_{bl}), and prism percent solid (α) follows:

$$f'_m = 0.59\alpha f_{bl} + 0.9(1 - \alpha) fg \quad \text{(Priestly, 1986);} \qquad \textit{Eq. (3-2)}$$

Priestly's analytical model was plotted against the trend lines from the third-scale model results described earlier along with previous experimental trends reported by Hamid et al. (1985) using quarter-scale model material in Figure 3-8.

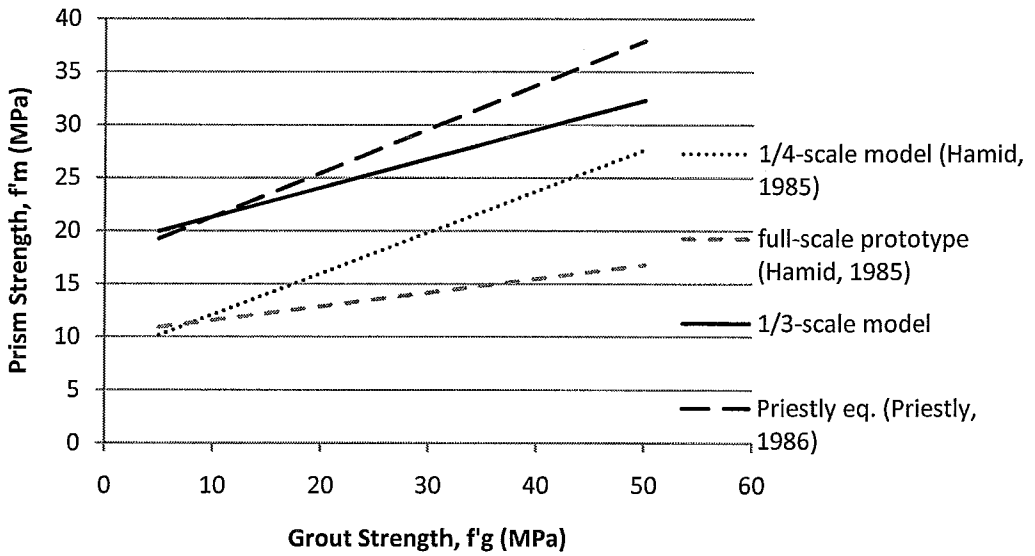

Figure 3-8: Grout Strength Trend Compared to Priestly's Equation

Figure 3-8 clearly shows that Priestly's equation reasonably represents the experimentally found trend of the third-scale model grouted prism strength

increase as grout strength increased. However, the compressive strengths of the third-scale model prisms tested were much higher than the full-scale prototypes. Priestly's model was used to compare the third-scale model grouted prism strength trend to the full-scale prototype trend found by Hamid et al. (1985). Figure 3-9 provides the strength trend comparison between quarter-scale model and full-scale prototype, tested by Hamid et al. (1985), the third-scale model strength trend and finally Priestly's equation plotted using f_{bl} = 25 MPa instead of f_{bl} = 54 MPa. The result was a trend that was very similar to the quarter-scale model testing performed Hamid et al (1985) and full-scale prototype by Drysdale and Hamid (1979).

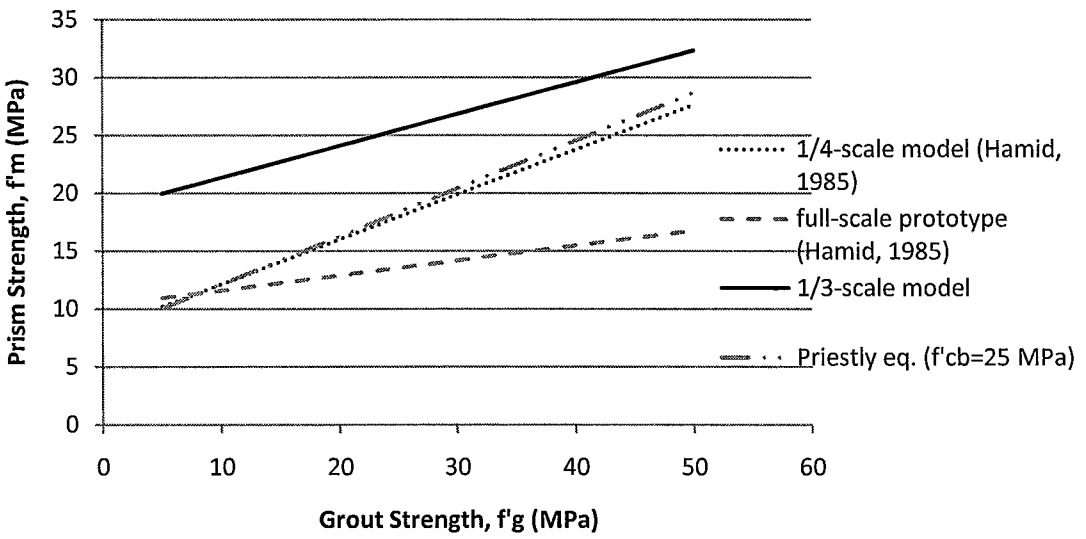

Figure 3-9: Model Grouted Prism Strength Trend Validation Using Priestly's Equation

No significant variation of the experimentally determined elastic modulus between the specimen variations was observed. The elastic modulus was, similar to ungrouted prisms; much lower that than the CSA S304.1 approximation due to the high compressive strength of the constituent blocks. The average stress-strain

relationships for each of the six grouted compressive prism types are displayed in Figure 3-10.

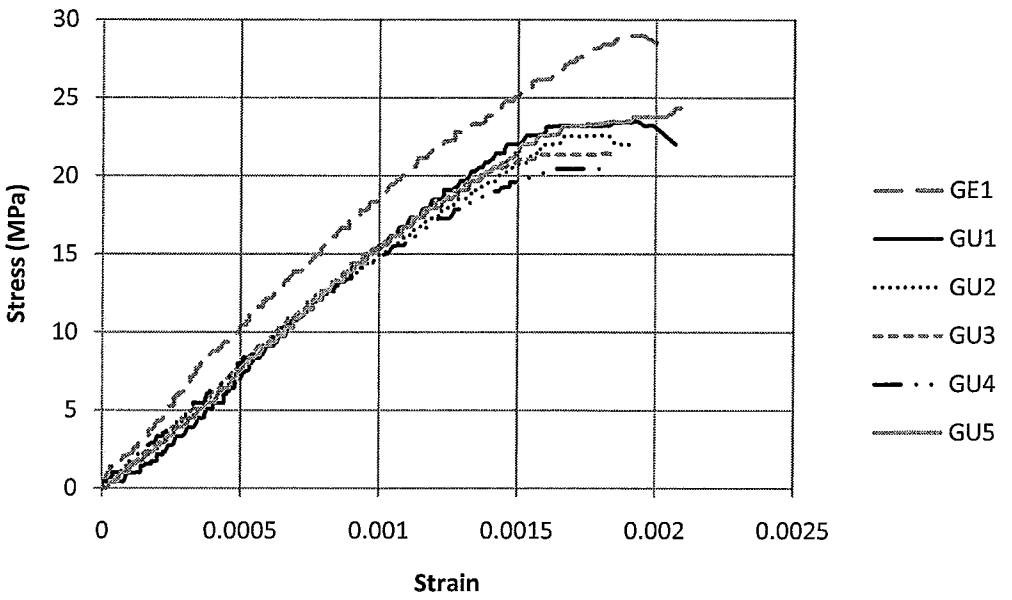

Figure 3-10: Grouted Prism Comparison

The stress-strain relationships of the six different series, with the exception of the specimens built with end units (GE1), showed good correlation in the elastic range as is evident from the properties examined in Table 3-5. The measured elastic modulus did not vary much as the grout strength increased. The average strain at ultimate stress was also very consistent between the five different grout mixes. One trend that has already been discussed was the impact of the grout strength on the compressive strength of the assemblage. In general, as the grout strength increased, the ultimate compressive stress of the various assemblages increased. This is clearly illustrated in the close-up of the stress-strain behaviour at ultimate as shown in Figure 3-11.

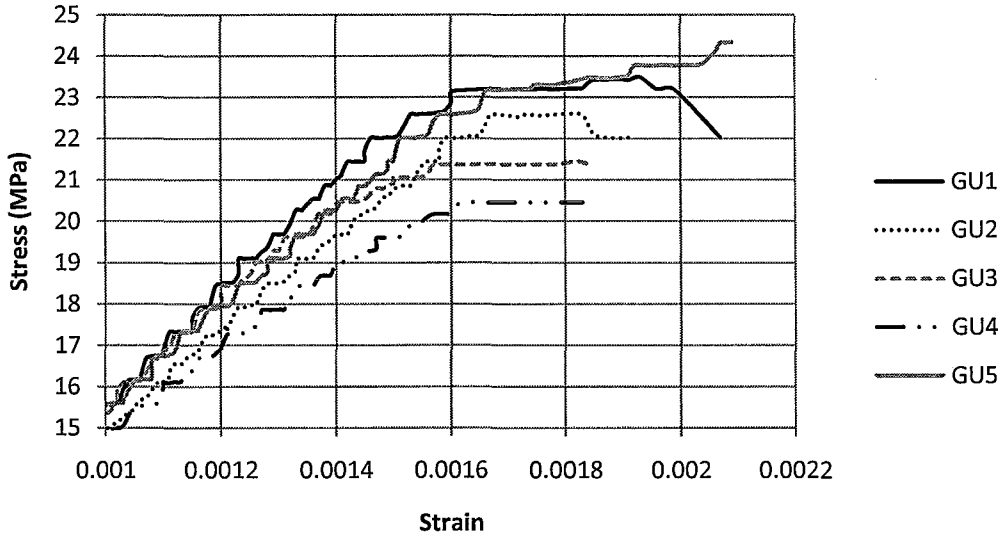

Figure 3-11: Close-up of Grouted Prism Comparison

The failure modes were consistent between the six different types of grouted compression prisms. The typical failure mechanism was characterized by tensile splitting with both vertical and diagonal cracking (see Figure 3-12). This failure mechanism corresponded well to previous model testing completed by Long (2006) and Hamid et al. (1985) as well as full-scale prototype failures (Drysdale and Hamid, 1979).

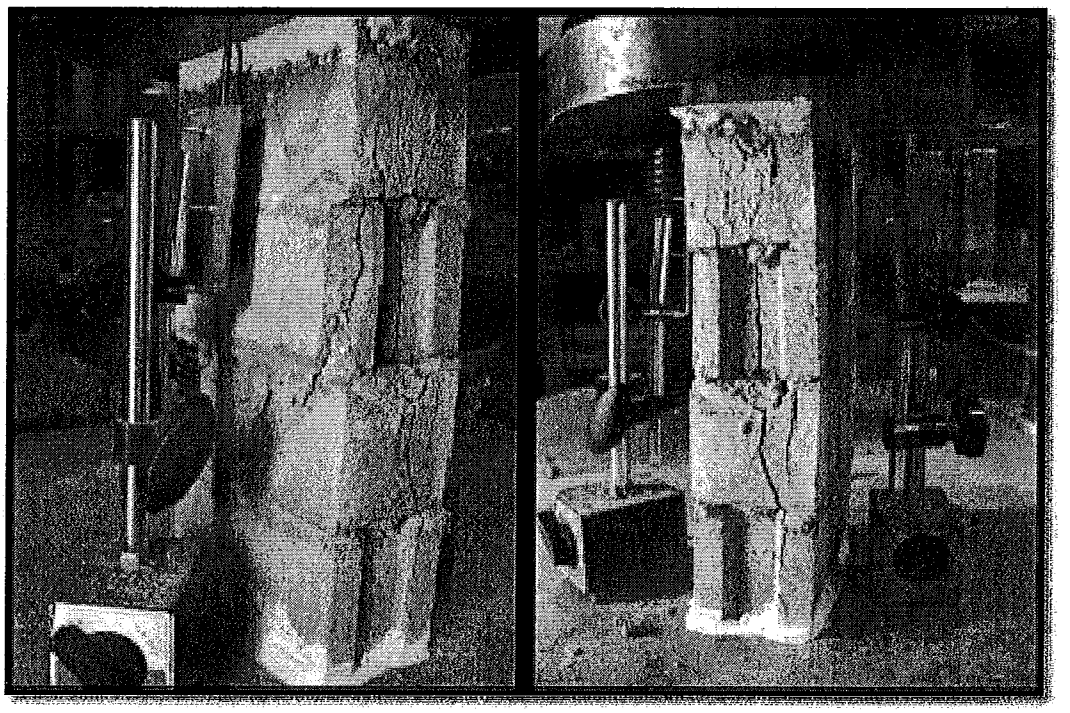

Figure 3-12: Typical Failure Mechanism of Grouted Prism

3.2.3 Grouted, Reinforced Masonry Assemblages

The vertical reinforcement is typically neglected when determining the compressive strength of masonry, as the former would typically buckle due to the lack of confinement inside a typical reinforced masonry wall cell. However, the effect of vertical reinforcement on the other material properties such as elastic modulus, E_m, and strain at ultimate stress, ε_u, has not been well quantified. The impact of vertical reinforcement on the stress-strain behaviour of concrete block masonry was explored in the following section in order to provide some insight into this issue. Three specimen types were tested with the percentage of vertical steel in each prism being the only varying parameter. A summary of the various specimens constructed are listed in Table 3-6.

Table 3-6: Summary of Grouted, Reinforced Prism Specimens

Specimen	Mortar Strength (MPa)	Grout mix #		Grout Strength (MPa)	Comments	Prism Comparison
GR1	26.9	McMaster	5	22.8	reinforced ρ_v= 0.28%	GR2, GR3, GU1
GR2	26.9	McMaster	5	22.8	reinforced ρ_v= 0.66%	GR1, GR3, GU1
GR3	26.9	McMaster	5	22.8	Reinforced ρ_v= 1.13%	GR1, GR2, GU1

Prisms were originally built by a skilled mason and they were later reinforced and grouted. The reinforcing bars were first welded to a 6.4 mm steel plate, and then fed through the prism empty cells so that the bottom plate could be mortared to the underside of the prism. The prism was then fully grouted from the top. After the grout had cured, a 6.4 mm steel top plate, that had been pre-drilled to allow the reinforcing bars to pass through it, was mortared to the top of the prism. The bars (now protruding through the top plate) were then welded to the top plate, and ground down flush. The process can be seen in Figure 3-13. There was some difficulty grouting the prisms as the presence of vertical bars made it difficult to properly vibrate the grout into the empty cells.

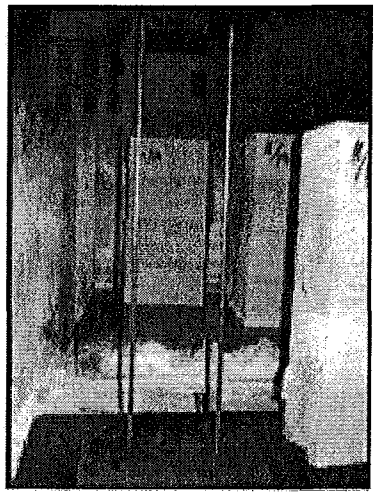

a) Reinforcing Bars Welded to Bottom Plate

b) Prism Reinforced Prior to Grouting

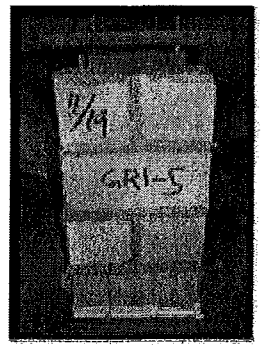

c) Reinforced Prism Fully Grouted

Figure 3-13: Construction Process of Reinforced Prism

The experimental results from the reinforced prism compressive strength tests have been summarized in Table 3-7, where each value represents the average of five assemblages tested.

Table 3-7: Summary of Grouted, Reinforced Prism Compression Test Results

Specimen	% reinforced	f'_m (MPa) [c.o.v. (%)]	ε_{mv} ult [c.o.v. (%)]	Measured E_m(MPa) [c.o.v. (%)]	$E_m / f'm$
GR1	reinforced $\rho_v = 0.28\%$	25.1 [8.5%]	0.00240 [9.9%]	12,338 [8.46%]	491
GR2	reinforced $\rho_v = 0.66\%$	25.3 [8.3%]	0.00249 [8.2%]	11,698 [15.4%]	462
GR3	reinforced $\rho_v = 1.13\%$	23.9 [3.6%]	0.00293 [28.4%]	10,482 [29.8%]	439
GU1	$\rho_v = 0\%$	23.7 [4.1%]	0.00199 [10.9%]	16,509 [7.9%]	697

No clear trend relating percentage of vertical reinforcement to compressive strength of assemblage was found. The strength of the assemblages was not positively increased impacted by the presence of the vertical bars. This was an expected result as the area displaced by vertical reinforcement was offset by the strength of the steel bars in compression.

The average experimentally determined modulus of elasticity dropped from 16,510 MPa to 12,340 MPa with the presence of the smallest percentage of vertical steel. As the percentage of steel reinforcing increased, the corresponding elastic modulus for each reinforced prism decreased. This decrease in stiffness as the amount of reinforcing increased was attributed to the loss of grout around the reinforcing bars, due to possible insufficient vibration of the test specimens. This loss of area can be seen in Figure 3-14. As the stiffness decreased the average strain at yield increased. The average stress-strain relationships between the three reinforced prisms have been plotted with grouted prism GU1 in Figure 3-15 in order to compare the impact of the vertical steel.

Figure 3-14: Grout Void around Reinforcing Bar

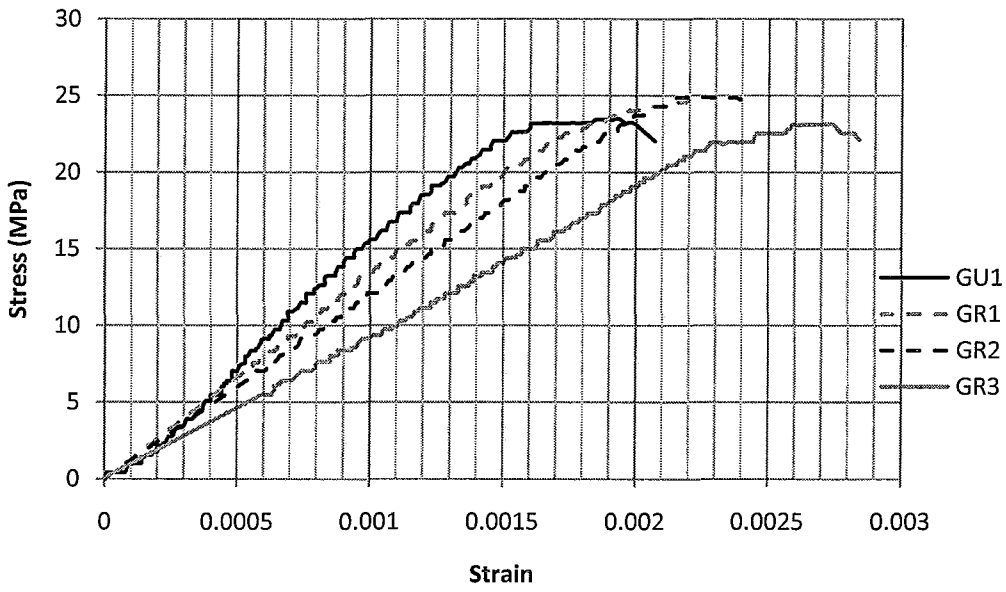

Figure 3-15: Grouted, Reinforced Prism Comparison

The failure mechanism for the grouted, reinforced prisms was characterized first by web cracking at the ends of the prisms, and finally the spalling of face shells at ultimate load. The spalling of the face shells was partly

attributed to the presence of the deforming steel bars. After the spalling of the face shells, failure occurred very rapidly in most cases. A few of the lightly reinforced specimens achieved a more ductile failure mode as the steel deformation did not seem to affect the face shells of the prisms. The typical failure mechanism has been shown in Figure 3-16.

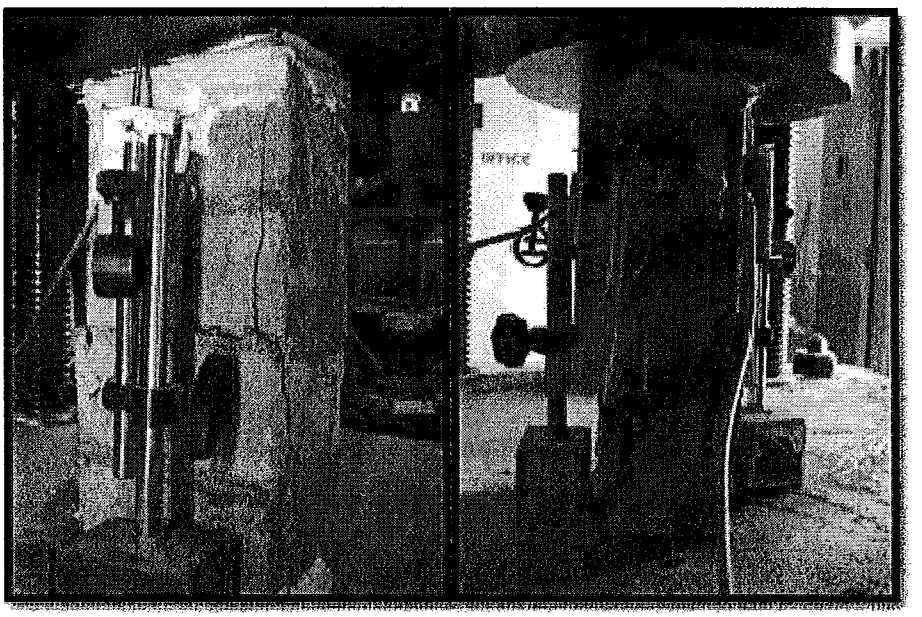

Figure 3-16: Typical Failure Mechanism of Reinforced Prisms

3.3 Shear Strength

The shear strength of the third-scale masonry assemblages was determined using the modified shear triplet method as described in previous research by Hamid (1990). The prism configuration is shown in Figure 3-17; the presence of a gap (double the typical mortar joint thickness) in the middle of the specimen allows for the shear failure along bed mortar joints to occur. The prisms consisted of four full stretcher blocks and were rotated 90 degrees to be tested in compression in order to achieve the desired shear failure along the mortar joints.

The compression testing apparatus used for each of the modified shear triplet specimens is shown in Figure 3-18.

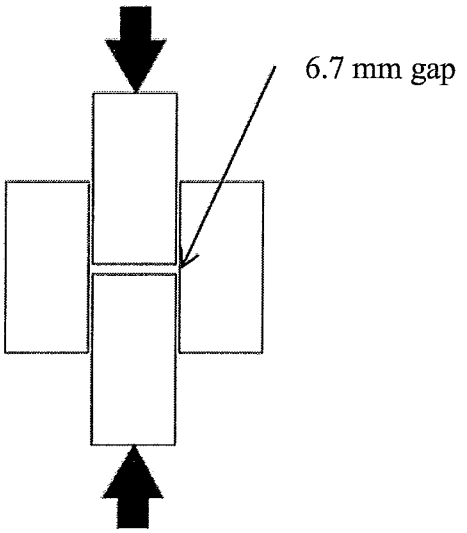

Figure 3-17: Configuration of Model Shear Specimen

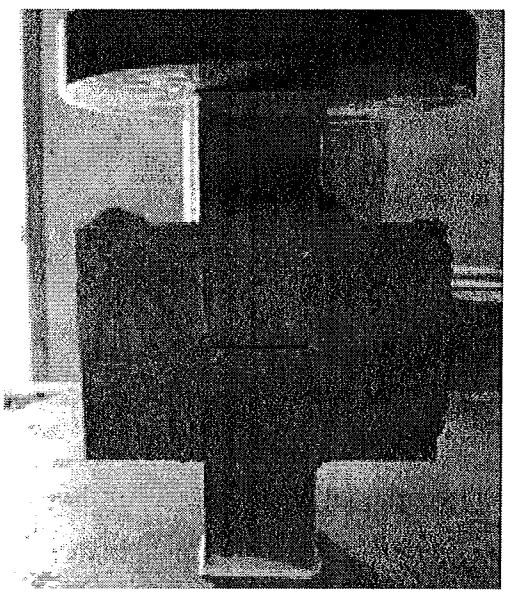

Figure 3-18: Shear Triplet Prism in Loading Apparatus

The average shear stress (τ) was calculated as a function of the applied load (P) and the net contact area (A_{net}) between two blocks for ungrouted specimens and the gross area (A_{gross}) for grouted specimens and using the following equation:

$$\tau = P/2A; \qquad (Eq.3\text{-}3)$$

A total of four prism variations tested in this manner, each variation consisted of five repetitions bringing the total amount of the shear specimens tested to twenty. The first ten specimens were ungrouted with varying mortar strengths while the last ten specimens were grouted with varying grout strengths. The specific details with respect to the different shear specimens are described in Table 3-8.

Table 3-8: Summary of the Modified Shear Triplet Properties

Series	Mortar Strength (MPa)	Grout Compressive Strength* (MPa)	Grout Tensile Splitting Strength (kPa)
U1	15	---	---
U2	31	---	---
G1	31	16	1105
G2	31	20	1210

** Based on the average of 3-100 mm x 200 mm non-absorptive cylinders*

3.3.1 Ungrouted Shear Triplet Specimens

The results from the ungrouted shear triplet specimen testing have been summarized in Table 3-9. Series U2, was constructed with a mortar that was about half (48.4%) of the average compressive strength of that used in the remaining specimens. The impact of the mortar strength reduction was a decrease in shear strength of 44%, from 0.52 MPa for U1 to 0.29 MPa for U2. All of the ungrouted shear triplet specimens had a similar failure mechanism characterized by a shear failure of the bed joints (Figure 3-19). The mode of failure was in

agreement with both full-scale prototype testing carried out by Drysdale et al. (1979) and quarter-scale testing completed by Hamid and Abboud (1987). This was an expected result for ungrouted shear specimens, as the major shear stress resisting force was the mortar bed joint between model blocks. The ungrouted shear specimen results have been summarized in Table 3-9.

Table 3-9: Summary of Ungrouted Shear Triplet Testing

Specimen	τ of U1 (MPa)	τ of U2 (MPa)
1	0.577	0.219
2	0.508	0.289
3	0.554	0.335
4	0.439	0.346
5	---	0.277
Average (kPa)	**0.520**	**0.293**
C.O.V. (%)	**11.7 %**	**17.3 %**

Shear Strength (τ) based on A_{net}=4,330 mm^2

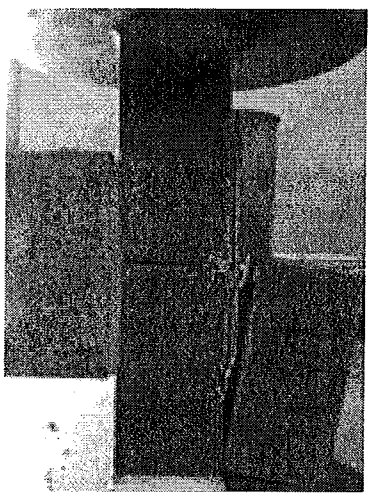

Figure 3-19: Typical Failure Mechanism of Ungrouted Shear Triplet

3.3.2 Grouted Shear Triplet Specimens

The results from the grouted shear triplet specimens have been summarized in Table 3-10. Series GU2 was constructed with a grout tensile splitting strength that was 9.5% stronger than the grout used in series GU1, and the resulting shear strength increase was approximately 8.1%. The typical grouted shear failure mode was initiated by cracking in the mortar bed joints followed by interior grout column cracking propagating to the face shell of the bottom block in the prism, see Figure 3-20. The observed failure mechanism of the grouted shear specimens was consistent with full-scale testing completed by Hamid, Drysdale and Heidebrecht (1979) and the quarter-scale testing by Hamid (1986).

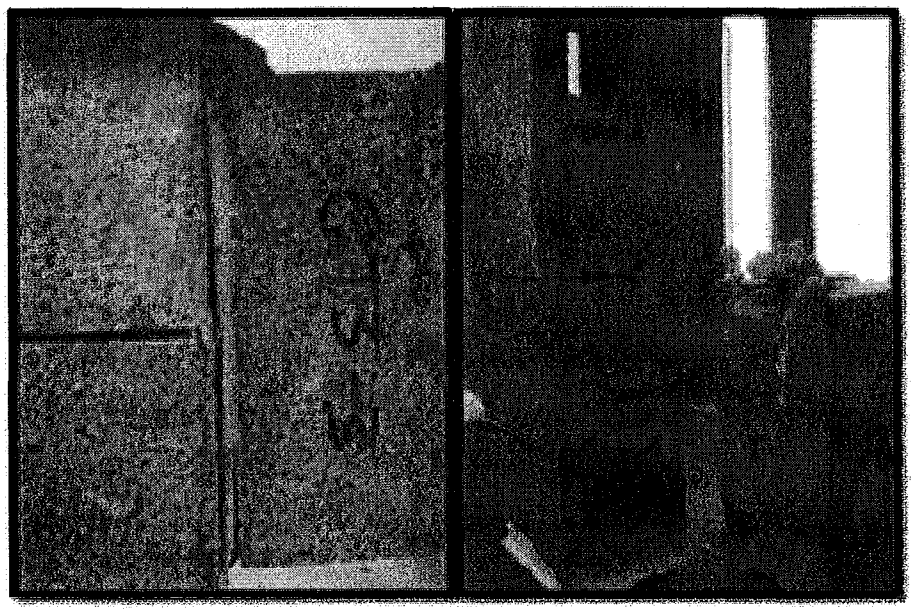

Figure 3-20: Typical Failure Mechanism of Grouted Shear Triplet Prism

Table 3-10: Summary of Grouted Shear Triplet Testing

Specimen	τ of G1 (kPa)	τ of G2 (kPa)
1	626	959
2	888	684
3	479	786
4	697	626
5	844	---
Average (kPa)	**707**	**764**
C.O.V. (%)	**23.5%**	**19.1%**

Shear Strength (τ) based on A_{gross} = 7,820 mm^2

The recorded shear strength of the grouted shear prism samples, G1, have a large C.O.V. that is reduced from 23.5% to a much more reasonable 16.1% with the exclusion of specimen G1-3 which was considered to be an outlier at less than 70% of the average shear strength of the 5 specimens. The comparatively low shear strength of specimen G1-3 was attributed to inadequate vibration of the grouted cores that lead to grout voids within the specimen.

The impact of the splitting shear strength of grout on the average shear strength of the prism has been plotted in Figure 3-21. The shear strength of the prism gradually increases as the splitting shear of the grout increases. Grouting clearly increased the average shear strength of the assemblages. Figure 3-21 presents a comparison of the ungrouted shear assemblages and the grouted assemblages of varying splitting shear strengths.

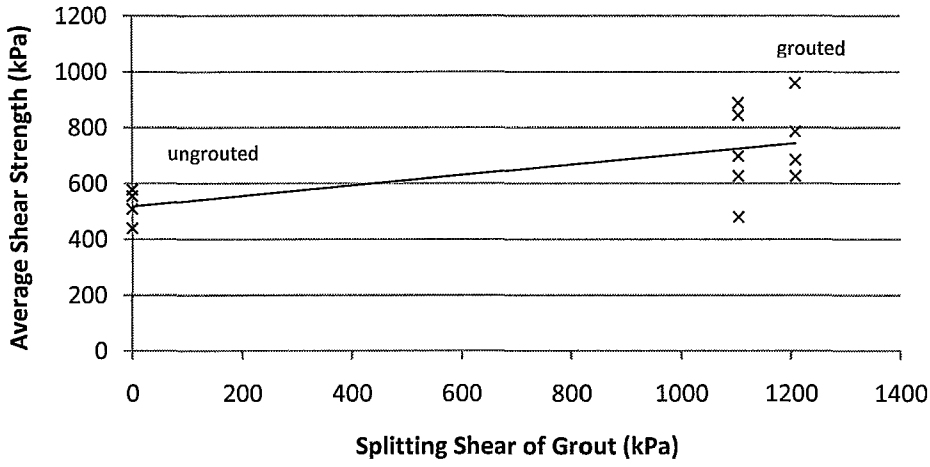

Figure 3-21: Effect of Grout on Joint Shear Capacity

The results of the model shear triplet prism specimens have been compared to full-scale prototype testing in Figure 3-22 and in Figure 3-23 to observe the shear strength trend as the splitting shear of grout increases. The third-scale model shear triplet specimens showed excellent correlation to both the full-scale prototypes tested previously by Drysdale et al. (1979) and to the quarter-scale model specimens. It should also be noted the unlike the compressive prisms, the shear triplet specimens corresponded well to full-scale prototypes without the need to use mathematical modelling to relate them.

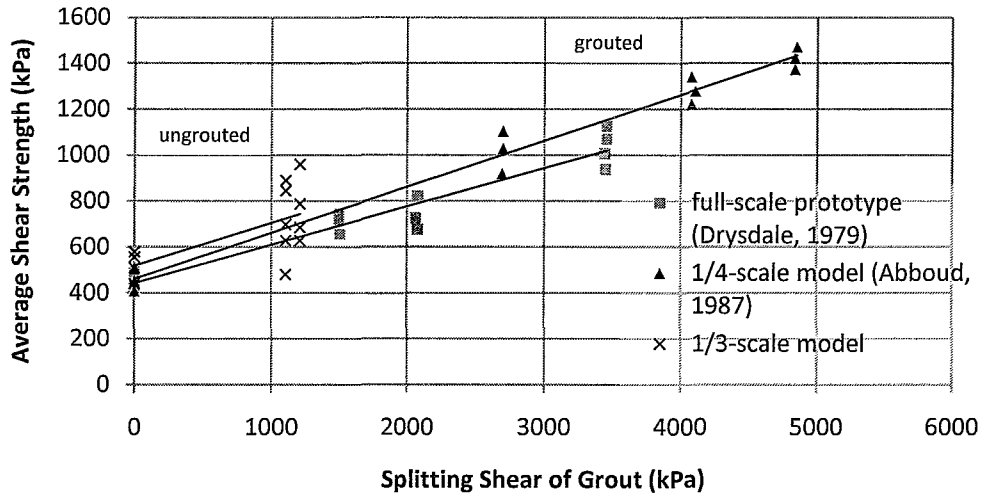

Figure 3-22: Shear Strength Comparison to Full-scale Prototype

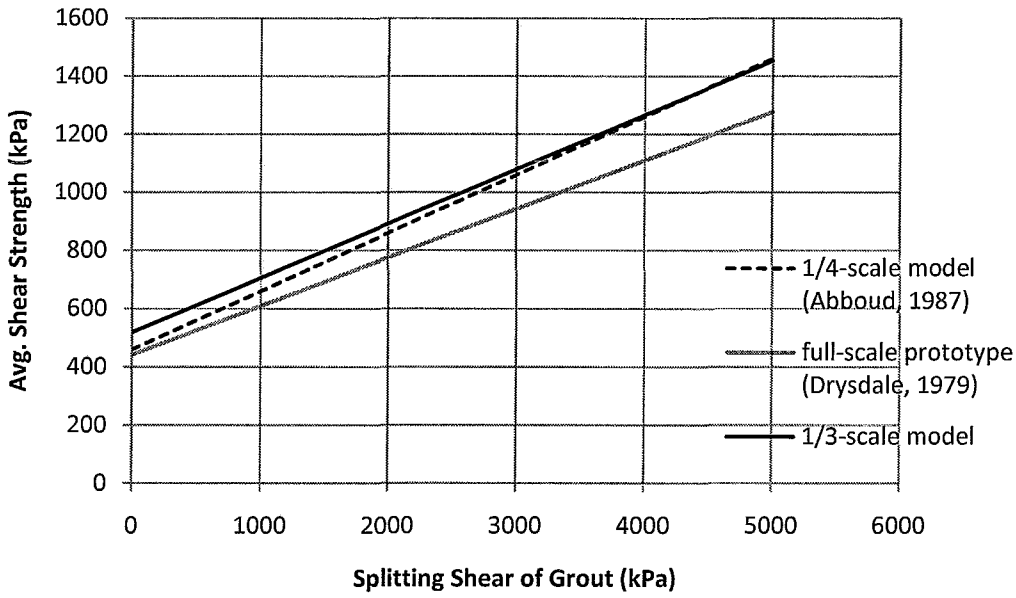

Figure 3-23: Model Shear Strength Trend-line Comparison

3.4 Conclusions

A total of eighty assemblages were tested in this phase of the research program. Sixty prisms were tested in compression and twenty modified triplets were tested in shear. Both types of assemblages were selected as the most critical assemblage components of a reinforced masonry shear wall.

The ungrouted prisms tested under compressive loading produced a high compressive strength when compared to the prototype testing completed by Long (2006). The strength variation was attributed to the use of individual blocks with a significantly higher compressive strength than the prototype blocks. An analytical model developed by Koksal et al. (2005) that related ungrouted prism strength of to the individual material strengths of the block and mortar constituents was used to compare the model ungrouted prisms to the prototype prisms tested by Long (2006). The model provided an excellent prediction of the compressive strength of the ungrouted prisms using the high model block strength of 54.2 MPa. The fact that the equation developed by Koksal et al. (2005) was able to predict the compressive strength of the model ungrouted assemblages suggests that third-scale model block masonry can be used as a reasonable direct model as long as the individual components are of similar individual strengths.

The model testing illustrated the importance of mortar joints in unreinforced masonry assemblage compressive strength. Koksal's equation did not provide an accurate representation of the compressive strength of the ungrouted compressive strength of the specimens with the lower mortar strength. Koksal's model did not place much emphasis on mortar strength as full-scale prism strength is typically a function of the block strength. The mortar strength has much more of an impact on the compressive strength of the ungrouted model assemblages than it did on the prototype assemblages used by Koksal to create the mathematical model, illustrating the importance of mortar joints in reduced-scale

masonry. This fact reinforces the findings of the study on the quarter-scale model masonry conducted by Hamid et al. (1985).

The model testing of grouted compressive assemblages illustrated the impact of grout strength on the compressive strength of the prism. In general, as the compressive strength of the grout increased, the compressive strength of the grouted assemblage increased proportionally. The strengths of the model grouted assemblages were higher than the prototypes tested by Drysdale and Hamid (1979). The high strengths of the model assemblages was again attributed to the use of a 54.2 MPa block instead of the 20 to 25 MPa block used in prototype testing. An equation developed by Priestly (1986) was used to relate the compressive strength of the third-scale model units to full-scale prototypes and the result showed reasonable correlation between the third-scale model and the prototype grouted assemblages. All grouted compressive prisms tested were constructed with the same mortar strength for consistency; however, as a result this did not facilitate studying the impact of the mortar strength on the model grouted masonry assemblages. It was assumed that, similar to full-scale specimens, grouted model assemblage strength would be a function of the grout strength and the block strengths.

The ungrouted shear specimens were tested in order to observe the impact of varying mortar strengths on the model shear strength of the assemblages. As the mortar strength was decreased by 48%, the corresponding shear strength of the assemblage was reduced by 44%. Similar to the compression prisms, the importance of masonry strength and mortar joint consistency is of significant importance when considering ungrouted model assemblages.

The grouted shear specimens were tested to compare the impact of grout splitting shear strength on the shear strength of the assemblages. As the splitting shear strength of grout increased by 9.5%, the shear strength of the assemblages increased by 8.1%. The trend of increasing shear strength with respect to grout

splitting strength was compared to previous reduced-scale testing by Abboud and Hamid (1987) and to full-scale prototype testing by Drysdale and Hamid (1979) with excellent correlation.

In conclusion, the results of the third-scale model compression and shear assemblage testing, which showed similar strength characteristics as the prototype assemblages tested by others, clearly demonstrated the potential of the third-scale masonry to act as a direct model for full-scale masonry testing. However it should be noted that although strength trends of model prisms were correlated to full-scale prototype testing data with reasonable success, model prisms with a more representative block compressive strength should be used in order to confirm the ability of reduced-scale masonry to act as a direct model.

4 SHEAR WALL TESTING PROGRAM

4.1 Introduction

Two reduced-scale shear walls were constructed to provide a correlation between the results obtained through previous full-scale experimentation at McMaster University. The walls were designed to exhibit flexural failure and represent a direct third-scale model of the prototype walls constructed and tested by Shedid (2006). The specific details with respect to the two walls tested will be described in this chapter. The results from the experimental testing can be found in the following chapter.

4.2 Design of Shear Wall Specimens

The shear walls were modelled after two full-scale shear walls that were designed to exhibit flexural failure. The aspect ratio (height to width ratio) for both walls constructed was 2.0. The actual height and thickness dimensions selected to produce that aspect ratio were based on ensuring that the compression zone at the wall toe extended further than one cell. The specific details related to the two shear wall specimens can be found in Table 4-1. The model specimen information has been presented in bold text where as the full-scale prototype information has been italicized.

Table 4-1: Wall Test Program

Wall No.	f'_m	Wall Dimensions		Vertical Reinforcement			Horizontal Reinforcement	
		Length	Height	No. & Size	A_v	ρ_v	Spacing	ρ_h
	(MPa)	(mm)	(mm)	of bars	(mm^2)	(%)	(mm)	(%)
1	**22.5**	**600**	**1200**	**5 - D7**	**45**	**0.60**	**133.3**	**0.13**
	15.2	*1800*	*3600*	*5 - No. 25*	*500*	*0.73*	*400*	*0.13*
2	**22.5**	**600**	**1200**	**9 - D7**	**45**	**1.07**	**66.7**	**0.26**
	15.2	*1800*	*3600*	*9 - No. 25*	*500*	*1.31*	*200*	*0.26*

Although the third-scale model specimens were designed to mimic the exact material properties of the full-scale specimens constructed by Shedid (2006) there were some small variations highlighted in Table 4-1. The value of f'_m of the model shear walls was 48% greater than the full-scale prototype walls. The percentage vertical steel used in the third-scale model walls was 18% lower than the full-scale walls. The difference between the amount of vertical steel between the model and prototype walls was partly due to the difference in tensile yield strength of the 25M bars compared to the D7 deformed wire. The average yield strength of the 25M bars was 503 MPa (Shedid, 2006) while the average D7 bars were 540 MPa, a difference of approximately 8%. More information with respect to the individual material properties used in the construction of the third-scale model shear walls will be discussed in Section 4.4. The elevations of the third-scale model walls are shown in Figure 4-1.

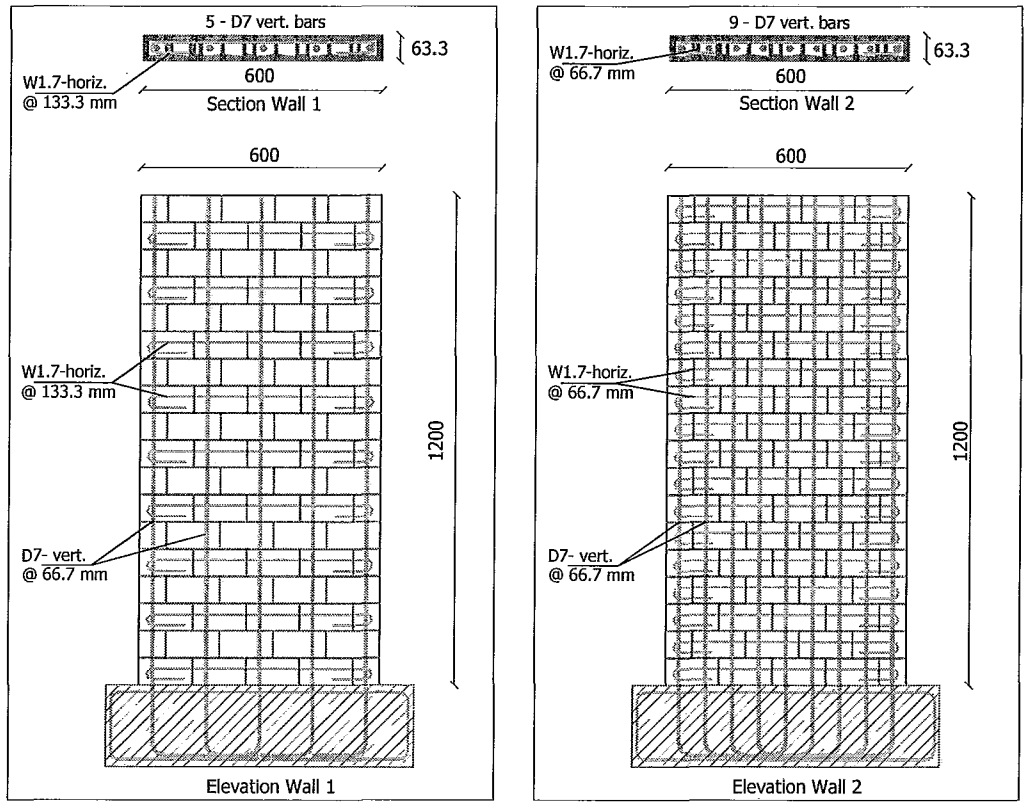

Figure 4-1: Shear Wall Reinforcing Details

4.3 Construction of Shear Wall Specimens

The shear wall construction details including: base beam design, the instrumentation of internal steel reinforcing, the work completed by the skilled mason and finally the grouting of the specimens are presented in this section.

4.3.1 Wall Base Construction

The base was of specific importance as it acted as the mechanism through which the shear wall is fixed to the strong floor of the lab. The base depth was designed to allow adequate length for full bond development of the tensile reinforcement used in the wall specimens. In this case it was decided that the vertical reinforcing bars would be bent at 90 degrees to ensure adequate

anchorage and development length. The potential complexities associated with a rebar splice in altering the flexural behaviour of the wall were eliminated by continuing the vertical rebar the entire height of the wall.

The concrete base was 300 mm tall x 600 mm wide x 1,000 mm long and was reinforced with 5-10M bars at the top and bottom and with 10M shear stirrups spaced at 333 mm (see Figure 4-2) to minimize cracking as the beam was stressed during testing. Six 38 mm diameter plastic tubes were inserted into the slab form to allow for post tensioned rods used to fix the shear wall to the test test-up. The plastic tubes were held in place by plywood planks on the top of the slab form. The vertical reinforcing was tied in place to the shear stirrups within the base beam slab and then held by wooden guides to ensure that the bars remained at their required even spacing.

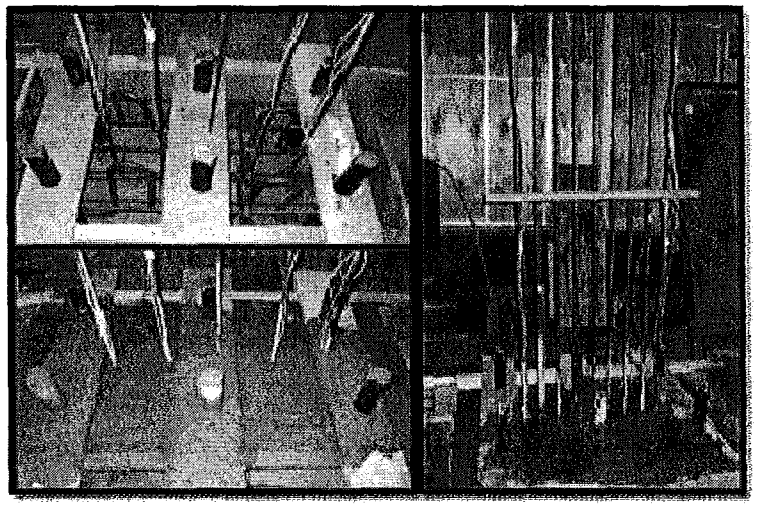

Figure 4-2: Base Beam Construction

4.3.2 Wall Construction

Two third-scale model shear walls were constructed consisting of 18 courses; each course was 4.5 blocks long. The wall construction took a skilled mason a total of three days. The blocks were fed over the top of the vertical

reinforcing as the reinforcing was imbedded into the concrete base. The blocks used in the construction of the shear wall specimens had 10 mm x 30 mm rectangular notches taken out of their side webs to aid in the placement of the horizontal steel (see Figure 4-3).

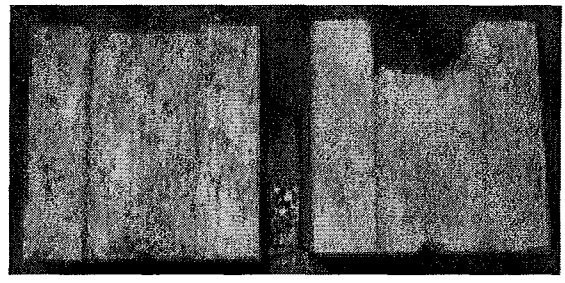

Figure 4-3: Notch in Side Web of Model Blocks

Wall 1 had one horizontal W1.7 bar placed every other cell. The notched blocks were only used for courses that required a bond beam. Wall 2 had one horizontal bar placed in every course. The horizontal reinforcement was bent around the D7 vertical reinforcing to form hook and was returned back into the bond beam at 180° for a length of 100 mm. It became clear at the time of construction that, due to the small cells present in the model blocks, it may be difficult to grout; specifically with the heavily reinforced Wall 2. A shear wall cell, prior to grouting highlights this congestion in Figure 4-4. This issue of congestion was easily overcome during the grouting of the specimens through the use of a very workable grout (slump > 250 mm) and through careful vibration of the grouted cells. In general, six courses were laid each day. After each day of construction, the walls were grouted up to half of the top course to avoid a cold joint. Following this construction technique the entire construction process took six days.

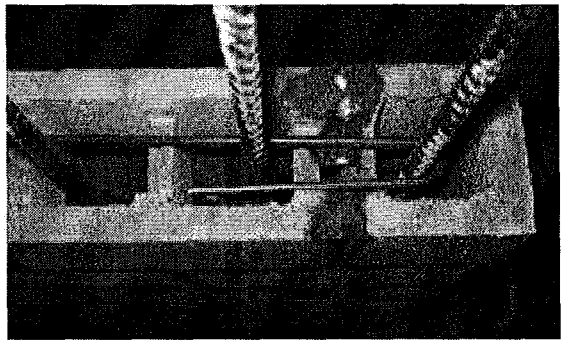

Figure 4-4: Wall 2 Cell Prior to Grouting

After the construction of the shear wall specimens, a concrete loading beam was poured on top of the walls. The concrete loading beam was to act as a medium to transfer the lateral loading from the loading actuator to the shear wall.

4.3.3 Grouting of Wall Specimens

The shear wall specimens were grouted in three stages to ensure that there were no voids present within the grouted cells. During each stage of grouting, 5.5 courses were grouted. The top course of each phase was only half filled with grout to provide a shear key between the different phases of wall. The shear wall is shown just after grouting in Figure 4-5. As the wall specimens were grouted, the mortar joints and some face shells turned darker as a result of moisture absorption. The grouted cells were vibrated with a pencil vibrator in order to adequately fill the voids. Extreme care had to be taken as the grouted cells were vibrated in order to ensure that the 25.4 mm diameter vibrator head did not come into direct contact with the interior face shell of the block. In order to prevent that issue a 3.8 mm diameter bar was attached to the vibrator head to aid in the vibration process, this attachment can be seen in Figure 4-6.

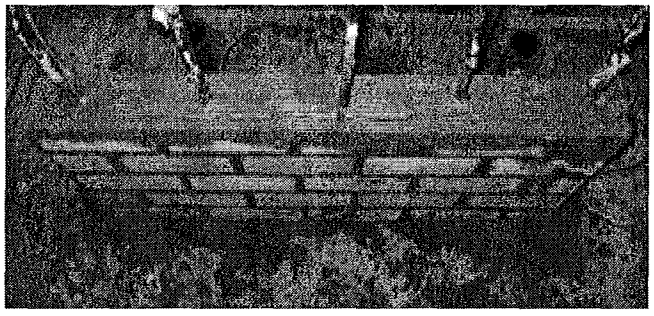

Figure 4-5: Shear Wall Specimen after First Day of Grouting

Figure 4-6: Grout Vibrator Head Attachment

4.4 Material Properties of Shear Wall Components

The material properties of the individual components that make up the reinforced concrete masonry shear walls used in this phase of the experimental program will be discussed in the following section.

4.4.1 Block Strength

The block properties used for the shear wall specimen construction have already been discussed in details in Section 2.3 of this thesis. A brief summary of

the compressive strength of the third-scale model blocks will be presented in this section. The average block strength recorded from 5 compressive strength tests 54.2 MPa, with a C.O.V. of 4.72%. As described in Section 2.3, the model block compressive strengths were much higher than the full-scale blocks used in the prototype shear wall specimens. The full-scale blocks tested by Shedid (2006) had an average compressive strength of 24.8 MPa with a C.O.V. of 3.9%.

4.4.2 Mortar Properties

The mortar used in the construction of the shear wall specimens was a Type S mortar made with Type 30, high early strength cement, lime and sieved masonry sand. The gradation of the sieved masonry sand used as the aggregate component of the mortar mix was shown in Figure 2-22. The mortar mix used was 1: 3.55: 0.2: 0.88 (cement: masonry sand: lime: water) by weight. The water content was adjusted slightly between batches to achieve a workable mortar with a flow between 125 and 130 mm. Owing to the small size of the third-scale mortar joints, much less mortar was required compared to that for a full-scale wall. The mortar was not kept for longer than 45 minutes to ensure that it did not dry out.

The average compressive strength of the mortar used was determined in accordance with ASTM standard C109-08 (2008) and CSA A179 (2009) through the testing of mortar cubes. The average compressive strength of the mortar used in the third-scale shear walls was 29.2 MPa (C.O.V. = 10%) with an average flow of 128 mm. Mortar cube specimens were tested 60 days after they were originally cast. The average compressive strength of the mortar used by Shedid (2006) in the full-scale prototype was 27.7 MPa (C.O.V. = 11.6%).

4.4.3 Grout Properties

The fine grout used in the construction of the third-scale model shear walls was composed of Type 10 cement, lime and sieved concrete sand. The gradation of the sieved concrete sand used as the aggregate component of the grout mix is

shown in Figure 2-25. The grout mix used was 1: 3.9: 0.04: 0.85 (cement: sand: lime: water) by weight. The water content varied slightly in between mixes in order to achieve a grout slump of approximately 250 mm. The high slump was necessary to ensure that the grout would completely fill the cells of the shear walls.

The compressive strength of the grout was determined by testing non-absorptive cylinders. The dimensions of the cylinders were 100 mm in diameter by 200 mm in height. The average compressive strength recorded was 18.2 MPa (C.O.V. = 14.0%) with an average slump of 255 mm. The cylinders were tested 60 days after they were cast. The grout used by Shedid (2006) was a commercial fine grout produced by a local ready-mix company. The average grout strength used by Shedid (2006) in the full-scale shear walls was 37.8 MPa. This strength is much higher than the third-scale grout due to the presence of super-plasticizers in the ready-mix grout.

4.4.4 Steel Reinforcing Properties

The vertical reinforcing steel used in the third-scale model shear walls was D7 deformed wire with a cross-sectional area of 45 mm^2. The stress-strain relationship curve for the D7 deformed wire is shown in Figure 2-28. The tensile strength of the steel bar was determined in accordance with ASTM standard E111-04 (2004). The average yield strength recorded was 540 MPa (C.O.V. = 1.5%). The yield strength of the 25M vertical steel bars used by Shedid (2006) in the full-scale shear wall prototypes was 503 MPa (C.O.V. = 0.6%). The cross-sectional area of the 25M prototype bars used was 500 mm^2.

Using the scale factor of S_L = 1/3, the area (A) of the third-scale model bar should have been S_L^2 = 1/9 of the area of the 25M bar used in the full-scale wall (Harris et al, 2000). Using this scale factor, the cross-sectional area of the third-scale reinforcing bar should have been 55 mm^2. The reason that the D7 (A_s = 45 mm^2) bar was selected was to account for the increase in tensile strength typically

associated by deformed wire. The deformed wire manufacturer's specifications suggested an area reduction of 0.8 when converting rebar steel area to deformed wire. This factor was based on the assumed strength ratio of 400 to 500 MPa. The D7 wire had a higher yield strength than the 25M bar, but it was not the expected 25% increase that was assumed.

The horizontal reinforcing steel used in the third-scale model shear walls was W1.7 smooth wire. The W1.7 wire had a cross-sectional area of 11 mm^2. The stress-strain relationship curve for the W1.7, smooth wire, is shown in Figure 2-29. Using the scale factor $A = S_L^2 = (^1/_3)^2$, the W1.7 bar area corresponded exactly to the full-scale 10M (A_s = 100 mm^2) used by Shedid (2006) in the full-scale prototype shear walls. The 10M bars tested by Shedid (2006) had an average yield strength of 491 MPa (C.O.V. = 0.4%) while the W1.7 wires had an average yield strength of 680 MPa (C.O.V. = 1.2%). Although the W1.7 wire had a higher yield strength than anticipated, it was decided that the increase in shear strength would have a minimal impact the desired flexural failure of the third-scale model shear wall.

4.4.5 Compressive Strength of Masonry Assemblages

Three prisms were built on each day of construction. As mentioned early, the walls were grouted in three phases. All construction prisms were 4 courses high and built using stretcher units and half stretcher units. The three sets of prisms were grouted along with the walls in order to document the compressive strength and modulus of elasticity variation within the walls. In total there were nine construction prisms tested. All construction prisms were tested around the time approximately 6 months after they were built. This timeline corresponded to the testing of the wall specimens. Table 4-2 presents a summary of the assemblage and shear wall material property variation throughout the construction process. Day 1, Day 2, and Day 3 specimens correspond to the bottom six, middle six and top six courses of the shear wall specimens, respectively.

Table 4-2: Summary of Construction Prism Compression Test Results

Specimen	f'_m (MPa)	Average f'_m (MPa) [C.O.V. (%)]	E_m (MPa)	Strain at f'_m (ε_u)	Average ε_u [C.O.V. (%)]
Day 1	25.7	23.7 [7.2%]	15640	0.00209	0.00197 [8.9%]
Day 1	23.1		17313	0.00205	
Day 1	22.5		17884	0.00177	
Day 2	19.9	20.7 [5.4%]	14474	0.00195	0.0020 [5.7%]
Day 2	20.2		13609	0.00213	
Day 2	22.0		15258	0.00192	
Day 3	23.3	22.6 [21.3%]	18027	0.00194	0.00185 [21.0%]
Day 3	18.5		16505	0.00142	
Day 3	26.1		18168	0.00218	

4.4.6 Comparison of Shear Wall Component Materials

Table 4-3 presents a summary of the third-scale material properties of the individual constituent elements of the shear wall specimens and directly compares them to those used by Shedid (2006) in the full-scale prototype shear walls. In general, the third-scale model is comparable to the full-scale prototype, the main difference being the compressive strength of the model blocks and the resulting f'_m of the masonry assemblage. The impact of these small differences will be further explored in Chapter 5 when the third-scale model shear walls are compared to the full-scale results obtained by Shedid (2006).

Table 4-3: Comparison of Shear Wall Constituent Materials

	Block	Mortar	Grout	Assemblages			Steel		n =
	f_b (MPa)	f_m (MPa)	f_g (MPa)	f'_m (MPa)	ε_{ult} (mm/mm)	E_m (GPa)	f_y (MPa)	E_s (GPa)	E_s/E_m
Third-Scale	54.2	29.2	18.2	22.5	0.00194	16.3	540	200	12.3
Full-Scale*	24.8	27.7	37.8	14.2	0.00177	10.6	503	200	18.9

**full-scale results summarized from M.A.Sc. Thesis by Shedid (2006) (Type II construction prisms)*

A comparison of the average stress-strain relationships of both the full-scale construction prisms tested by Shedid (2006) and the third-scale model assemblages is presented in Figure 4-7. The results correspond with the data presented in Table 4-3. As expected, the masonry compressive strength (f'_m) and elastic modulus (E_m) of the third-scale assemblages were both higher than the full-scale assemblages due to the high compressive strength of the individual blocks. However, the strain at ultimate corresponded well between the reduced-scale and full-scale specimens. The grout strength, f_g, used in the full-scale prototype walls was higher than that used in the model walls as it was a commercial ready-mix grout with additives that increased strength. The stress-strain relationships of all each construction prism can be found in Appendix D.

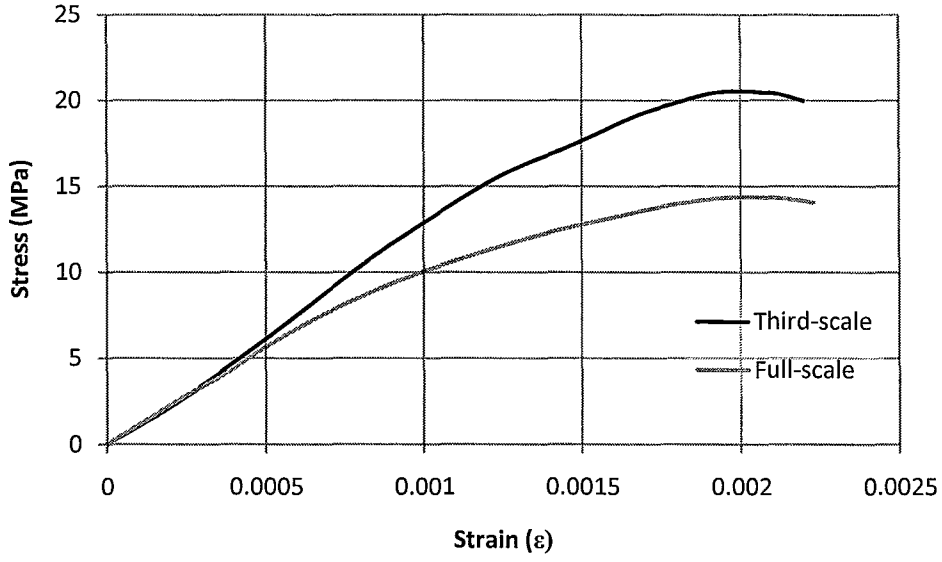

Figure 4-7: Stress-Strain Comparison of Full and Third-scale assemblages

4.5 Experimental Setup

The experimental shear wall test rig was designed to mimic an existing shear wall setup at McMaster University used previously by Shedid (2006) during

the full-scale prototype shear wall testing. This setup was designed in part by Wierzbicki (2010) and was used for both research programs.

The concrete wall bases were placed on a steel base made of two heavy 610 mm deep, wide flange steel beams welded together side by side. The steel base was attached to the base plates of four 410 mm wide flange columns using eight 19 mm thick stiffener plates (two stiffener plates at each corner). Finally, the steel base and columns were post-tensioned to the strong floor of the lab through the 25 mm column base plates using 51 mm diameter bolts. The usable base surface area for the setup was 2,000 mm x 600 mm. The plan view of the experimental setup is shown in Figure 4-8.

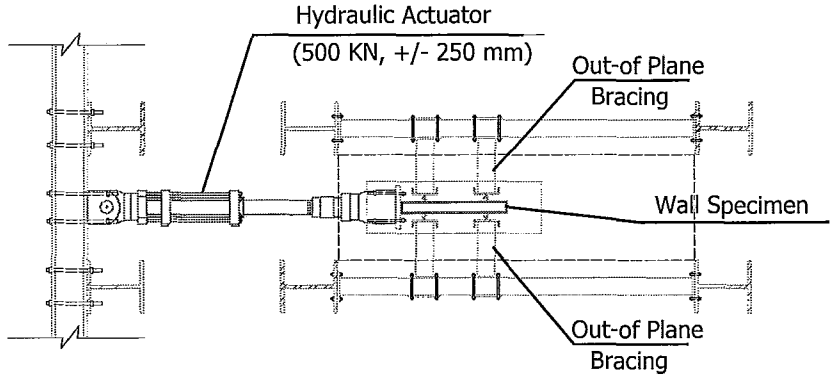

Figure 4-8: Plan View of Shear Wall Test Setup

As mentioned previously, the wall specimens were constructed on concrete base that had been poured with vertical voids to allow for the shear wall specimens to be post-tensioned into the experimental test rig. Six 19.5 mm threaded rods were used to post-tension the shear wall specimens to the 610 mm deep, heavy steel base beam. The rods were spaced at 340 mm on centre and were fastened to the steel base using 12.5 mm steel plates and 19.5 mm nuts. The

threaded rods were then post-tensioned using a torque wrench to a force of 40 kN. An elevation of the experimental shear wall test rig has been provided in Figure 4-9.

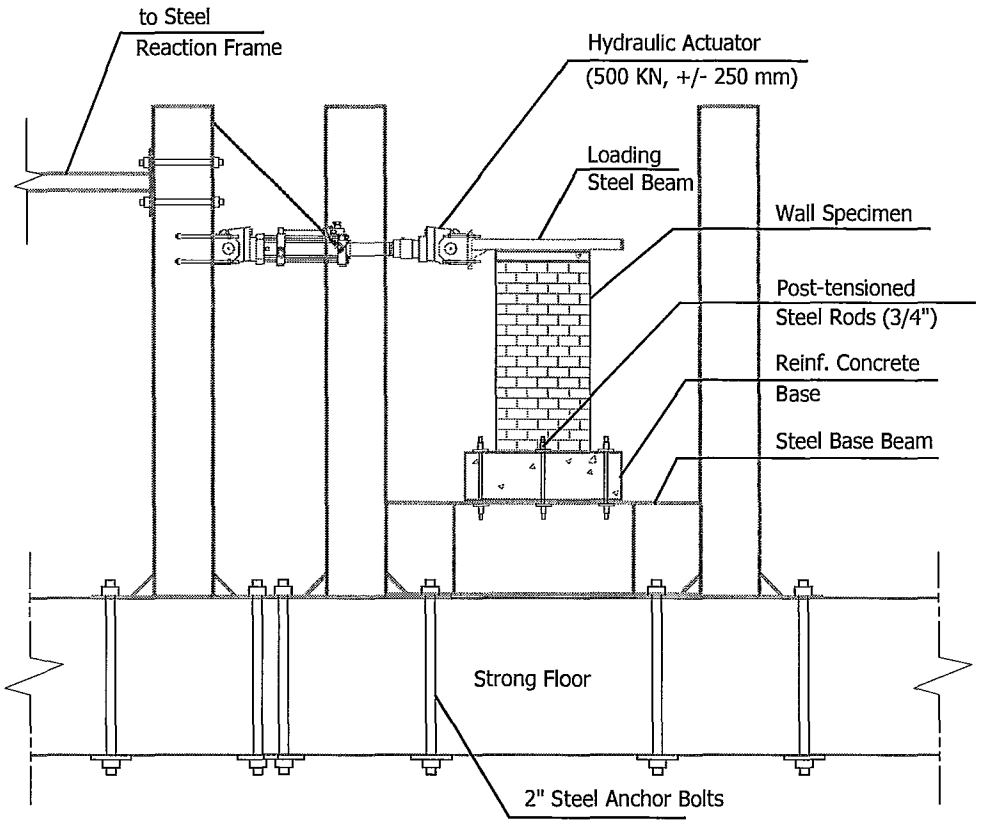

Figure 4-9: Elevation View of Shear Wall Setup

The lateral load was applied to the shear wall specimen at the top of the wall as shown in Figure 4-9. The load was applied with using a displacement-controlled MTS hydraulic actuator. The capacity of the actuator was 500 kN in both the push and pull directions and had a maximum stroke of 500 mm. The actuator was attached to a steel loading beam that was placed on top of the

concrete loading beam at the top of the wall. The steel loading beam consisted of two 100 mm x 100 mm x 6.4 mm angles and a 360 mm x 305 mm x 19.5 mm thick loading plate welded to the ends of the angles. The loading plate was pre-drilled with four 28.5 mm diameter holes to allow for the attachment of the actuator shown in Figure 4-10 (left side). The two angles were welded to the loading plate so that a 12.5 mm gap was left between the bottom legs to allow for the vertical bars to pass through the steel loading beam. The vertical steel bars were then welded to the steel loading beam using 50 mm x 50 mm x 6.4 mm square plates as shown in Figure 4-10 (right side). After the vertical reinforcing bars were welded to the loading beam the beam was attached to the MTS hydraulic actuator using four 19.5 mm diameter bolts (shown in Figure 4-11). The load from the actuator was transferred through the wall by the vertical reinforcing bars.

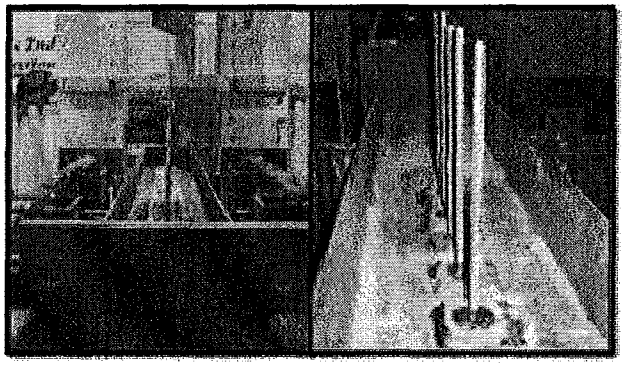

Figure 4-10: The Steel Loading Beam at Top of Shear Wall

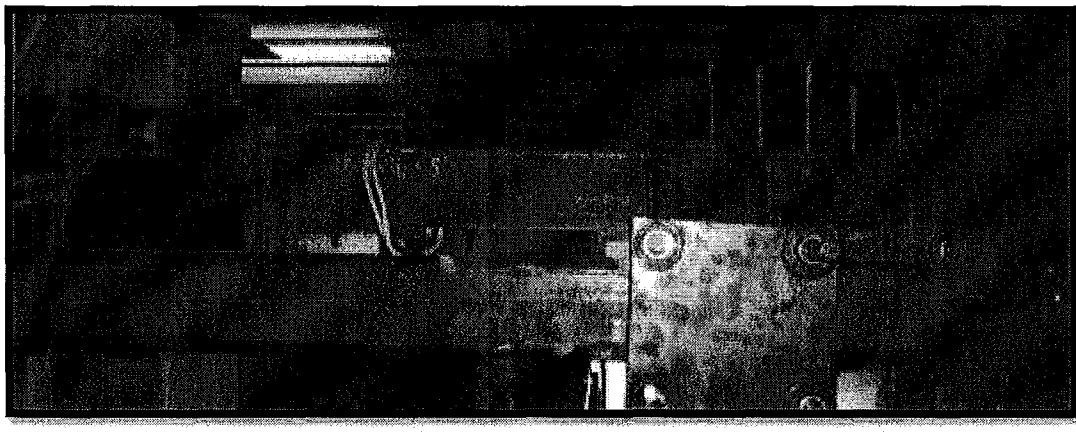

Figure 4-11: The MTS Actuator Attached to Steel Loading Beam

As the shear wall test specimens were loaded in-plane using the MTS hydraulic actuator they were restrained from movement in the out of plane direction using supports consisting of rollers welded to HSS 100 mm x 100 mm x 6.4 mm supports. The HSS support arms extended back to another of the same cross-sectional dimensions that spanned the distance of the main setup columns. In total, there were four out-of-plane braces acting as a guide to ensure that the shear wall remained in plane during the experimental loading. Details with respect to the movement and general behaviour of the shear wall specimens during testing are discussed in Chapter 5. The out-of-plane supports can be seen in the plan view of the test setup (Figure 4-8) and in Figure 4-12.

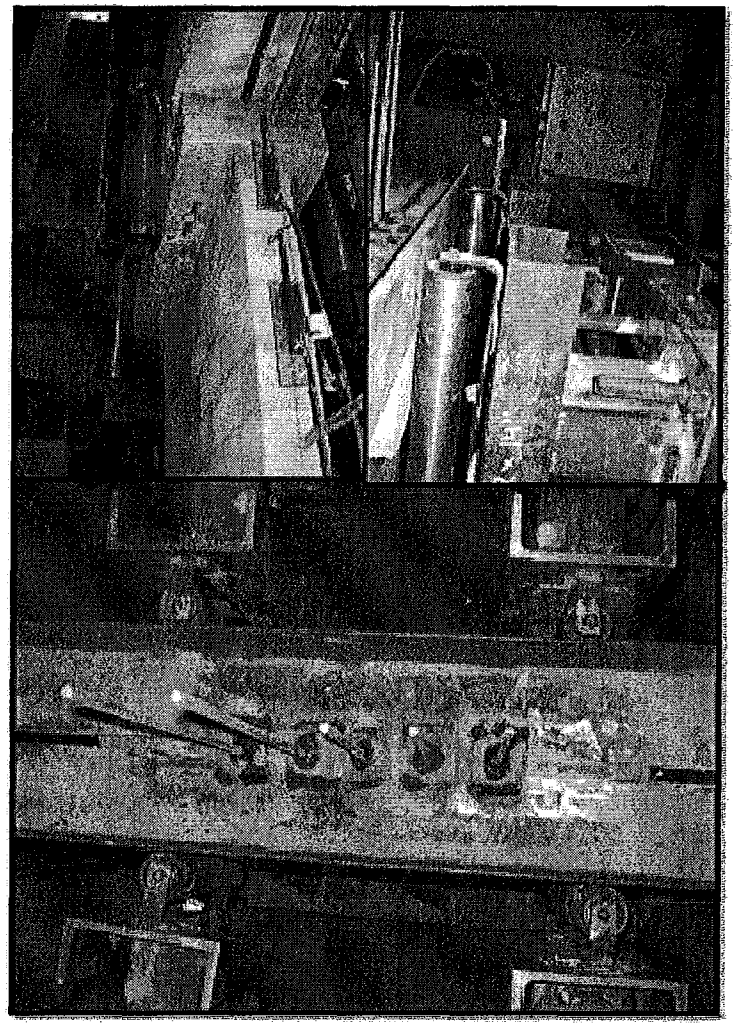

Figure 4-12: Shear Wall Out-of-Plane Bracing

4.6 Instrumentation and Measurements

The MTS actuator used to apply displacement to the top of the wall had a built in load cell to measure the applied force, which was recorded during the test procedure using a 60-channel data acquisition system that took readings every 2 seconds. The internal instrumentation of the shear walls through use of strain gauges and the external instrumentation using linear variable displacement transducers (LVDTs) are described in this section of the thesis. In total the

measurements from 12 strain gauges and 27 LVDTs were recorded using the aforementioned data acquisition system.

The strain measurements taken during testing were recorded at the two end vertical reinforcing bars on each side of the walls. The end vertical bars were instrumented with strain gauges to determine the extent of yielding within the wall. The extent of yielding was recorded using LVDTs LS2 to LS5 and RS2 to RS5 on the extreme tensile bars as shown in Figure 4-13. LS1 and RS1 were used to observe the extent of yielding into the concrete base. Strain gauges LS6 and RS6 were added to the second bar from the ends at the interface between the concrete base and the shear wall. These strain gauges would allow for the yield strain in the extreme tensile bar to be verified during testing to establish the wall's yield displacement.

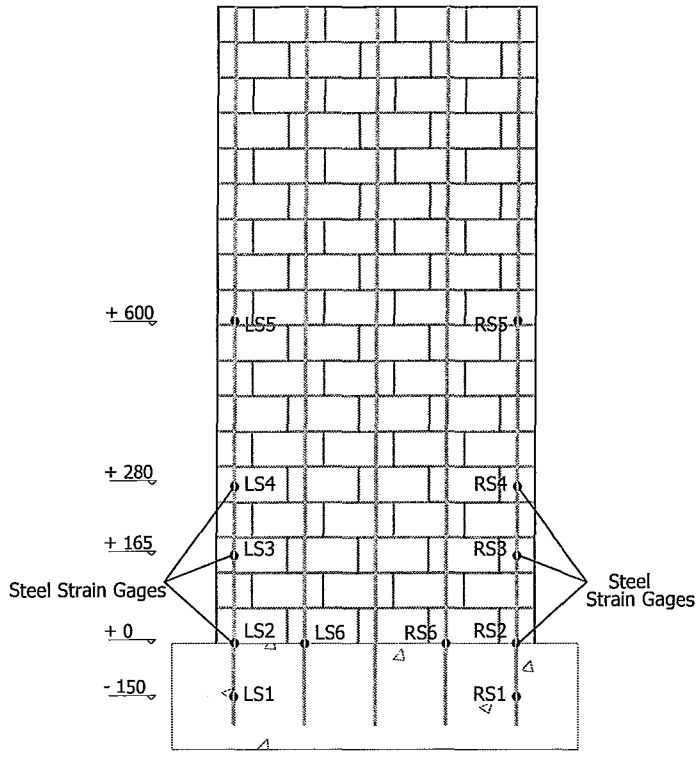

Figure 4-13: Strain Gauge Locations on Shear Wall

A total of 27 LVDTs were used to record external displacements throughout the testing procedure. LVDTs L1 to L12 were positioned vertically along each of the two ends of the shear wall specimens and used to calculate average curvatures during testing. The average curvature calculations are described in detail in the Appendix A. LVDTs L1, L2, L15, L16, L17, L18, L10, and L11 were used to evaluate the strain gradient in the wall specimen. Displacement transducers L13 and L14 were placed at the top of the wall on a diagonal in order to create a strain rosette that would later be used to distinguish between shear and flexural displacements. The flexural and shear contributions of the recorded displacements will be discussed in Chapter 5. LVDT L19 was used to record base slip between the shear wall and its concrete base, while LVDT L20

was used to measure the base slip between the concrete base and the steel base attached to the structural floor. The in-plane lateral displacements were measured using LVDTs L21 to L27 whereas LVDTs L1 to L19 were attached to 22 gauge steel strips and fixed to the wall using Loctite adhesive. L20 to L27 LVDTs were attached to an instrumentation support post. The support post was isolated from the shear wall to ensure recording any base slip during testing. The LVDT layout is shown in Figure 4-14. The placement of the LVDTs corresponded to the LVDT layout used by Shedid (2006) during his full-scale shear wall testing. A fully instrumented shear wall is shown in the setup just prior to testing in Figure 4-15.

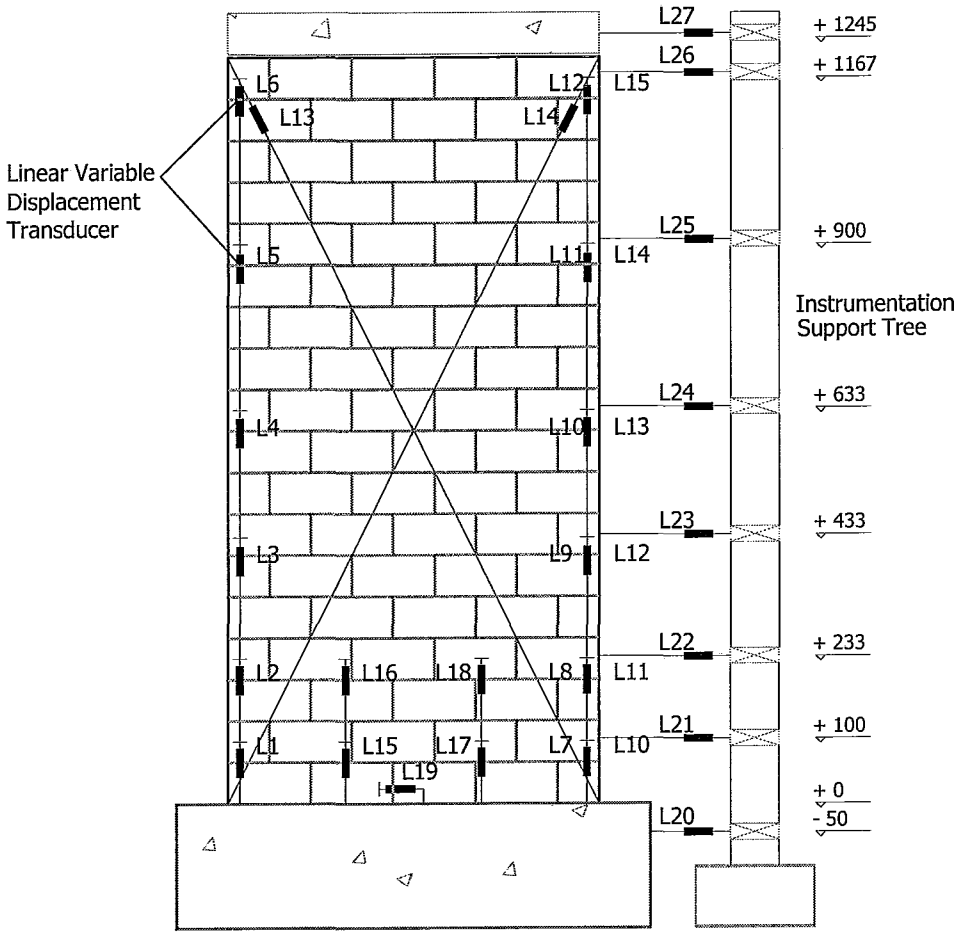

Figure 4-14: LVDT Locations on Shear Wall

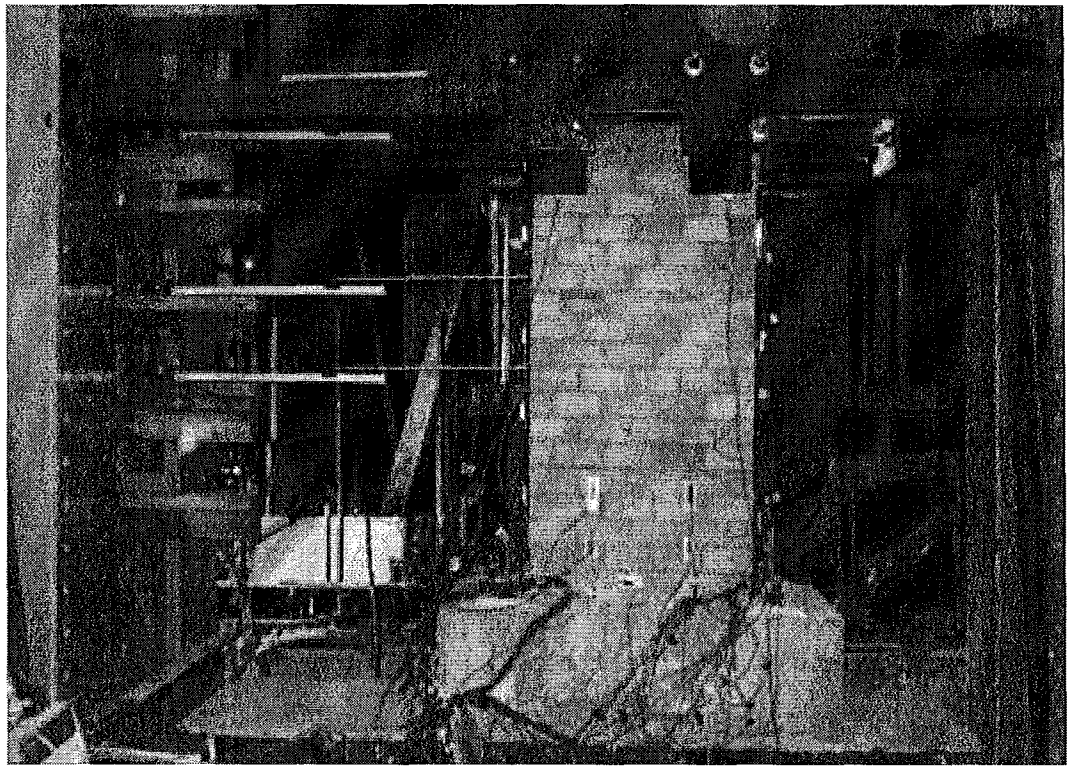

Figure 4-15: Shear Wall Specimen in Test Setup (prior to testing)

4.7 Testing Procedure

The original plan was to test the walls in displacement-controlled environment using a reversed cyclic technique similar to that of previous flexural shear wall experimentation completed at McMaster University by Shedid (2006) and Long (2006). However, during the preliminary wall testing phase it was noticed that the model vertical reinforcing steel (D7 wire) was less ductile under cyclic loading compared to the tensile test coupons. Although the stress-strain of the vertical D7 wire shown previously in Figure 2-28 seemed to achieve more than adequate ultimate strain (approximate 3.5 % elongation); the low cycle fatigue on the bars resulting from cyclic displacements caused the vertical bars to rupture in tension before the masonry could reach its full compressive strength

potential. This phenomenon was observed in a third-scale model shear wall tested by Wierzbicki (2010).

The relatively brittle steel used as vertical reinforcing did not impact the strength of the wall (as will be discussed in Chapter 5); however it did have an impact of the ductility. In order to relate the third-scale model results to the ductile results obtained by Shedid (2006) with his full-scale shear walls it was decided to test the model walls monotonically (push-over). A previous study carried out by Jamison (1997) validated the ability of a monotonic test to represent the backbone curve of cyclic loading. Jamison found that the initial cyclic values were within 94% to 97% of the monotonic strength capacities while the initial cyclic deflections were between 77% and 81% on the monotonic displacements (Jamison, 1997). These results illustrate the fact that the load displacement curve resulting from a shear wall tested in-plane through monotonic loading can easily be related to results obtained through cyclic loading. The "backbone curve" is defined as the load displacement envelope that encompasses load-displacement hysteresis loops resulting from cyclic loading (Chopra, 2001). The results obtained by Jamison (1997) will be used in Chapter 5 to relate the third-scale model monotonic testing to full-scale walls tested cyclically by Shedid (2006).

In order to ensure that all measurements were being properly recorded, each wall was first subjected to a single cycle at approximately 25% of the theoretical yield force. After this preliminary cycle the hydraulic actuator was returned to its neutral position where no load was being applied to the wall. The wall was then pushed monotonically at a rate of approximately 1 mm every 60 seconds until the extreme tensile bar reached its predetermined yield point. The yielding of the tensile bars was observed through the internal strain gauge instrumentation. The pause in loading during as the wall reached its yield point was to allow for detailed examination of the test specimen. This recorded lateral

displacement at the top of the wall as the extreme tensile bar yielded was then used as a displacement increment that would define subsequent examination pauses. At each yield displacement increment the wall was examined for cracks and general behaviour was observed. The crack patterns were highlighted and photographed at each increment of yield displacement in order to document the crack propagation throughout the test. Details with respect to the individual tests will be described in Chapter 5.

4.8 Conclusions

The two third-scale model shear wall that were tested during this experimental program were described in this chapter. The dimensions, steel reinforcing ratios and individual material properties were all modeled after two full-scale shear walls that were tested previously at McMaster University by Shedid (2006) in an attempt to directly compare their behaviours. The individual third-scale properties were directly compared to the material properties used within the full-scale prototype walls. In general, the third-scale material properties related well to the full-scale prototype. The main variation between model and prototype was the block strength. The average stress-strain relationship of the construction assemblages was compared, again illustrating the impact of the higher third-scale block strength. As expected, the increased block strength resulted in an increased elastic stiffness when compared to the full-scale stress-strain relationship curve.

The shear wall test setup procedure was also examined within this chapter. Just as the with the material properties of the wall, the design of the test setup was such that the testing procedure could be carried out in a similar manner to the full-scale testing performed by Shedid (2006). The details with respect to the instrumentation of the shear wall specimens and the measurement scheme used during the test were consistent with those used by Shedid (2006) in order to directly compare results.

The monotonic test procedure, as well as the rationale behind employing it was outlined in this chapter. In general the monotonic loading curve was deemed to be an adequate representation of the backbone curve resulting from cyclic. A more detailed analysis with respect to the model shear walls test results is provided in Chapter 5 of this thesis.

5 EXPERIMENTAL SHEAR WALL TEST RESULTS AND ANALYSIS

5.1 Introduction

The third-scale model experimental shear wall test results are described in this chapter and compared to the full-scale shear wall results obtained by Shedid (2006). This chapter describes the results obtained through the experimental monotonic testing of the two shear wall specimens. The focus is on the load-displacement relationships, extent of plastic hinging, curvature and stiffness degradation. The third-scale results are then compared to the full-scale shear walls tested by Shedid (2006). The comparison between third-scale and full-scale specimens will include strength, displacement, stiffness and ductility assessments in order to examine the ability of the third-scale materials to model full-scale materials when used in a shear wall.

5.2 Experimental Results – Wall 1

5.2.1 Wall 1 Details

Wall 1 was reinforced with five D7, deformed wire, used as vertical bars (A_s = 45 mm^2) with a spacing between the bars of 133.3 mm (every other cell) and nine W1.7, smooth wire, used as horizontal reinforcement (A_s = 11 mm^2) spaced at 266.7 mm increments. The wall was loaded laterally, in-plane, at the top of the wall. In the beginning, the wall was pushed and pulled at a force equivalent to 25% of the theoretical yield to ensure that all gauges were properly recording data. The wall was then pushed monotonically until the extreme tensile bar ruptured. Following the rupture of the extreme tensile bar, the wall was pulled back, reversing the loading cycle, until the extreme tensile bar on the opposite end of the wall (previously in compression) ruptured. As mentioned earlier, it was the original intension to test the wall under displacement-controlled reversed cyclic

loading (as in the full-scale prototype testing); however, due to the material behaviour of the vertical reinforcing steel, a monotonic test was thought to provide the most usable data.

5.2.2 General Observations

As mentioned previously, the wall test procedure began with a calibration load-displacement loop where the wall was cycled at 25% of the theoretical yield force. After the calibration cycle, the wall was monotonically loaded at the top until the extreme tensile vertical bar ruptured. At that point the loading was reversed and the wall was pulled back until extreme tensile bar rupture on the other side of the wall. The load applied to the shear wall is plotted against the wall displacement and in provided in Figure 5-1. The general observations recorded over the course of this experiment are discussed in this section of the thesis.

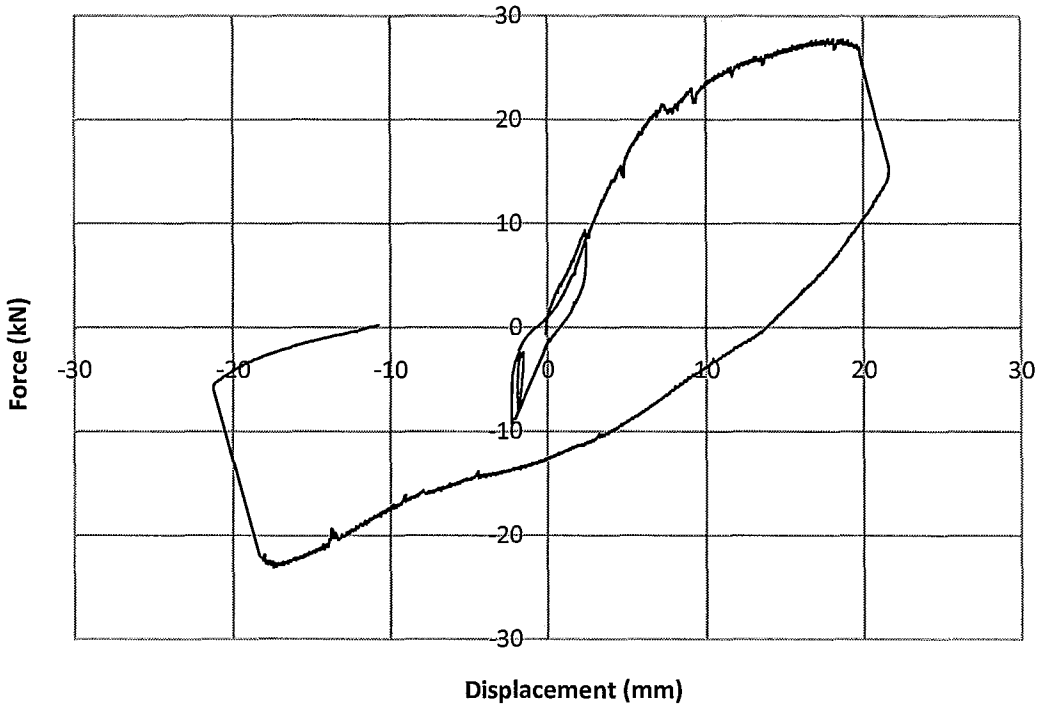

Figure 5-1: Wall 1 - Load-Displacement Response Curve

Bed joint cracking was noticed during the calibration cycle at 25% of the theoretical yield force. The horizontal cracking occurred at the 3rd and 6th courses from the bottom. The bed joint cracking continued at 50% of the theoretical yield force which occurred at 2.25 mm displacement at the top of the wall. The yielding of the vertical tensile steel was determined using the internal strain gauge located at the interface between the concrete base and the bottom course of the wall. The lateral displacement recorded at the wall top as the extreme tensile bar yielded was 4.5 mm; this displacement was then used as an incremental displacement point at which loading was paused during testing so that measurements could be taken and cracks photographed. The extent of bed joint cracking at the yield displacement, Δ_y, is shown in Figure 5-2. Bed joint cracking at yield occurred at the 3rd, 6th, 7th, 9th, and 11th courses (see Figure 5-2).

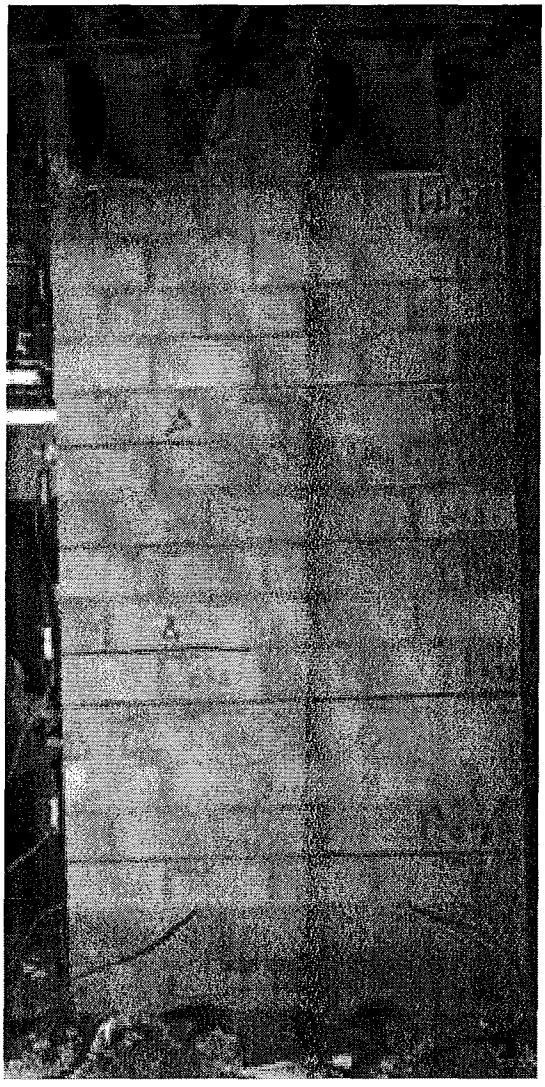

Figure 5-2: Wall 1 - Bed Joint Cracking at Δ_y

As the wall top displacement reached 9.0 mm, $2\Delta_y$, diagonal tension cracks began to appear through the face shells and head joints of blocks in the lower half of the wall. The stepped crack pattern that appears connecting the 9th course to the bottom course is shown in Figure 5-3.

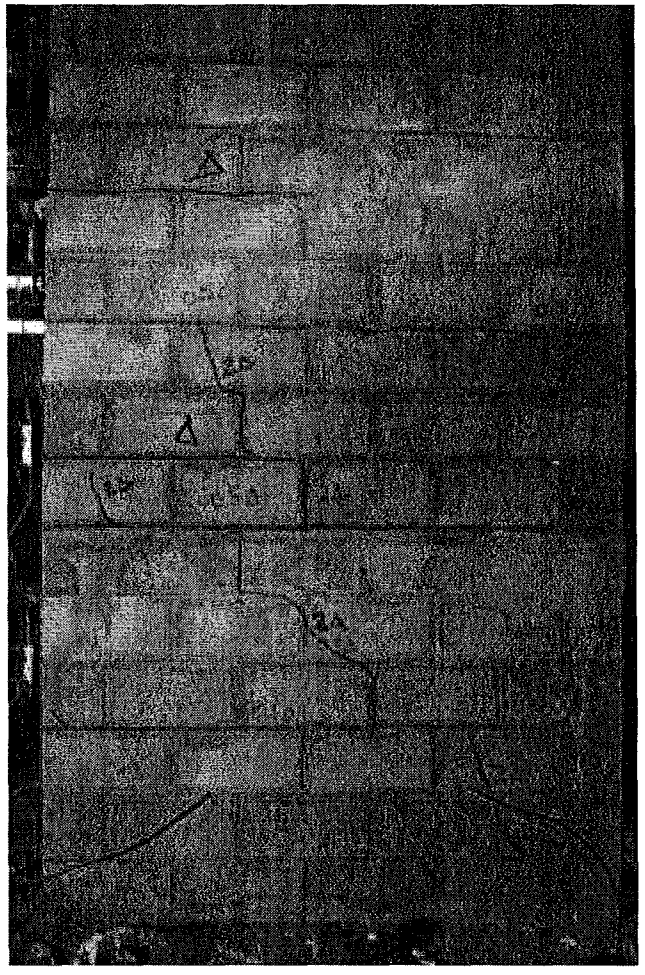

Figure 5-3: Wall 1 - Diagonal Tension Cracking at $2\Delta_y$ yield

As the lateral load reached 13.5 mm ($3\Delta_y$), the diagonal cracking continued to propagate towards the compression toe of the shear wall. The bottom bed joint crack at the interface between the wall and the concrete base began to extent lifting off the concrete base on the tension side of the wall. At 18 mm ($4\Delta_y$) the diagonal cracking had propagating from the 16th course down to the compression toe. There were no new horizontal cracks noticed at this time; however the cracks that existed continued to increase in width as the loading of the wall continued. The extent of the cracking can be seen in Figure 5-4.

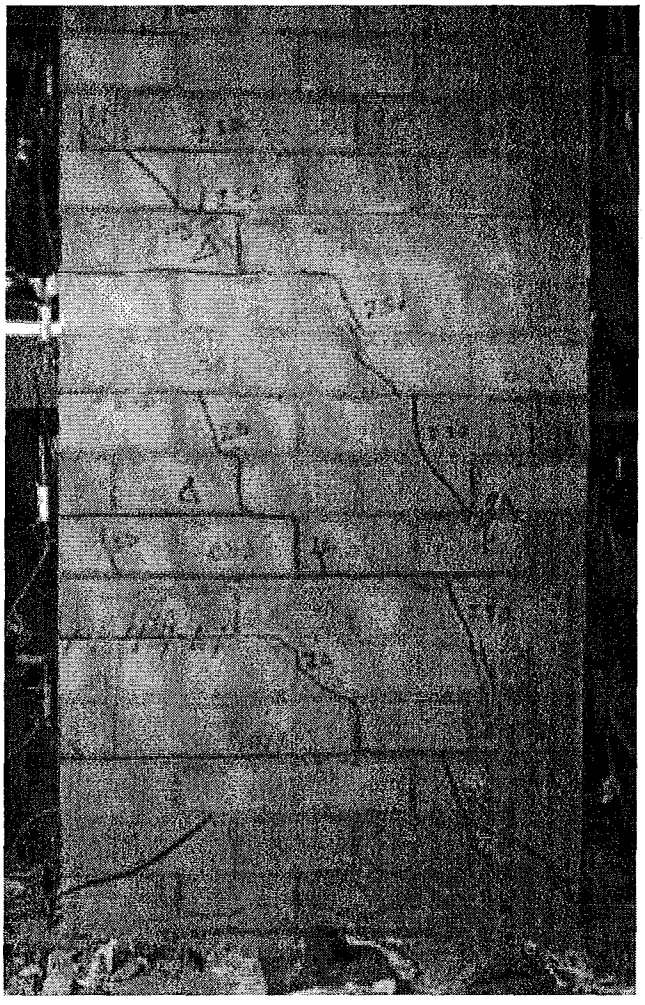

Figure 5-4: Wall 1 – Extent of Diagonal Tension Cracking at $4\Delta_y$

As the lateral displacement at the top of the Wall 1 reached 21.5 mm (approximately $4.7\Delta_y$) the extreme tensile bar ruptured. The rupture of the vertical reinforcing marked the end of the push cycle. The extent of the cracking in the compression toe of the wall can be seen in Figure 5-5. There was no face shell spalling or buckling of the vertical reinforcing bars in the compression toe as was noticed during full-scale prototype testing by Shedid (2006).

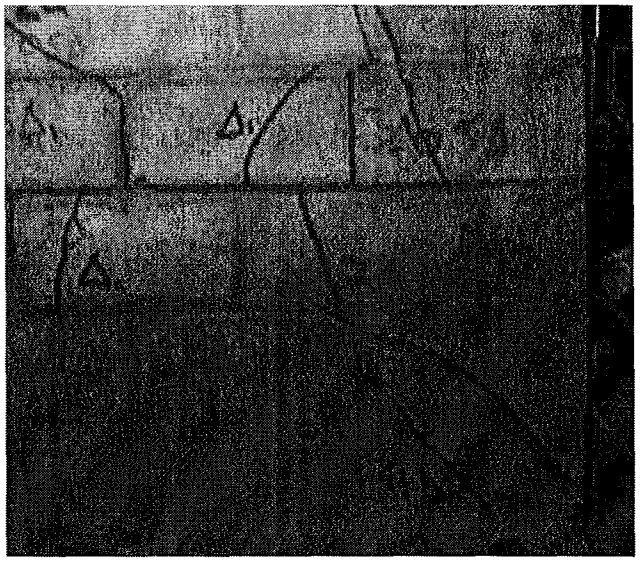

Figure 5-5: Wall 1 – Close up of Compression Toe at End of Test

At the end of the push cycle the end of the wall that was in tension had lifted-off of the concrete base approximately 6 mm. The extent of the uplift can be observed in Figure 5-6.

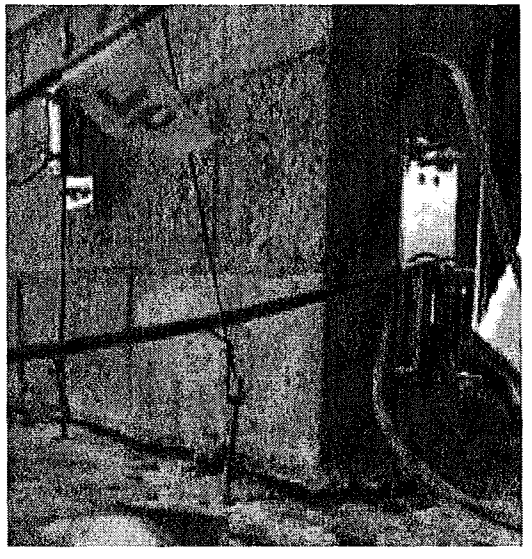

Figure 5-6: Wall 1 – Close up of Uplift at Tensile End of Wall

After the wall specimen had reached failure in the push direction, the loading cycle was reversed so that the other side of the wall could be tested. It was assumed that the effect of the compression steel (that had ruptured in tension) on the compression toe of the untested side of the wall would be negligible. The wall was loaded incrementally in pull using multiples of yield displacement similar to the push loading. The pull loading continued until the extreme tensile bar on the other side of the wall ruptured in tension. At the end of the testing procedure one tensile reinforcing bar had ruptured on each side of the wall.

The crack pattern during the pull loading direction seemed to mirror that previously recorded during the push loading direction. The only difference was that the line of symmetry was shifted from the centre of the wall unlike what was originally expected. This phenomenon was attributed to the damage caused during the wall push loading. The shifted line of symmetry along with the final crack propagation can be seen in Figure 5-7.

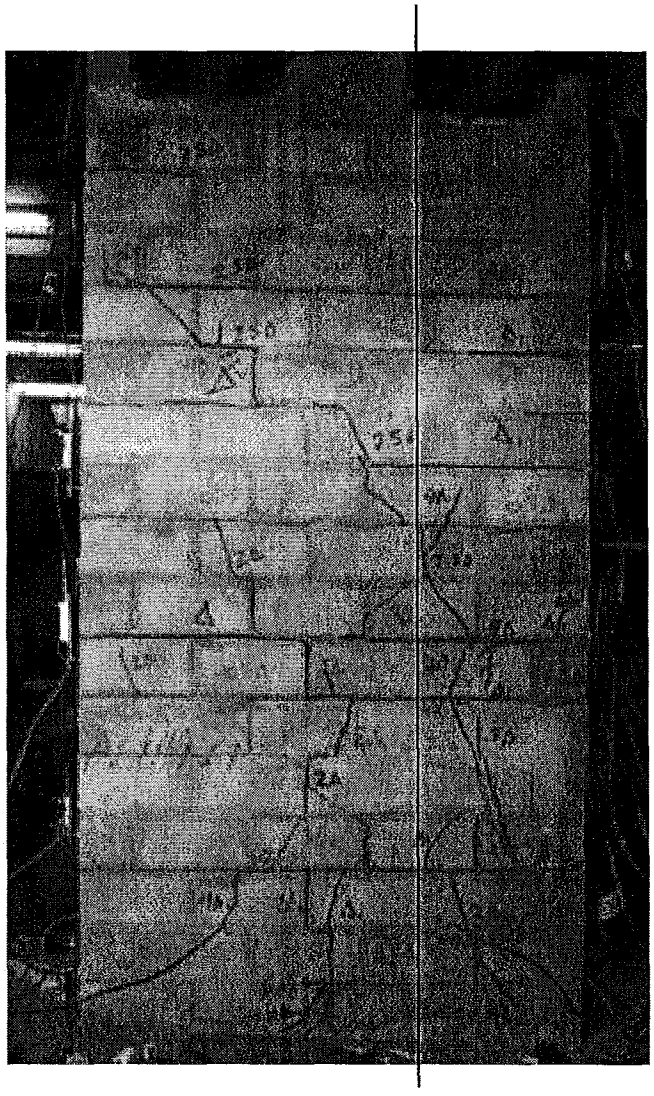

Figure 5-7: Wall 1 – Extent of Cracking (after push and pull displacements)

5.2.3 Load-Displacement Response

The load displacement response of Wall 1 is shown in Figure 5-1. The wall was loaded monotonically in the push direction until it reached failure after which it was pulled back in the opposite direction. As a result of this monotonic loading technique, the load-displacement curve obtained during the pull phase was not symmetrical with the push phase. However, the load displacement curve obtained during the initial push phase of loading seemed to represent the backbone curve of the full-scale walls tested by Shedid (2006). A more detailed

comparison of third-scale and full-scale load displacement relationships will be discussed later in the chapter. The backbone curve is shown in Figure 5-8.

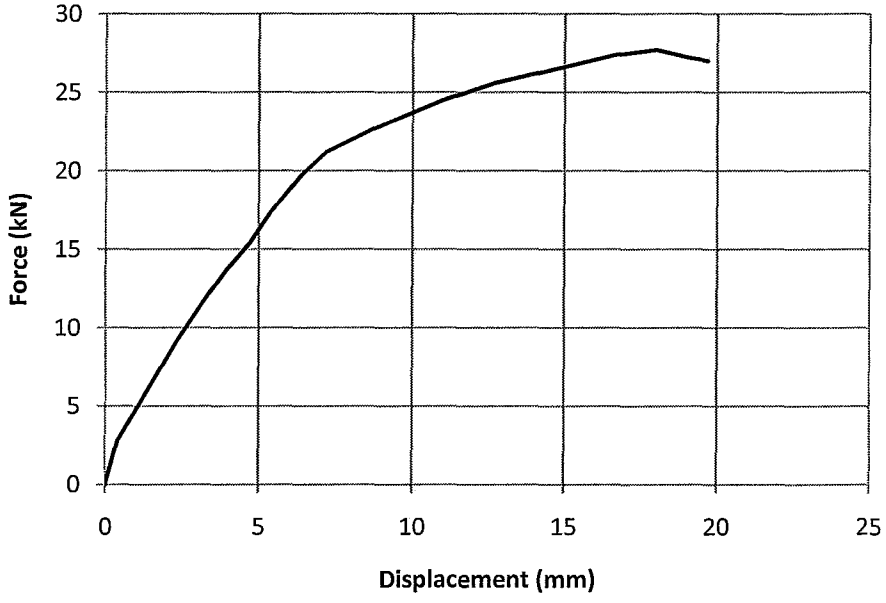

Figure 5-8: Wall 1 – Load-Displacement (Backbone Curve)

The wall response was almost linear up to the yielding of the extreme tensile bar (Δ_y = 4.5 mm). The corresponding lateral force, F_y, applied to the top of the wall was 13.3 kN. As expected, after the yielding of the extreme tensile bar, the stiffness of the wall decreased as the in-plane deformation increased. The wall reached its ultimate load, F_u, of 27.7 kN at 18.3 mm displacement. The test ended as the extreme tensile bar ruptured. The bar rupture occurred at 20.5 mm lateral wall displacement. The corresponding lateral force acting on the wall at this point was 26.2 kN, approximately 94.6% of the ultimate strength.

5.2.4 Experimental Results Compared to Predictions

A comparison between measured and predicted behaviour of Wall 1 is summarized in Table 5-1. Displacements and corresponding forces at both yield and ultimate displacements were calculated using basic flexural theory. The

equations used to determine predicted values are discussed in detail in Appendix C. The material properties used for the predictions were input based on the testing of the construction assemblages discussed in Chapter 4. Ultimate displacement values, Δ_u, were determined using the assumption that the walls would behave as shear walls with "limited ductility". The Canadian Standards CSA S304.1 (2004) assumes that limited ductility shear walls have a plastic hinge length equal to half of the length of the wall. The displacement ductility, μ_Δ, is defined as the ratio of displacement at the ultimate loading condition to the displacement measured at yield. This measurement of ductility is intended to provide an indication of the inelastic deformation exhibited shear wall. Table 5-1 compares theoretically predicted values with experimentally measured values from the monotonic push-over test.

Table 5-1: Wall 1 – Predicted and Experimental Comparison

Value	Predicted (ε_u = 0.0025)		Experimentally Measured
	excluding compression steel	Including compression steel	Push-over loading condition (monotonic)
Δ_y (mm)	3.0	2.9	4.5
F_y (kN)	19.5	18.5	13.3
Δ_u (mm)	9.5	10.3	18.7
F_u (kN)	25.9	26.8	27.7
$\mu_\Delta = \Delta_u / \Delta_y$	3.22	3.53	4.16
	Predicted (ε_u = 0.003)		
Δ_y (mm)	3.0	2.9	
F_y (kN)	19.5	18.5	
Δ_u (mm)	10.8	12.3	
F_u (kN)	26.2	27.0	
$\mu_\Delta = \Delta_u / \Delta_y$	3.67	4.21	

The CSA S304.1 does not permit the inclusion of compression steel when calculating the flexural capacity of a shear wall however it has been included in Table 5-1 for comparison purposes. Previous shear wall testing programs completed by Shedid (2006) and Long (2006) suggest that the inclusion of compression steel in theoretical predictions tend to yield values closer to actual experimental results than if the contribution of compression steel is ignored. As shown in Table 5-1, the inclusion of compression steel increased the expected ultimate strength (F_u) as well as the expected displacement ductility (μ_Δ).

The values listed under the experimentally measured column of Table 5-1, correspond to the plotted load-displacement curve, Figure 5-8. The measured initial yield displacement (Δ_y) was found to be approximately 50% greater than the theoretical displacement determined using beam theory. The force applied to the wall at the point of yield displacement (F_y) was lower than expected, 13.3 kN measured compared to 19.5 kN predicted. The ultimate capacity, F_u, recorded at 27.7 kN of the wall was predicted with reasonable accuracy to within 3.3% (including compression steel) at 26.8 kN and 6.9% (neglected compression steel) at 25.9 kN. The displacement recorded as the wall specimen reached its ultimate load, Δ_u, was 18.7 mm. This value was much higher than the expected 9.5 mm. With the inclusion of compression steel in the prediction and the assumption that the compressive strain in the masonry could reach 0.003 the prediction was 12.3 mm at ultimate.

5.2.5 Extent of Yielding Within Reinforcement

As previously discussed in Chapter 4, the outer most vertical reinforcing bars were instrumented with strain gauges in an attempt to measure the extent of yielding and plasticity within the shear wall. The yield strain of the vertical D7 reinforcing bars was experimentally determined to be 0.0027. During the test it was noticed that the strain gauge located at the interface between the concrete base and the shear wall was damaged. The yield point was determined using a

combination of theoretical yield force as well at experimental yield of the 2nd bar from the end. The extent of yielding of the outermost vertical reinforcing bars is summarized in Table 5-2.

Table 5-2: Wall 1 – Extent of Yielding of Vertical Reinforcement

Strain Gauge Location (height from base beam, mm)	Initial Yield Condition (ε_y = 0.0027)			Ultimate Load (27.7 kN)	
	Load (kN)	Displacement (mm)	Drift (%)	Strain (ε_s)	Factor X ε_y
Interface (0)*	---	---	---	---	---
165	19.24	6.77	0.56	0.00939	3.48
280	21.07	7.72	0.64	0.005744	2.13

**Strain Gauge at Interface was damaged and as a result did not accurately record any strain measurements*

As mentioned previously, the yielding of the outermost tensile bar occurred at the interface between the concrete base beam and the wall at a lateral displacement (top of wall) of 4.5 mm and an applied force of 13.3 kN. Yielding extended up the vertical bar to 165 mm from the interface at an applied load of 19.24 kN and to 280 mm from the interface at 21.07 kN.

5.2.6 Lateral Deformations of Wall 1

The in-plane lateral displacements of the shear wall specimen were measured at six locations along the height of the wall. The displacement values with respect to the height of the wall specimen are provided in Figure 5-9. For the most part, the displacement appeared to be linear. In addition, most of the flexural deformation occurred in the lower 400 mm of the wall which is consistent with the yielding of the extreme tensile bars, as the yielding extended past 280 mm from the interface between the concrete base beam and the bottom of the wall as the specimen reached the ultimate load of 27.7 kN.

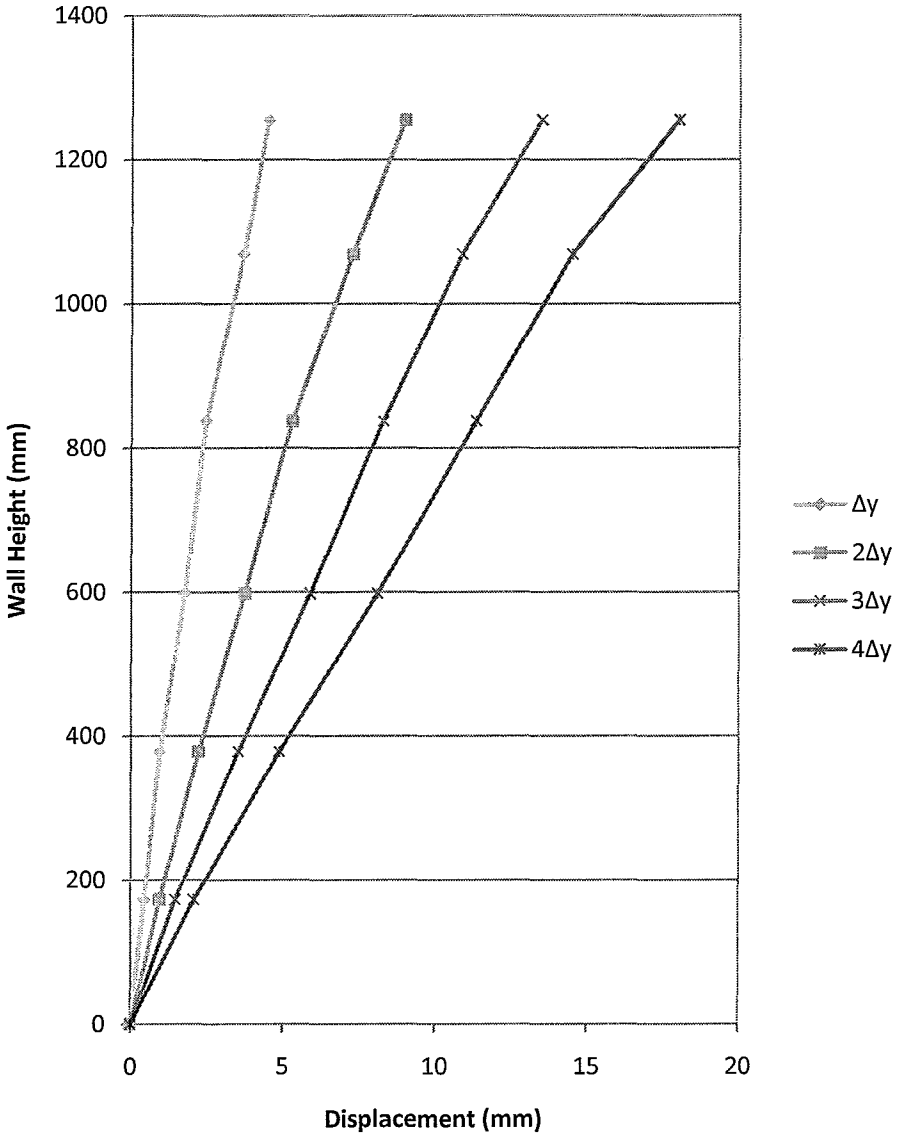

Figure 5-9: Wall 1 Lateral Displacement With Respect to Height

5.2.7 Wall Curvature

The average curvatures were measured over the height of the wall using compressive and tensile strains in six gauge lengths identified in Chapter 4. A detailed explanation with respect to the calculation of average curvatures can be

found in the Appendix A of this thesis. The average curvature along the height of wall 1 can be found in Figure 5-10.

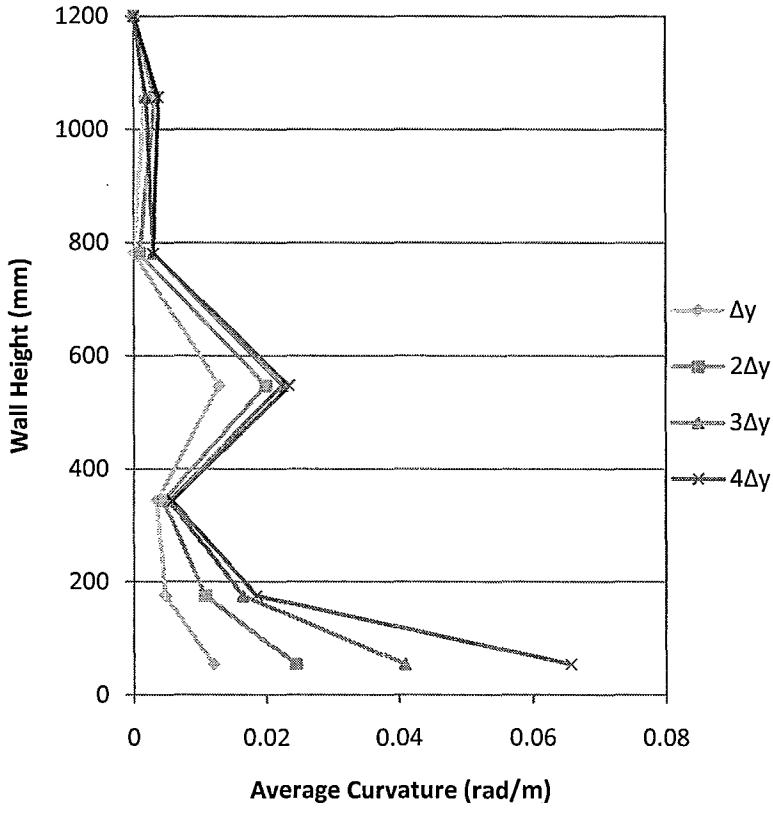

Figure 5-10: Wall 1 – Curvature Profile

The measured average curvature at yield, φ_y, was 0.01198 rad/m at the base of the wall, which was approximately double the predicted average curvature of 0.0061 rad/m. A detailed description of the theoretical curvature predictions can be found in the Appendix C. Average curvature measured over the bottom segment of the wall at ultimate loading, φ_p, was equal to 0.0657 rad/m which was approximately three times the curvature measured at initial yield and again approximately double that of the predicted average curvatures using the method described in the Appendix C. The measured curvatures within the lower segment

of the wall were higher than the predicted curvatures. This is consistent with the trend observed by Sasani and Kiureghian (2001) and by Shedid (2006). Sasani and Kiureghian (2001) suggested that this discrepancy between measured and predicted curvatures could be attributed to the conservative calculation of compressive strains. They suggest that the measured compressive strains are typically higher than predicted. This fact is further explored in the next section when looking at the measured strain values.

The wall segment located at the bottom third of the wall does not follow the expected curvature trend as the average curvature values measured at this segment were lower in comparison to segment above. One possible explanation for this behaviour is the lack of cracking between the gauges measuring average strain.

Overall the average curvature profile was consistent with the shape expected through comparison with the full-scale shear walls tested by Shedid (2006). The average curvature plotted against the height of the full-scale wall tested by Shedid (2006) is shown in Figure 5-11 for comparison purposes. The average curvature measured at the bottom wall segment for the third-scale wall was expected to be one third of the full-scale wall measured by Shedid (2006). This ratio appeared to be maintained throughout testing.

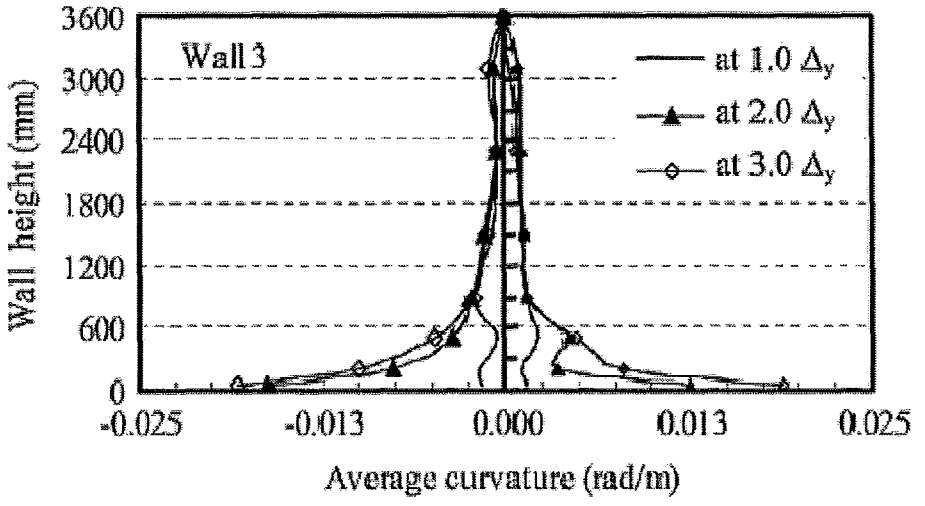

Figure 5-11: Average Curvature for Full-scale Wall Prototype (Shedid, 2006)

5.2.8 Strain Profile

The strain profile was recording using four LVDT's, as described in Chapter 4, along the length of the wall specimen at two gauge heights. The first gauge height measured strain from the base beam to approximately 105 mm above the base, see Figure 5-12. The second gauge height measured strains from 105 mm to 245 mm above the base, see Figure 5-13. The sign convention of the strain profile figures shows compressive strains as positive values.

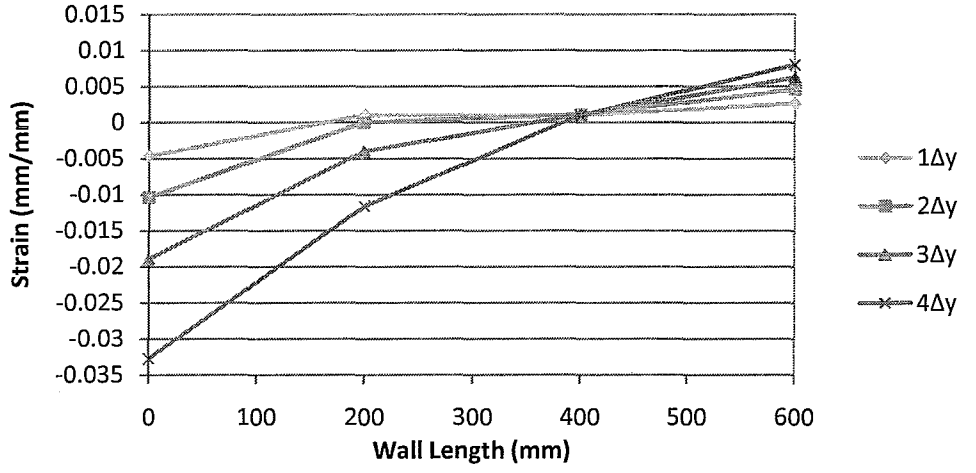

Figure 5-12: Average Strain along Length of Wall 1 (0 – 105 mm above base)

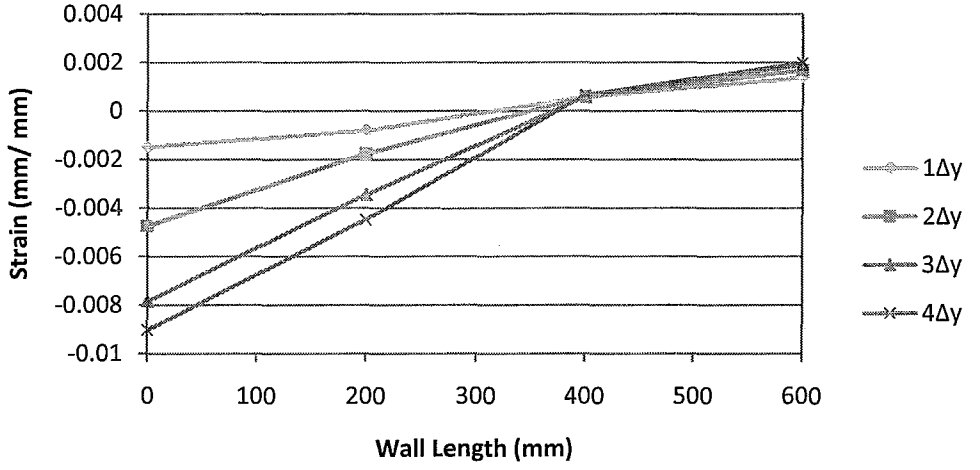

Figure 5-13: Average Strain along Length of Wall 1 (105 – 245 mm above base)

The lengths of the compression zone remained consistent between gauge lengths, showing the compression zone at just over 200 mm in length. This number was slightly higher than expected; however it should be noted that the tolerances of the strain gauges used to measure strains at the two gauge locations on the inside face of the walls limited the accuracy of this measurement. In

general, the strain profile was almost linear at yield displacement where the compression strain was $2.6x10^{-3}$. The maximum compressive strain recorded was $8.0x10^{-3}$ and occurred at the $4\Delta_y$ displacement. One possible explanation for such a high measured compressive strain was the confinement of the bottom block course built on the concrete base. This higher than predicted strain value is consistent with the higher curvature values described in the previous section. The maximum compressive strains were well over the CSA S304.1 limit of $3x10^{-3}$.

5.2.9 Stiffness Degradation

In an effort to compare stiffnesses of the third-scale shear walls to the full-scale specimens tested by Shedid (2006), a theoretical stiffness was approximated to provide some relevance to the measured stiffness plotted in Figure 5-14. A detailed description of the theoretical stiffness calculation can be found in the Appendix B. The predicted stiffness values obtained prior to testing are shown in Table 5-3. The stiffness values found in Table 5-3 were calculated using the individual material properties of the shear wall.

Table 5-3: Wall 1 – Summary of Theoretical Wall Stiffness Predictions

Value	Full-Scale* Prediction	Third-Scale Prediction	Third-Scale (1/3 of Full-scale)
Gross Stiffness, K_g (kN/mm)	70.41	33.9	23.5
Cracked Stiffness, K_{cr} (kN/mm)	17.48	4.56	5.83

**full-scale data shown is from M.A.Sc. Thesis by Shedid (2006)*

A complete comparison of the third-scale and full-scale specimens tested by Shedid (2006) can be found in Section 5.3. The following figure describes the stiffness deterioration of the third-scale shear wall specimen during the testing procedure. The measured initial stiffness, K_i, was 26.3 kN/mm, which deteriorated to 3.4 kN/mm at yield and finally to 1.5 kN/mm at ultimate load. The

stiffness degradation shown in Figure 5-14 was consistent with the expected deterioration.

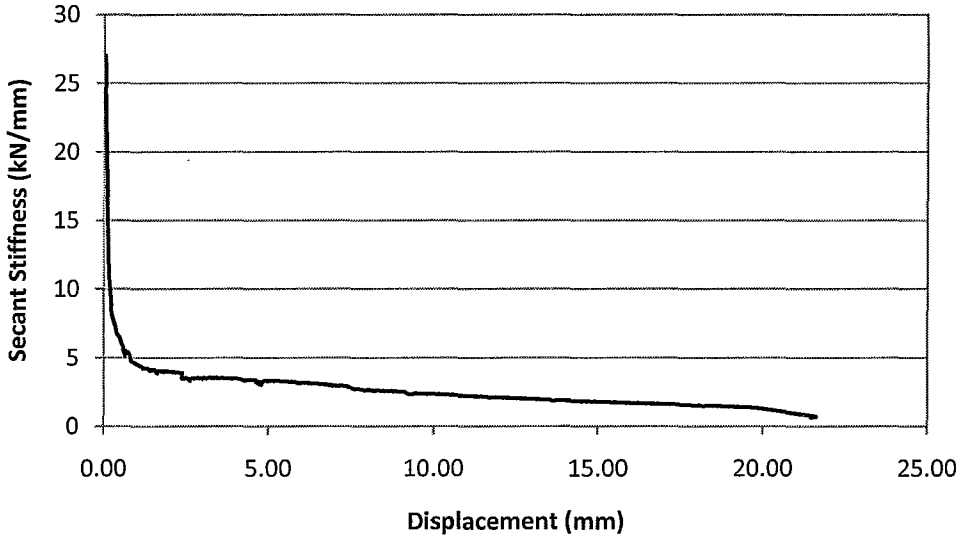

Figure 5-14: Wall 1 – Stiffness Degradation During Testing

5.3 Comparison of Wall 1 to Full-scale Experimental Data

Before a detailed comparison between the full-scale shear wall tested by Shedid (2006) and the third-scale wall described previously in this chapter it should be noted that the full-scale wall specimens were tested under fully reversed displacement controlled cycles whereas the third-scale shear walls were tested monotonically due to the limited ductility of the vertical steel reinforcement. The following section compares and relates the experimental results of the full-scale prototype testing obtained by Shedid (2006) to the third-scale results described in Section 5.2.

5.3.1 Strength Comparison

A comparison of the displacement and corresponding forces at both yield and ultimate conditions between third-scale model specimens and full-scale walls

tested by Shedid (2006) has been presented in Table 5-4. Based on the scale factors defined by Harris and Sabnis (1999) for a *practically true model* with a length scale of $S_L = 1/3$ the scaled force value is equal to $S_L^2 = 1/9$.

Table 5-4: Wall 1 – Strength Comparison of Full-scale and Third-scale Specimen

Value	Full-Scale*	Third-scale (measured)	Third-scale (expected)
Δ_y (mm)	11	4.5	3.67
F_y (kN)	174	13.3	19.3
Δ_u (mm)	24	18.7	8
F_u (kN)	242	27.7	26.9

The force values measured at yield and ultimate seemed to correlate well between third and full scale. The third-scale force measured at yield, F_y, was a little lower than scaled full-scale value would have been, whereas the third-scale force measured at ultimate loading, F_u, was predicted extremely accurately. This capacity prediction was consistent with previous reduced-scale testing completed at McMaster University by Long (2006) using half-scale masonry shear walls.

The displacement comparison between full and third-scale testing showed a greater spread between theoretical and measured scale-factors. At yield, Δ_y was approximately 7.6% higher than the theoretical scale-factor predicted. At ultimate load, the displacement recorded, Δ_u, was over 40% higher than expected.

In summary, the third-scale model of Wall 1 successfully modeled the ultimate load capacity; however the displacement values were much higher than the theoretical predictions. Heine (1997) and Jamison (1997) noticed similar trends when comparing monotonic and cyclic shear wall testing procedures for wood stud and plywood diaphragm shear walls.

5.3.2 Stiffness Comparison

Using the length factors previously defined the scale factor associated with stiffness is $S_L = 1/3$. A comparison between the full-scale shear wall specimen

tested by Shedid (2006) and the third-scale model measured stiffnesses is summarized in Table 5-5. The stiffness was measured at three points throughout testing using the secant stiffness approximation. The three stiffnesses recorded were the initial stiffness recorded prior to cracking, the stiffness as the wall reached its yield point and finally the stiffness as it reached the ultimate load.

Table 5-5: Wall 1 – Stiffness Comparison of Full-scale and Third-scale Specimen

Value	Full-Scale*	Third-scale (measured)	Third-scale (expected)
Initial Stiffness, K_i (kN/mm)	67.6	26.3	22.5
Yield Stiffness, K_y (kN/mm)	16.4	3.37	5.47
Ultimate Stiffness, K_u (kN/mm)	10.5	1.55	3.5

**full-scale data shown is from M.A.Sc. Thesis by Shedid (2006)*

The measured initial stiffness of the third-scale Wall 1 was determined to be slightly greater than the expected stiffness; 26.3 kN/mm compared to 22.5 kN/mm. This increased stiffness value is been consistent with the material properties discussed in Chapter 4. (Note that elastic modulus of the third-scale model assemblages was greater than that of the full-scale prisms tested by Shedid (2006)). After cracking was observed in the wall, the measured stiffness dropped to values lower than that of the equivalent full-scale prototype. At yield the stiffness was already less than 67% of the scale-factor prediction and by the time the specimen was pushed to ultimate load the measured stiffness had dropped to less than half of the scale factor prediction.

A possible explanation for the lower than expected measured stiffnesses could have been the presence of small grout voids within the wall specimen. No evidence of grout voids was ever found either during or after testing; however the presence of voids would account for the drop in stiffness as the specimen cracked.

5.3.3 Ductility Comparison

The load-displacement backbone curves from the full-scale prototype and third-scale model walls were normalized with respect to the wall ultimate load and yield displacement and plotted against each other for comparison in Figure 5-15.

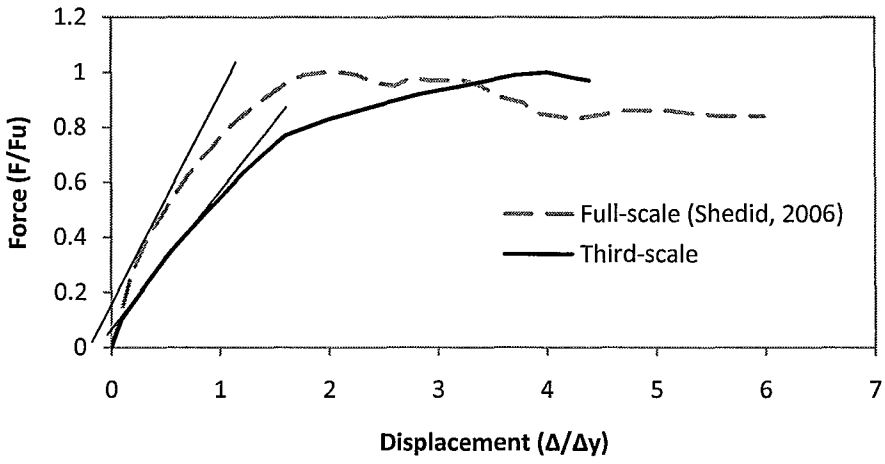

Figure 5-15: Wall 1 – Load Displacement Curve Comparison to Full-scale

The major differences between the model and prototype curves was that the location the ultimate load is achieved and the initial stiffness. The full-scale prototype specimen tested by Shedid (2006) reached ultimate load at approximately $2\Delta_y$ and then reached a plateau loading and continued to displace until the capacity of the wall deteriorated to approximately 20% of the ultimate strength. The third-scale model did not reach its ultimate strength until approximately $4\Delta_y$; after ultimate load was reached the wall did not experience the same plateau that was observed with the full-scale prototype. The definition of displacement ductility (μ_Δ) as measured in a shear wall has been previously defined as the ratio of ultimate displacement (Δ_u) to yield displacement (Δ_y);

however in this case the definition of displacement ductility is misleading. According to this definition of displacement ductility, the third-scale model shear wall appeared to have experienced a more ductile behaviour even though it did not reach a strength plateau as with the full-scale model. This is further discussed later in Section 5.3.4. A comparison of the measured ductility from both third and full-scale tests is presented in Table 5-6.

Table 5-6: Wall 1 – Ductility Comparison of Full-scale and Third-scale Specimen

Value	Full-Scale*	Third-scale (measured)	Third-scale (expected)
Δ_y (mm)	11	4.5	3.67
F_y (kN)	174	13.3	19.3
Δ_u (mm)	24	18.7	8.0
F_u (kN)	242	27.7	26.9
μ_Δ	2.2	4.2	2.2

**full-scale data shown is from M.A.Sc. Thesis by Shedid (2006)*

5.3.4 Load-Displacement Response Idealization

Different idealization techniques have been proposed throughout the years by researchers such as Tomazevic (1999) and Priestly, et al. (1992) in order to effectively define shear wall ductility as a function of force and displacement. The benefit of such idealization techniques is the ability to compare experimental test results and ulimately more effectively understand the behaviour of shear walls. The idealization technique described in this section is a adaptation of the bilinear idealization proposed by Tomazevic (1999). The technique was used previously with success by Long (2006) to relate hlaf-scale model shear wall test specimens to full-scale prototype walls tested by Shedid (2006). The bilinear idealization has been defined as follows:

1. Effective stiffness (EI_{eff}) is measured using the secant stiffness of the load-displacement backbone curve at 75% of the maximum load resisted by the wall (F_{max}).

2. The ulimate displacement (Δ_u) was defined as the point as which the wall capacity deteriorated to a level at which the "failure" occurred. This point is defined as the displacement along the decending branch of the load-displacement curve where the wall was resisting less than 20% F_{max}. This point varied slightly between full-scale prototype and third-scale model specimens as the model did not reach 20% strength degration on its decending branch prior to the rupturing of the vertical reinforcement.
3. The idealized maximum force (F_u) is determined by equating the area under actual load-displacement backbone curve to that of the proposed idealization using the slope determined by EI_{eff} and the final displacment Δ_u.
4. The idealized yield displacement is found by dividing F_u by the effective stiffness; $\Delta_y = F_u / EI_{eff}$.
5. The displacment ductility discussed in the previous section is defined as the ratio of ultimate displacement to displacement at yield; $\mu_\Delta = \Delta_u / \Delta_y$.

The idealization technique described above has been applied to both the third-scale model shear wall and the full-scale prototype shear wall tested by Shedid (2006) in Figure 5-16 and Figure 5-17, respectively. The values defined by the idealization have been identifed on each figure. The horizontal and vertical lines displayed on each idealization graph represent the intersection point between the idealization and the actual load-displacement backbone curve.

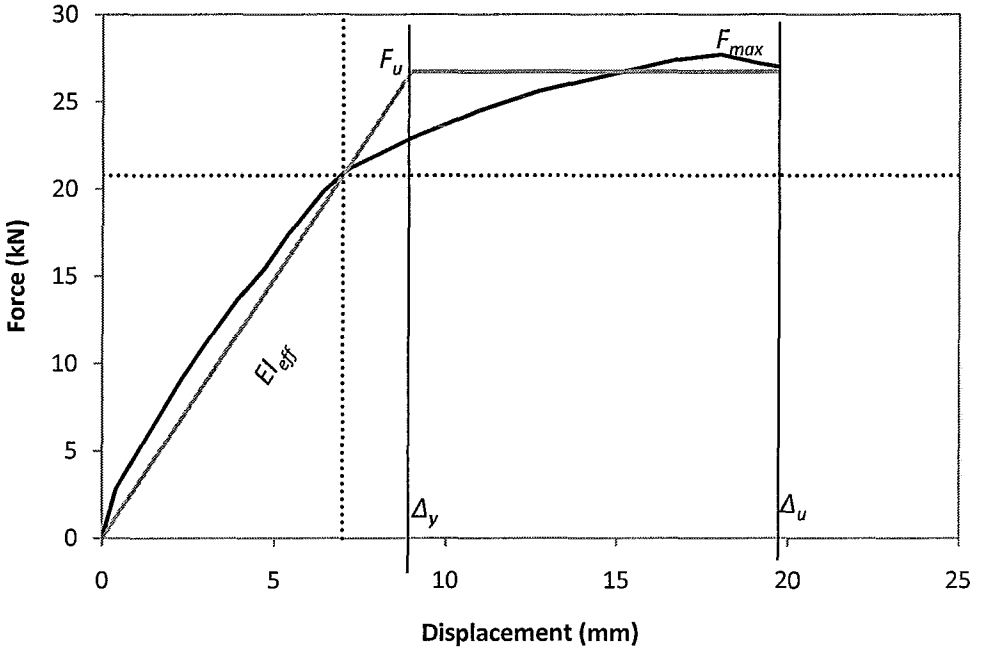

Figure 5-16: Wall 1 – Third-scale Force Displacement Idealization

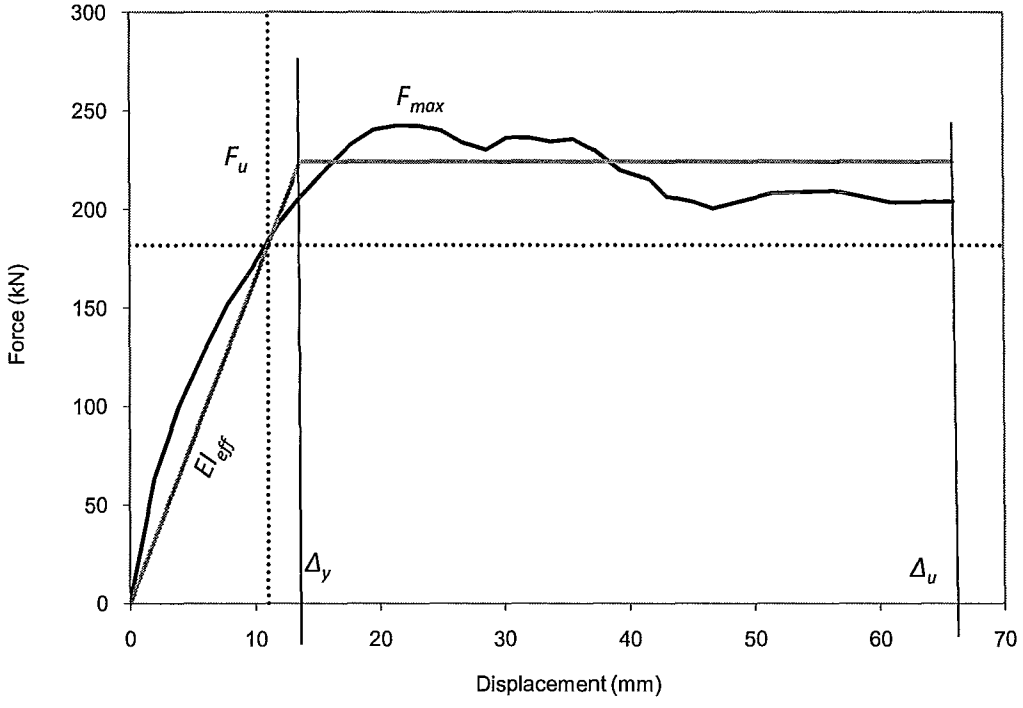

Figure 5-17: Wall 1 – Full-scale Force Displacement Idealization

The key parameters defined throughout the idealization described previously are summarized in Table 5-7. Recall that in Section 5.3.3, the displacement ductility, μ_Δ, of the third-scale wall was greater than that of the full-scale prototype; however using the values determined from the load-displacement idealization the full-scale specimen had the greater displacement ductility value.

Table 5-7: Wall 1 – Comparison of Full-scale and Third-scale Load Displacement Idealizations

Value	Full-Scale*	Third-scale (measured)	Third-scale (expected)
F_{max} (kN)	242.4	27.7	26.9
F_u (kN)	181.8	20.8	20.2
EI_{eff} (kN/mm)	16.53	2.97	5.5
Δ_y (mm)	13.56	9.00	4.5
Δ_u (mm)	65.93	19.7	22.0
μ_Δ	4.86	2.19	4.86

**full-scale data shown is from M.A.Sc. Thesis by Shedid (2006)*

The results from the idealization support the conclusions made by Shedid (2006) that if reinforced masonry shear walls are adequately reinforced they are capable of experiencing much higher levels of ductility than the current values in the National Building Code, NBCC (2010), allows. It is a conservative assumption to limit the displacement ductility to the to the ultimate displacement as defined as the maximum applied force since the wall specimen typically continues to displace without much strength degradation, as illustrated in Figure 5-17.

The idealization results are also clearly indicate that the third-scale masonry shear walls did not achieve the expected level of ductility compared to the full-scale model tested by Shedid (2006). This phenomenon has been attributed to the brittle vertical reinforcing that ruptured prior to the full development of compressive stress in the model masonry.

The effective stiffness (EI_{eff}) measured through the load-displacement idealization was consistent with the measured stiffness found when the experimental load-displacement curves of the model and prototype were compared. The third-scale model had a lower stiffness than the full-scale prototype. As mentioned previously, this phenomenon could be explained by the presence of unseen grout voids.

5.4 Experimental Results – Wall 2

5.4.1 Wall 2 Details

Wall 2 was reinforced with nine D7, deformed wires, used as vertical bars (A_s = 45 mm^2) with a spacing between the bars of 66.7 mm (every other cell) and eighteen W1.7, smooth wires, used as horizontal reinforcement (A_s = 11 mm^2) spaced at 133.3 mm increments. The wall was loaded laterally, in-plane, at the top of the wall in the same manner as Wall 1. The wall was also subject to a "calibrating" cycle at approximately 25% of the theoretical load to ensure that all instrumentation was working adequately.

5.4.2 General Observations

The initial load-displacement cycle occurred at approximately 25% of the theoretical yield force. The load applied to the shear wall is plotted against the displacement measured at the point of loading (top of the wall specimen) over the duration of the experiment in Figure 5-18. General observations recorded over the course of this experiment are described in this section of the thesis.

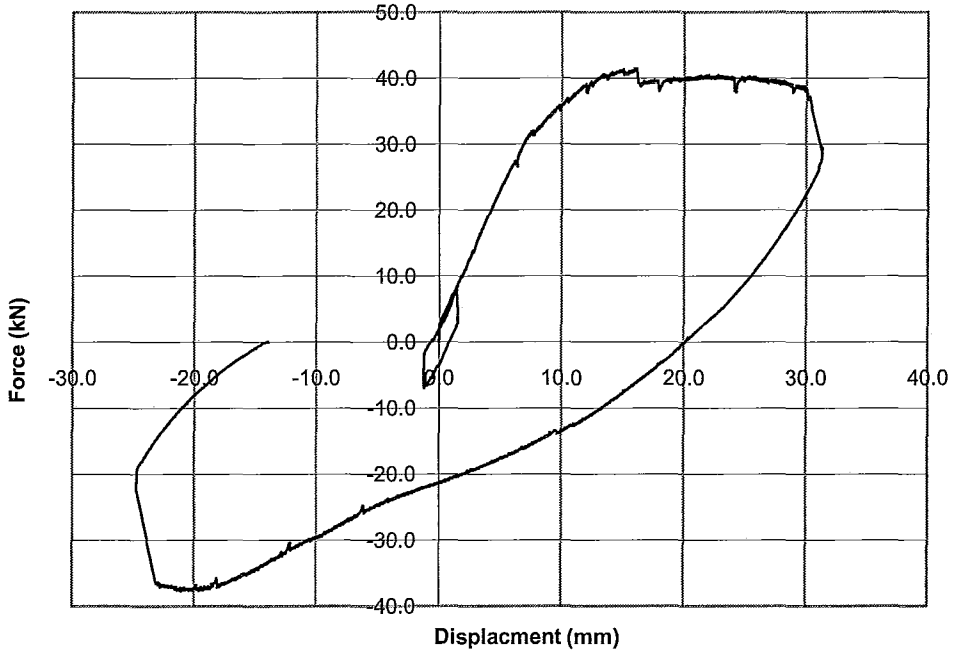

Figure 5-18: Wall 2 - Load-Displacement Response Curve

Bed joint cracks along mortar joints at 5th, 8th, and 10th courses from the bottom of the wall appeared at as early as 25% theoretical yield force. The yielding of the extreme vertical tensile bar was determined using the internal strain gauge located at the interface between the concrete base beam and the bottom course of wall. The lateral displacement recorded wall top as the extreme tensile bar yielded was 6.0 mm; this displacement was then used as an incremental displacement point at which loading was paused during testing so that measurements could be taken and cracks photographed. The extent of bed joint cracking at the yield displacement, Δ_y, is shown in Figure 5-19. Bed joint cracking at yield occurred between all courses up to half of the wall height (see Figure 5-19).

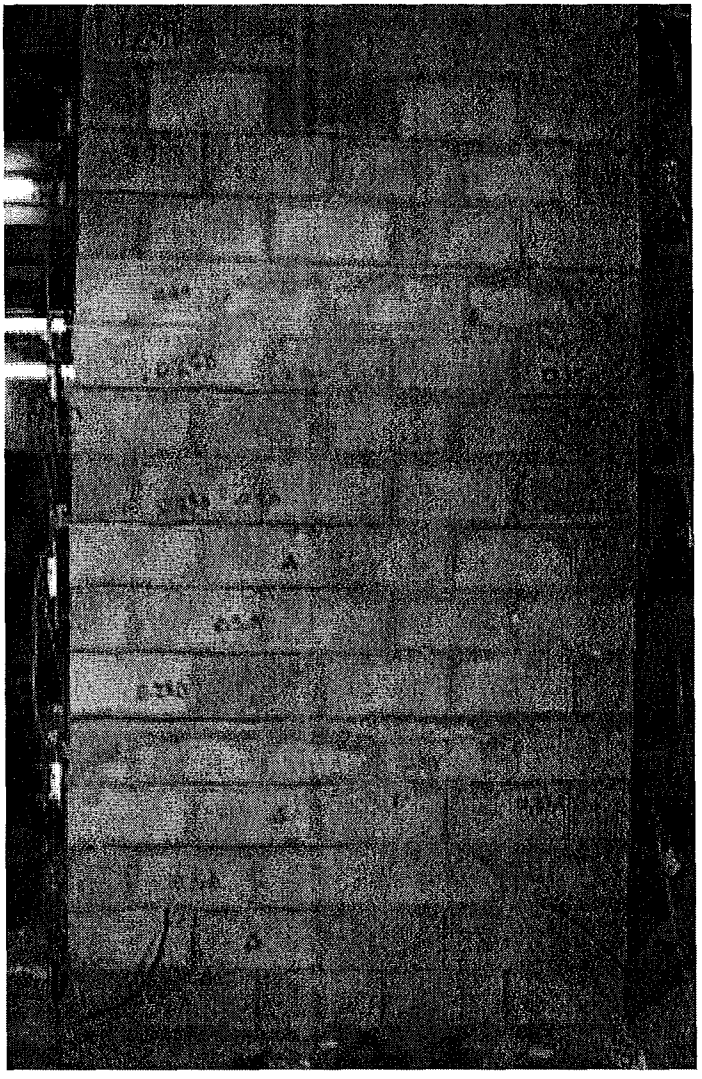

Figure 5-19: Wall 2 – Bed Joint Cracking at Δ_y

As the wall specimen was loaded to 12 mm ($2\Delta_y$) lateral displacement at the wall top, diagonal tension cracking was observed. The diagonal tension cracks stepped down from the point of lateral load application to the compression toe. Some of the diagonal cracks seemed to follow the mortar joints while other cracked through the face shells of the concrete blocks. At this point no visible compression cracking was observed within the extreme compression region of the

wall specimen. The extent of the crack propagation up until $2\Delta_y$ can be seen in Figure 5-20.

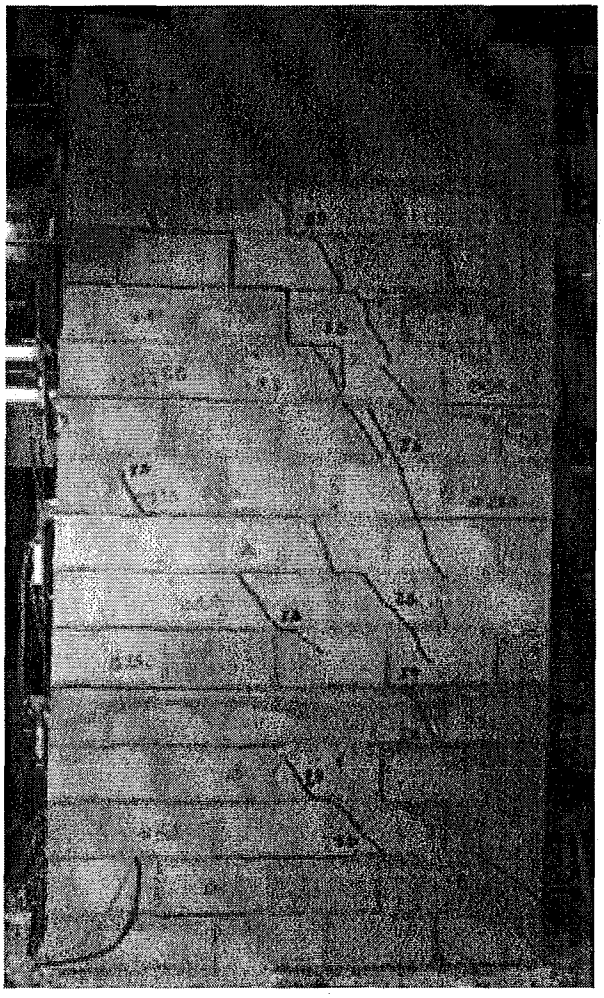

Figure 5-20: Wall 2 – Diagonal Tension Cracking at $2\Delta_y$

As the wall specimen reached $3\Delta_y$ displacement (18 mm) more diagonal cracking was observed. At this point the bed joint cracks observed between courses continued to widen but were not continuing to propagate. Compression cracking was observed through the end webs of the bottom two blocks within the compression toe region of the wall.

As the wall was pushed to 24 mm ($4\Delta_y$) lateral displacement, the diagonal tension cracking remained unchanged since the $3\Delta_y$ displacement increment. The compression toe cracking that was first noticed during the $3\Delta_y$ displacement cycle continued to lengthen and was now projecting into the third block course from the bottom of the wall. Some face shell spalling was observed on one side of the wall specimen. The extent of cracking up until the $4\Delta_y$ displacement increment can be seen in Figure 5-21.

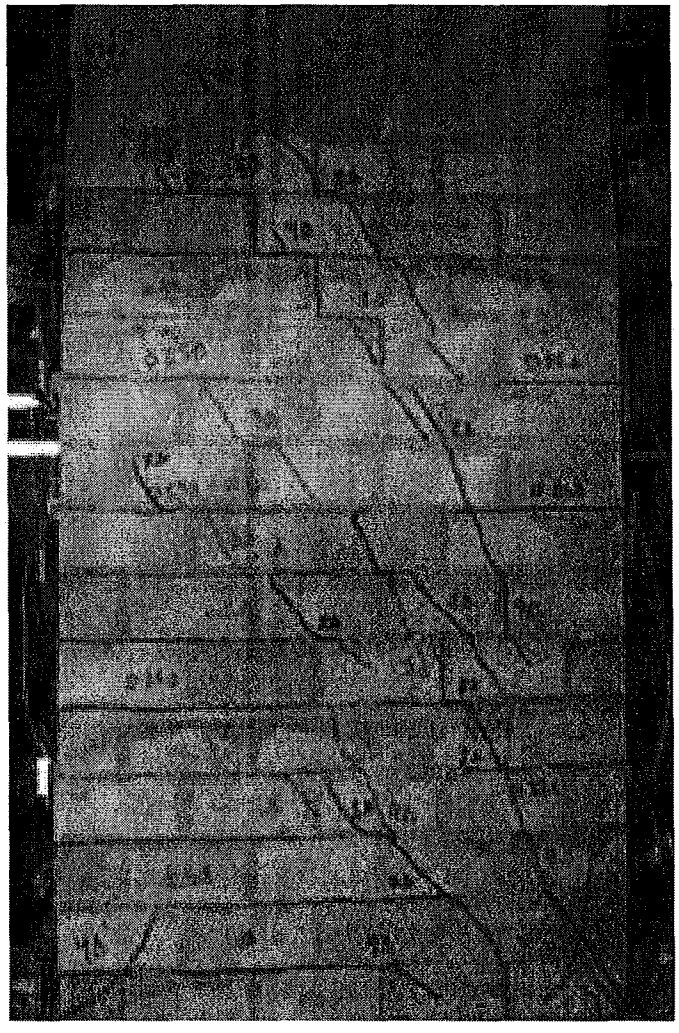

Figure 5-21: Wall 2 - Diagonal Tension Cracking at $4\Delta_y$

The face shell spalling that was observed within the compression toe of the wall during the $4\Delta_y$ displacement increment was characteristic of a typical shear wall flexural failure mode (Drysdale & Hamid, 2005). Figure 5-22 displays a close up view of the observed face shell spalling. The image on the left of Figure 5-22 shows the side view of the wall, clearly displaying the face shell spalling of the first block in the bottom course. The image on the right of Figure 5-22 displays the end view of the wall. The propagation of the vertical compression cracking up the top of the third block course is easily observed.

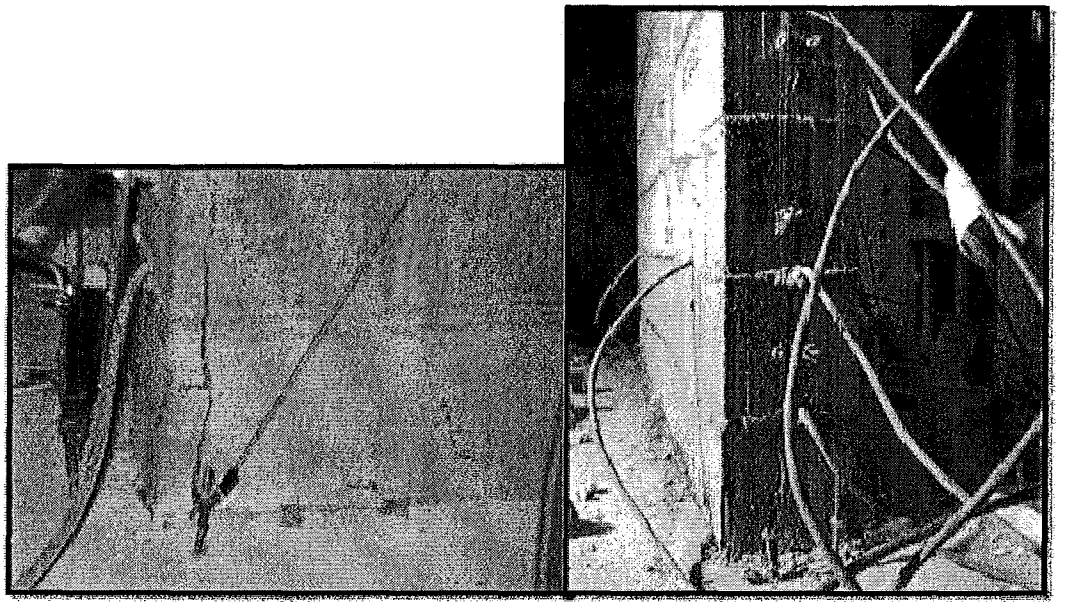

Figure 5-22: Wall 2 - Face Shell Spalling at Compression Toe ($4\Delta_y$)

As the wall specimen was pushed just beyond 30 mm displacement ($5\Delta_y$) at the wall top, the extreme tensile bar ruptured. At this point the face shells of both sides of the compression toe region of the wall had spalled off. The grout core was still intact without the presence of visible cracking. The fact that the grout core was still intact suggests that that limiting factor controlling the lateral displacement of the test specimen was the vertical steel as the masonry did not

reach its full compressive potential. The grout core along with the remainder of the compression toe can be seen in Figure 5-23.

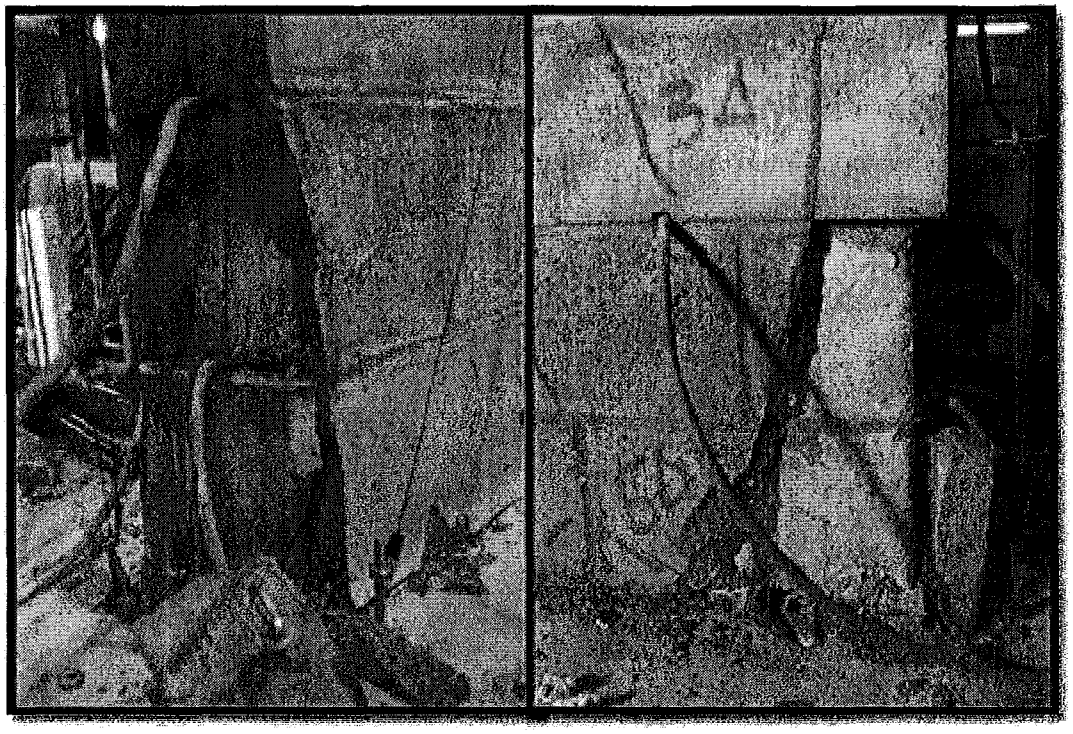

Figure 5-23: Wall 2 - Extent of Face Shell Spalling in Compression Toe (after test)

After the wall specimen reached failure in the push loading condition, the loading cycle was reversed so that the other side of the wall could be tested. Just as with Wall 1, it was assumed that the effect of the compression steel (that had ruptured in tension) on the compression toe of the untested side of the wall would be negligible. The wall was loaded incrementally in pull using multiples of yield displacement much like with the primary push loading. The pull loading continued until the extreme tensile bar on the other side of the wall ruptured in tension. At the end of the testing procedure at least one tensile reinforcing bar had ruptured on each side of the wall.

The crack pattern observed during the pull loading mirrored that recorded during the push loading condition and much like as seen in Wall 1 the line of symmetry was shifted from centre of the wall unlike what was originally expected. The slightly shifted centre-line of reflection along with the final crack propagation was again attributed to the damage caused to the wall during the push phase of the monotonic test procedure. The extent of the crack propagation during testing can be seen in Figure 5-24.

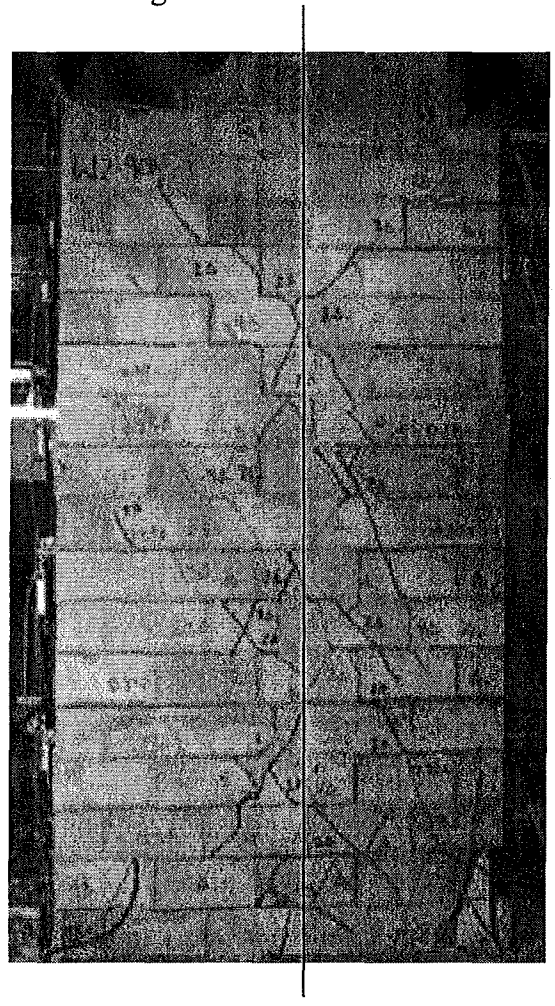

Figure 5-24: Wall 2 – Extent of Crack Propagation (after testing)

5.4.3 Load-Displacement Response

The load displacement response of Wall 2 is shown in Figure 5-18. Just as described with Wall 1, the specimen was loaded monotonically in the push direction until it reached failure after which it was pulled back in the opposite direction. As a result of this monotonic loading technique, the load-displacement curve obtained during the pull phase was not symmetrical with the push phase. However, the load displacement curve obtained during the initial push phase of loading seemed to represent the backbone curve of the full-scale walls tested by Shedid (2006). A more detailed comparison of third-scale and full-scale load displacement relationships will be discussed later in the chapter. The backbone curve is shown in Figure 5-25.

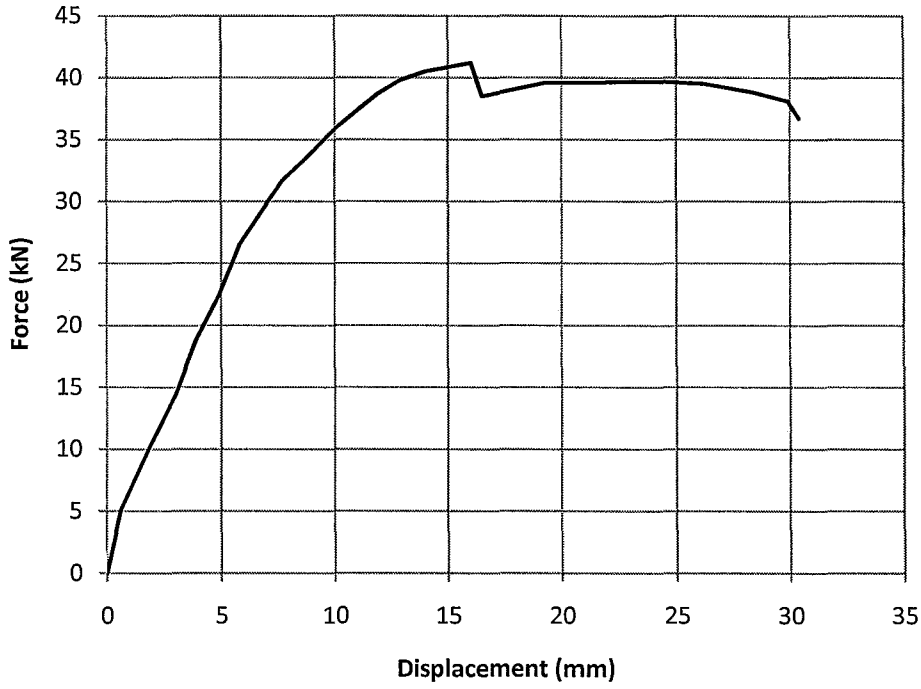

Figure 5-25: Wall 2 – Load vs. Displacement Backbone Curve

The wall response was almost linear elastic up to the yielding of the extreme tensile bar (Δ_y = 6.0 mm). The corresponding lateral force, F_y, applied to the top of the wall was 24.7 kN. As expected, after the yielding of the extreme tensile bar, the stiffness of the wall decreased as the in-plane deformation increased. The wall reached its ultimate load, F_u, of 41.0 kN at 16.4 mm displacement. The test ended as the extreme tensile bar ruptured. The bar rupture occurred at 30.3 mm lateral wall top displacement. The corresponding lateral force acting on the wall at this point was 36.6 kN, approximately 89.3% of the ultimate strength.

After examination of the plotted backbone curve in Figure 5-25 it was determined that the extreme tensile reinforcing bar most likely ruptured as the ultimate load was reached (characterized in Figure 5-25 by a sudden drop in force). The loading on the wall at this point dropped to the capacity of a shear wall specimen that was one cell shorter in wall length. This occurrence did not impact the measured displacement values used to quantify displacement ductility, μ_Δ, as it occurred after ultimate load was reached.

5.4.4 Experimental Results Compared to Predictions

A comparison between measured and predicted behaviour of Wall 2 is summarized in Table 5-8. Displacements and corresponding forces at both yield and ultimate displacements were calculated using basic flexural theory. The equations used are discussed in detail in Appendix C. The material properties used for the predictions were input based the testing of the construction assemblages discussed in Chapter 4. Similarly to Wall 1, ultimate displacement values (Δ_u) were determined using the assumption that the walls would behave as shear walls with limited ductility as defined by CSA S304.1 (2004). The predicted values are estimated using the assumption that the wall had a plastic hinge length equal to half of the length of the wall.

Table 5-8: Wall 2 – Predicted and Experimental Comparison

	Predicted (ε_u = 0.0025)		Experimentally Measured
	excluding	including	Push-over loading condition (monotonic)
Value	comp. steel	comp. steel	
Δ_y (mm)	2.9	2.8	6.0
F_y (kN)	32.4	31.5	24.7
Δ_u (mm)	6.5	7.1	16.44
F_u (kN)	40.5	40.6	41.0
$\mu_\Delta = \Delta_u/\Delta_y$	2.28	2.50	2.74
	Predicted (ε_u = 0.003)		
Δ_y (mm)	2.9	2.8	
F_y (kN)	32.4	31.5	
Δ_u (mm)	7.4	8.3	
F_u (kN)	40.9	43.0	
$\mu_\Delta = \Delta_u/\Delta_y$	2.60	2.92	

As with Wall 1, as predicted values for both limiting masonry strains of 0.0025 and 0.003 have been included in Table 5-8 for comparison purposes. Similarly to Wall 1, the inclusion of compression steel increased the expected ultimate strength (F_u) as well as the expected ductility (measured by displacement ductility, μ_Δ).

The values listed under the experimentally measured column of Table 5-8, correspond to the plotted load-displacement curve, Figure 5-25. The measured initial yield displacement (Δ_y) was found to be approximately 100% greater than the theoretical displacement determined using beam theory. The force applied to the wall at the point of yield displacement (F_y) was lower than expected 24.7 kN measured compared to 32.4 kN predicted. The ultimate capacity, F_u, recorded at 41.0 kN of the wall was predicted with excellent accuracy to within 0.9% (including compression steel) at 40.6 kN and 1.0% (neglected compression steel) at 40.5 kN. The displacement recorded as the wall specimen reached its ultimate

load, Δ_u, was 16.4 mm. This value was much higher than the expected 6.5 mm. With the inclusion of compression steel in the prediction and the assumption that the compressive strain in the masonry could reach 0.003 the prediction was 8.3 mm at ultimate.

5.4.5 Extent of Yielding Within Vertical Reinforcement

As previously discussed in Chapter 4, the outer most vertical reinforcing bars were instrumented with strain gauges in an attempt to measured the extent of yielding and plasticity within the shear wall. The yield strain of the vertical D7 reinforcing bars was experimentally determined to be 0.0027. All the strain gauges attached to the outer most tensile bar appeared to be functioning adequately throughout testing for Wall 2. The yield point was determined using a combination of theoretical yield force as well at experimental yield of the vertical bar in the end cell. The extent of yielding of the outermost vertical reinforcing bars is summarized in Table 5-9.

Table 5-9: Wall 2 – Extent of Yielding of Vertical Reinforcing

Strain Gauge Location (height from base beam, mm)	Initial Yield Condition (ε_y = 0.0027)			Ultimate Load (41.0 kN)	
	Load (kN)	Displacement (mm)	Drift (%)	Strain (ε_s)	Factor X ε_y
Interface (0)	24.7	6.00	0.53	---	---
165	28.9	7.10	0.59	0.007330	2.71
280	31.5	8.06	0.67	0.003468	1.28

As mentioned previously, the yielding of the outermost tensile bar occurred at the interface between the concrete base and the wall at a lateral displacement (top of wall) of 6 mm and an applied force of 24.7 kN. Yielding extended up the vertical bar to 165 mm from the interface at an applied load of 28.9 kN and to 280 mm from the interface at 31.5 kN.

5.4.6 Lateral Deformations of Wall 2

The in-plane lateral displacement of Wall 2 was measured at six locations along the height of the wall. The displacement values, with respect to the wall height, are provided in Figure 5-26. For the most part, the displacement appeared to be linear. It appeared as though flexural deformation occurred in lower 400 mm of the wall. This is consistent with the yielding of the extreme tensile bars, as the yielding extended past 280 mm from the interface between the concrete base and the bottom of the wall. The flexural deformation within Wall 2 appeared to be isolated into a lower segment of the wall than was previously noticed in Wall 1.

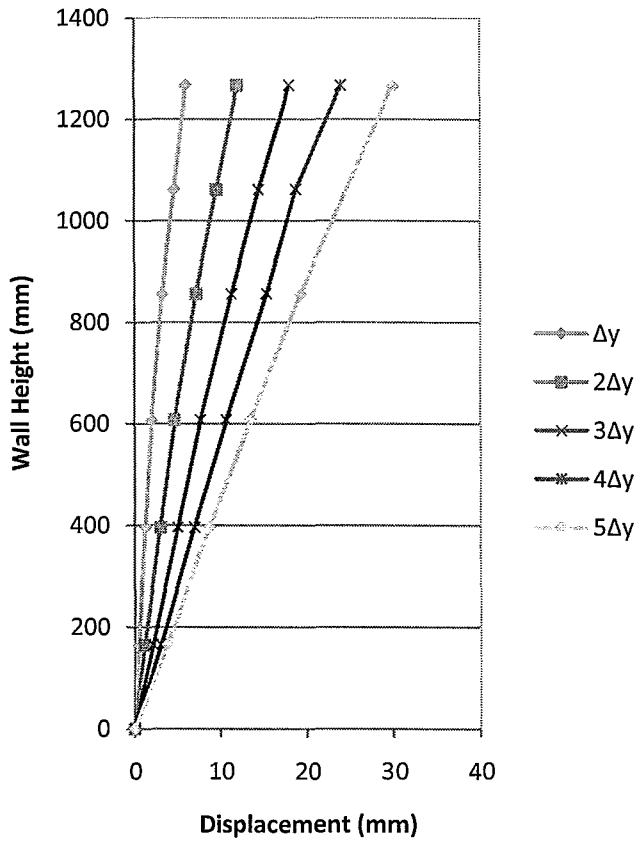

Figure 5-26: Wall 2 – Lateral Displacement with Respect to Height

5.4.7 Wall Curvature

The average curvatures were measured over the height of wall 2 using compressive and tensile strains in six gauge lengths identified in Chapter 4. A detailed explanation with respect to the calculation of average curvatures can be found in the Appendix A of this thesis. The average curvature along the height of wall 1 can be found in Figure 5-27.

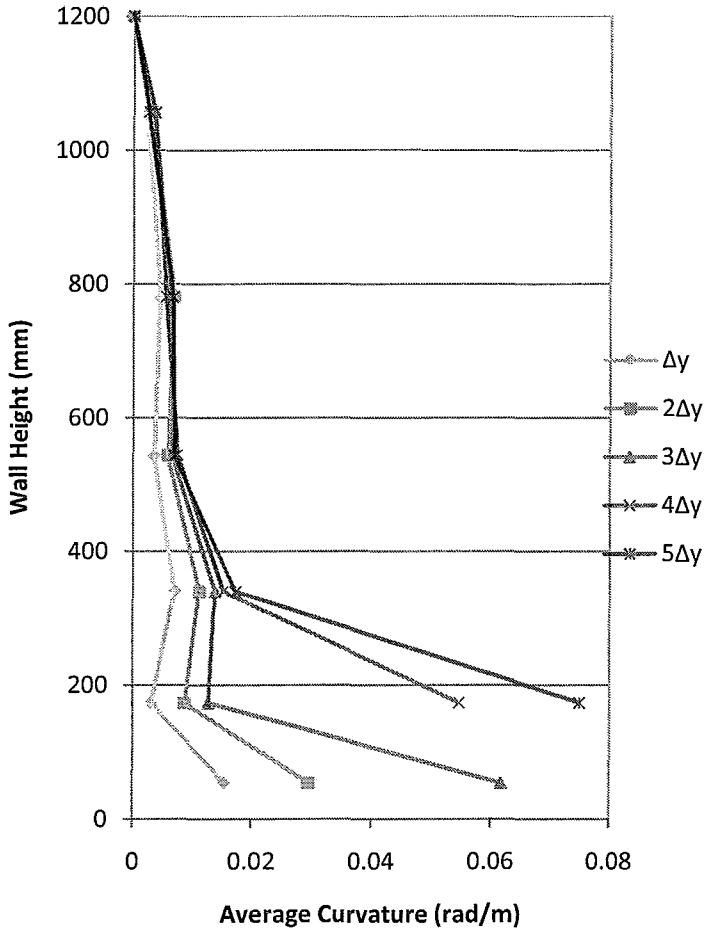

Figure 5-27: Wall 2 – Curvature Profile

The measured average curvature at yield, φ_y, was 0.0155 rad/m which was approximately triple the predicted average curvature of 0.0059 rad/m at the base

of the wall. A detailed description of the theoretical curvature predictions can be found in the Appendix C. Average curvature, measured over the bottom segment of the wall, at ultimate loading, φ_p, was equal to 0.0617 rad/m was approximately four times the curvature measured at initial yield and again approximately triple the predicted average curvatures using the method described in the Appendix A. Just as with Wall 1, the expected curvature values were much lower than those measured experimentally. This is consistent with the trend observed by Sasani and Kiureghian (2001).

As the wall specimen was pushed beyond $3\Delta_y$ the LVDT measuring curvature on the compression side of the wall had to be removed due to face shall spalling at its location. As a result curvature could not be measured over the bottom wall segment for the remainder of the test.

Overall the average curvature profile was consistent with the shape expected through comparison with the full-scale shear walls tested by Shedid (2006). The average curvature plotted against the height of the full-scale wall tested by Shedid (2006) is shown in Figure 5-28 for comparison purposes. The average curvature measured at the bottom wall segment for the third-scale wall was expected to be one third of the full-scale wall measured by Shedid (2006). This ratio appeared to be maintained throughout testing.

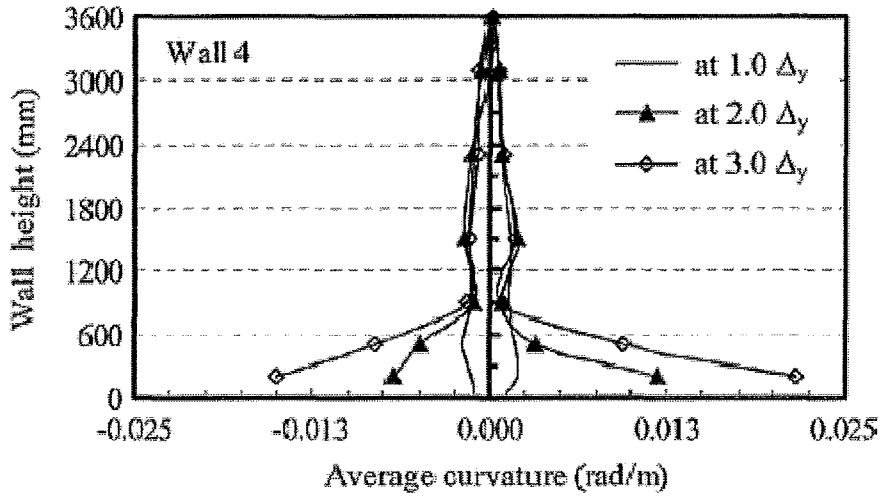

Figure 5-28: Average Curvature for Full-scale Wall Prototype (Shedid, 2006)

5.4.8 Strain Profile

The strain profile was recording using four LVDT's, as described in Chapter 4, along the length of the wall specimen at two gauge heights. The first gauge height measured strain from the base beam to approximately 105 mm above the base, see Figure 5-29. The second gauge height measured strains from 105 mm to 245 mm above the base, see Figure 5-30. The sign convention of the strain profile figures shows compressive strains as positive values.

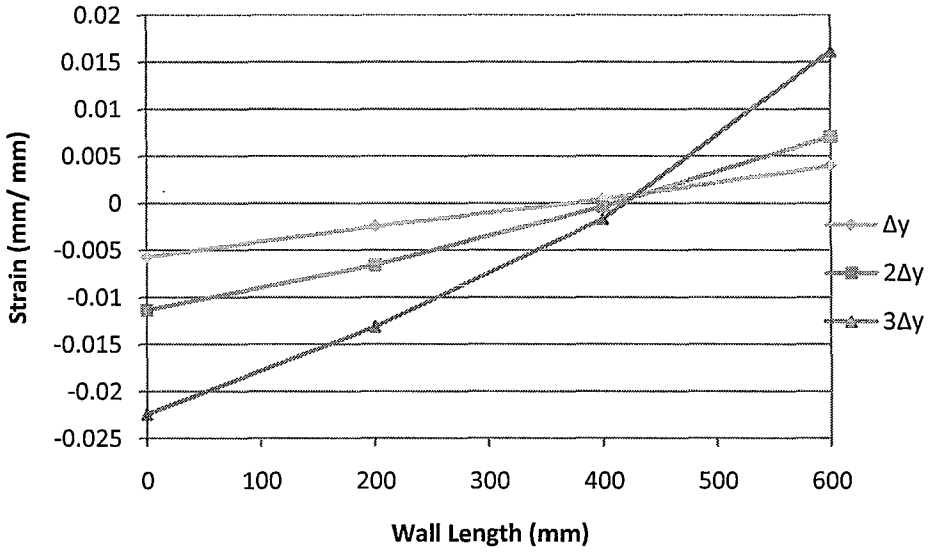

Figure 5-29: Average Strain along Length of Wall 2 (0 – 105 mm above base)

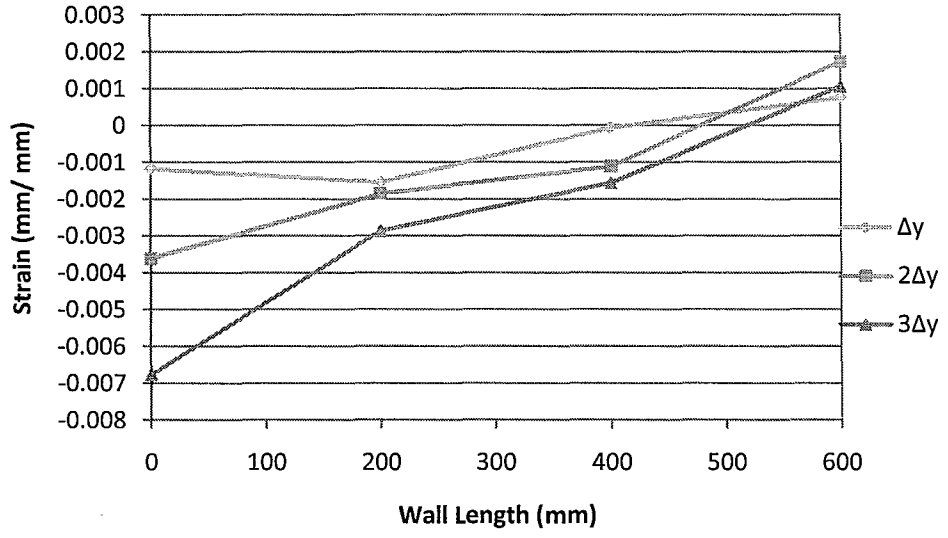

Figure 5-30: Average Strain along Length of Wall 2 (105 – 245 mm above base)

The lengths of the compression zone were inconsistent between gauge heights, showing the compression zone at just under 200 mm in length for the lower gauge and just over 100 mm for the upper gauge height. In general, the strain profile was almost linear at yield displacement where the compression strain was 3.97×10^{-3}. The maximum compressive strain recorded was 16.1×10^{-3} and occurred at the $3\Delta_y$ displacement. The maximum compressive strains were well over the CSA S304.1 limit of 3×10^{-3}. This is consistent with the higher that theoretically predicted measured average curvatures and with the strains measured in Wall 1.

5.4.9 Stiffness Degradation

The theoretically predicted stiffness values for Wall 2 were approximated to provide some relevance to the measured stiffnesses plotted in Figure 5-31. A detailed description of the theoretical stiffness calculation can be found in the Appendix B. The predicted stiffness values obtained prior to testing are shown in Table 5-10. The stiffness values found in Table 5-10 were calculated using the individual material properties of the shear wall.

Table 5-10: Wall 2 – Summary of Theoretical Wall Stiffness Predictions

Value	Full-Scale* prediction	Third-scale prediction	Third-scale (1/3 of full-scale)
Gross Stiffness, K_g (kN/mm)	73.64	35.04	24.5
Cracked Stiffness, K_{cr} (kN/mm)	24.36	5.92	8.1

**full-scale data shown is from M.A.Sc. Thesis by Shedid (2006)*

A complete comparison of the third-scale and full-scale specimens tested by Shedid (2006) can be found in Section 5.5. The following figure describes the stiffness deterioration of the third-scale, Wall 2, during the testing procedure. The initial stiffness, K_i, was measured as 29.0 kN/mm which deteriorated to 4.5 kN/mm at yield and finally to 2.6 kN/mm at ultimate load. The stiffness degradation shown in Figure 5-31 was consistent with the expected deterioration.

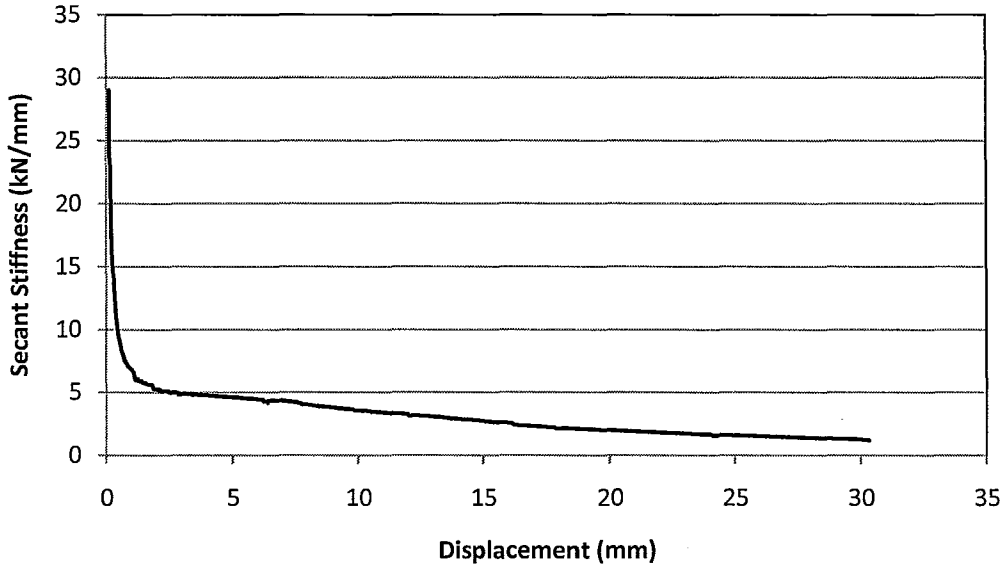

Figure 5-31: Wall 2 – Stiffness Degradation During Testing

5.5 Comparison of Wall 2 to Full-scale Experimental Data

The following section compares and relates the experimental results of the full-scale prototype testing obtained by Shedid (2006) to the third-scale results described in Section 5.4 for Wall 2.

5.5.1 Strength Comparison

A comparison of the displacement and corresponding forces at both yield and ultimate conditions between third-scale model specimens and full-scale walls tested by Shedid (2006) is presented in Table 5-11.

Table 5-11: Wall 2 – Strength Comparison of Full-scale and Third-scale Specimens

Value	Full-Scale*	Third-scale (measured)	Third-scale (expected)
Δ_y (mm)	15	6.0	5.0
F_y (kN)	296	24.7	32.9
Δ_u (mm)	30	16.44	10.0
F_u (kN)	360	41.0	40.0

**full-scale data shown is from M.A.Sc. Thesis by Shedid (2006)*

Consistent with results from Wall 1, the force values measured at yield and ultimate seemed to correlate well between third and full scale. The third-scale force measured at yield, F_y, was slightly lower than scaled full-scale value would have been, whereas the third-scale force measured at ultimate loading, F_u, was predicted extremely accurately. This capacity prediction was consistent with previous reduced-scale testing completed at McMaster University by Long (2006) using half-scale masonry shear walls.

The displacement comparison between full and third-scale testing showed a greater spread between theoretical and measured scale-factors. At yield, the third-scale Δ_y displacement was approximately 6.6% higher than the theoretical scale-factor predicted. At ultimate load, the displacement recorded, Δ_u, was over 20% higher than the equivalent full-scale prototype.

In summary, the third-scale model of Wall 2 successfully modeled the ultimate load capacity of the wall specimen; however the displacement values were much higher than the theoretical predictions.

5.5.2 Stiffness Comparison

A comparison between the full-scale shear wall specimen tested by Shedid (2006) and the third-scale model (Wall 2) measured stiffnesses is summarized in Table 5-12. Recall that the scale-factor used to relate model stiffness to prototype is $S_L = 1/3$. The stiffness was measured at three points throughout testing using the secant stiffness approximation. The three stiffnesses recorded were the initial

stiffness recorded prior to cracking, the stiffness as the wall reached its yield point and finally the stiffness as it reached the ultimate load.

Table 5-12: Wall 2 – Stiffness Comparison of Full-scale and Third-scale Specimens

Value	Full-Scale*	Third-scale (measured)	Third-scale (expected)
Initial Stiffness, K_i (kN/mm)	85.94	29.0	28.6
Yield Stiffness, K_y (kN/mm)	19.61	4.48	6.53
Ultimate Stiffness, K_u (kN/mm)	11.94	2.57	3.98

**full-scale data shown is from M.A.Sc. Thesis by Shedid (2006)*

The initial stiffness of the third-scale Wall 2 was very close the scaled full-scale prediction, 29 kN/mm compared to 28.6. After cracking was observed in the wall, the measured stiffness dropped to values lower than that of the equivalent full-scale prototype. At yield the stiffness was already less than 67% of the scale-factor prediction and by the time the specimen was pushed to ultimate load the measured stiffness had dropped even farther from the expected stiffness.

Much like with as noticed with Wall 1, the theoretically predicted stiffness values determined using individual material properties (shown in Table 5-10) was higher than the experimentally measured values summarized in Table 5-12.

5.5.3 Ductility Comparison

The load-displacement backbone curves from the full-scale prototype and third-scale model were normalized with respect to the wall ultimate load and yield displacement and plotted against each other for comparison in Figure 5-32.

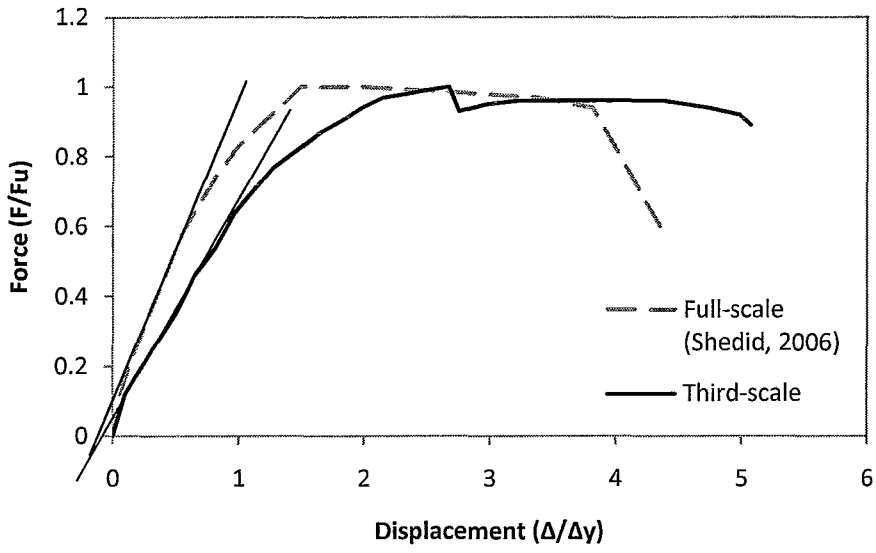

Figure 5-32: Wall 2 – Load Displacement Curve Comparison to Full-scale

As noted with Wall 1, the major differences between the model and prototype curves were that the location the ultimate load is achieved and the initial stiffnesses. The full-scale prototype specimen tested by Shedid (2006) reached ultimate load at approximately $1.5\Delta_y$ and then reached a plateau loading and continued to displace until the extreme tensile bar ruptured (Shedid, 2006). The third-scale model did not reach its ultimate strength until approximately $2.5\Delta_y$. After ultimate load was reached the wall did seem to experience a strength plateau, much like that of the full-scale prototype; however, as mentioned in Section 5.4.3, it appeared as though the extreme tensile bar ruptured as the wall reached its ultimate capacity.

As noticed with Wall 1, the measured displacement ductility for this wall was not representative of the brittle failure that was observed shortly after ultimate load was reached. Table 5-6 summarizes that displacement ductility

values measured during the testing of Wall 2 and compares them to the full-scale prototype wall tested by Shedid (2006). The prototype wall has a $\mu_\Delta = 2.0$ while the third-scale wall had a $\mu_\Delta = 2.74$.

Table 5-13: Wall 2 – Ductility Comparison of Full-scale and Third-scale Walls

Value	Full-scale*	Third-scale	Third-scale (expected)
Δ_y (mm)	15	6.0	5.0
F_y (kN)	296	24.7	32.9
Δ_u (mm)	30	16.44	10.0
F_u (kN)	360	41.0	40.0
μ_Δ	2	2.74	2

**full-scale data shown is from M.A.Sc. Thesis by Shedid (2006)*

5.5.4 Load Displacement Response Idealization

The idealization technique described in Section 5.3.4 is applied to both the third-scale model shear wall and the full-scale prototype shear wall tested by Shedid (2006) in Figure 5-33 and Figure 5-34, respectively. The values defined by the idealization are identifed on each figure. The horizontal and vertical lines displayed on each idealization graph represent the intersection point between the idealization and the actual load-displacement backbone curve.

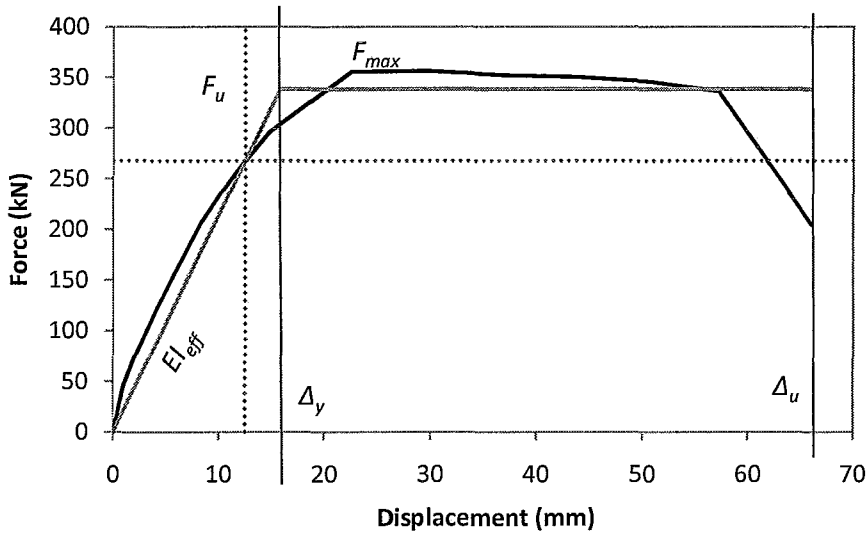

Figure 5-33: Wall 2 – Full-scale Force Displacement Idealization

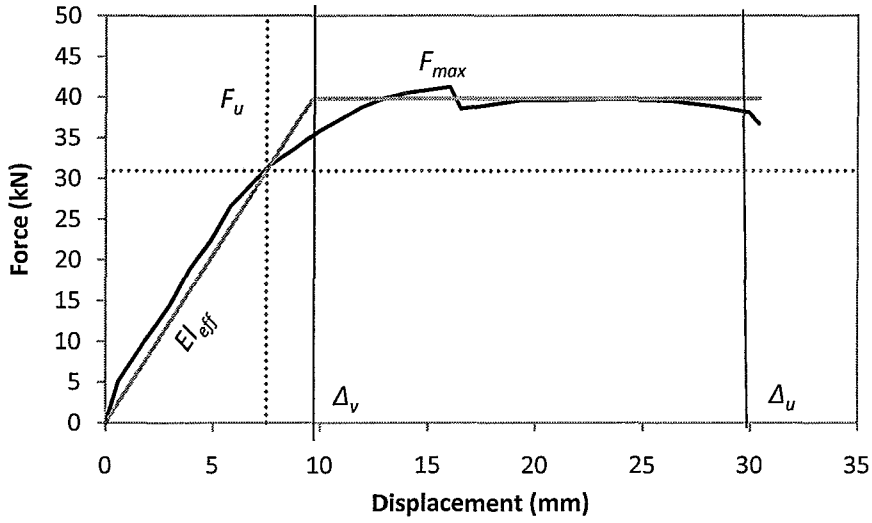

Figure 5-34: Wall 2 – Third-scale Force Displacement Idealization

The key parameters defined throughout the idealization described in Section 5.3.4 have been summarized in Table 5-14. Recall that in Section 5.5.3, the displacement ductility, μ_Δ, of the third-scale wall was greater than that of the

full-scale prototype; however using the values determined from the load-displacement idealization the full-scale specimen had the greater displacement ductility value. This result is consistent with the idealization results from Wall 1.

The idealization provides a better ductility characterization of the shear walls, both model and prototype, and it clearly demonstrates the ability to deform well into the inelastic range.

Table 5-14: Wall 2 – Comparison of Full-scale and Third-scale Load Displacement Idealizations

Value	Full-scale*	Third-scale (measured)	Third-scale (expected)
F_{max} (kN)	356.2	41.2	39.6
F_u (kN)	267.1	30.9	29.7
EI_{eff} (kN/mm)	21.37	4.12	7.13
Δ_y (mm)	15.82	9.65	5.27
Δ_u (mm)	66.05	30.4	22
μ_Δ	4.17	3.15	4.17

**full-scale data shown is from M.A.Sc. Thesis by Shedid (2006)*

As described with the interpretation of the idealized values determined from Wall 1, the third-scale model shear wall did not reach the same level of ductility as the full-scale prototype wall tested by Shedid (2006). Once again this was attributed to the fact that the vertical reinforcing steel was more brittle than originally assumed and ruptured prior to the full development of compressive strength within the masonry.

The effective stiffness (EI_{eff}) measured through the load-displacement idealization was consistent with the stiffness scale factor found when the experimental load-displacement curves of the model and prototype were compared. The third-scale model had a lower stiffness than the full-scale prototype. As noted with Wall 1, this phenomenon could possibility be explained by the presence of unseen grout voids.

5.6 Conclusions

This chapter discussed the experimental results of the third-scale model reinforced shear wall specimens tested as the final component of this thesis. The shear wall specimens brought all of the individual material properties and characteristics discussed in Chapters 2 and 3 together into a complex composite material in order to observe the ability third-scale model masonry to replicate the behaviour of the full-scale prototype shear walls tested by Shedid (2006).

Both third-scale shear walls tested appeared to have a concentration of inelastic curvature in the bottom third of the wall heights. The displacement profile above this point was almost linear for each of the walls. This observation is consistent with the full-scale results obtained by Shedid (2006).

The experimentally measured curvature profiles for each of the third-scale shear walls was also consistent with the overall shape and magnitude of the curvature profiles resulting from the full-scale prototype walls. The measured curvatures were higher than the theoretically predicted values. This was consistent with the findings of Sasani and Kiureghian (2001).

Through the use of basic beam theory, and the equations described in Appendix C of this thesis, the ultimate capacity of the third-scale model shear walls was predicted with reasonable accuracy. However, the theoretical predictions were not as accurate with respect to the yield force, yield displacement or ultimate displacement. Based on the material properties described in Chapter 2, the stiffness of the third-scale model was expected to be greater than that of the full-scale walls (measured E_m was higher for model wall than prototype wall); however, the experimental results were not consistent with this fact. The experimentally measured stiffnesses were lower than the scaled full-scale results. A similar variation in stiffness was found in previous studies by Heine (1997) and Jamison (1997). Heine and Jamison both found that when comparing shear walls loaded monotonically to those loaded cyclically, the capacity of the walls was

consistent between the testing variation; however, the intial stiffnesses measured for similar shear walls tested using the two loading techniques did not provide consistant results (Heine, 1997).

The displacement ductility of the third-scale shear walls, defined using the ratio of ulimate displacement and yield displacement, was $\mu_\Delta = 4.16$ for Wall 1 and $\mu_\Delta = 2.74$ for Wall 2. As the amount of vertical steel increased, the ductility decreased. This trend was consistent with that found by Shing (1989) and Shedid (2006). The displacement ductility of the full-scale protoype walls tested by Shedid were $\mu_\Delta = 2.2$ and $\mu_\Delta = 2.0$ for the corresponding full-scale protoypes of Walls 1 and 2, respectively. Based on these experimentally determined results the third-scale model shear walls would appear to have experienced greater ductility than their full-scale prototype equivalents.

Apon the use a less conservative approach to define the displacement ductility through idealized yield and ultimate displacement intervals the displacement ductility values assigned the the third-scale model shear walls were refined. The idealization produced third-scale model displacement ductility values of $\mu_\Delta = 1.84$ and $\mu_\Delta = 3.15$ for Walls 1 and 2, respectively. The idealization produced full-scale prototype displacement ductility values of $\mu_\Delta = 2.95$ and $\mu_\Delta = 4.17$ for full-scale equivalents of Walls 1 and 2, respectively. The idealized displacement ductilty values had a better correlation to the load-displacement backbone curves and also remain consistent with the notion that the third-scale model specimens were limited to a less ductile behaviour due to the rupture of steel reinforcing prior to the full development of compressive strength of masonry.

6 CONCLUSIONS AND RECOMMENDATIONS

6.1 Summary

The overall goal of this thesis was to provide a detailed comparison between third-scale model and full-scale prototype masonry materials, assemblages and wall components. The study included a total of three phases of experimental testing. The first phase focused on the individual scaling of elements that make up a reinforced concrete masonry shear wall including blocks, grout, mortar, and reinforcing steel. The second phase of the research project focused on testing different configurations of masonry assemblages. Assemblages were selected and tested to represent components of shear walls designed to exhibit flexural failure. The third and final phase of research compared two third-scale model shear walls to full-scale prototype walls tested previously at McMaster University by Shedid (2006).

6.1.1 Constituent Materials

The non-structural material properties of the model block were modelled very well. The difference in densities between the third-scale model and full-scale prototype block tested by Long (2006) was negligible. There was a 13% reduction in the model blocks absorption capability when compared to the prototype. The compressive strength of the model blocks used throughout the research project was 54.2 MPa, over 100% stronger than the prototype blocks. The extremely high block strength was attributed to the presence of a super-plasticizer within the concrete block mix and the addition of a steel lip on the top of the block.

The impact of aggregate size on the compressive strength of mortar was negligible for both mixes using Type 10 (regular Portland) and Type 30 (high early-strength Portland) cement. However the use of Type 30 cement increased the average compressive strength of the mortar cubes by 25%.

The impact of aggregate size on the compressive strength of grout was clearly shown as an increasing trend as the aggregate size increased. In general, the compressive strengths of the model grout related very well to the full-scale fine grout prototype. There was only a 12% difference in strength between the model and prototype grout.

The model reinforcing steel showed a good material correlation to the full-scale prototype steel. The modulus of elasticity of the steel used for both horizontal and vertical reinforcing was approximately the same, 200 GPa. The tensile strength of the model vertical steel was approximately 8% stronger at yield and approximately 20% stronger at ultimate. The steel was not heat-treated as it had a similar stress-strain curve to the prototype steel (shown in Figure 2-28). In general, the model steel showed excellent correlation to the prototype vertical reinforcing up until approximately 10 times yield strain. As mentioned in Chapter 5, during the testing of the model shear wall specimens it was noticed that the steel was rupturing prematurely. It was concluded that the steel used as vertical reinforcing within the wall specimens was not representative of typical rebar found in full-scale walls as usually rebar will deform to over 10% elongation strain prior to rupture (CSA G30.18, 2009).

6.1.2 Assemblages

The ungrouted prisms tested under compressive loading produced a high compressive strength when compared to the prototype testing completed by Long (2006). The high compressive strength was attributed to the high block compressive strength. The fact that an analytical model developed by Koksal et al. (2005) was able to accurately predict the compressive strength of the ungrouted prisms using third-scale model properties provided reasonable confidence in the ability of the model assemblages to behave as direct models of full-scale assemblages.

The fact the Koksal's strength model could not produce accurate strength predictions for ungrouted masonry assemblages with varying mortar strengths emphasized the greater importance of mortar strength within reduced-scale models compared to full-scale assemblages. This finding was consistent with the trend noticed by Hamid et al. (1985) in a reduced-scale research program using quarter-scale masonry materials.

The model testing of grouted compressive assemblages illustrated the impact of grout strength on the compressive strength of the prism. As the compressive strength of the grout increased, the compressive strength of the grouted assemblage also increased. The strengths of the model grouted assemblages were higher than the prototypes tested by Drysdale and Hamid (1979). The high strengths of the model assemblages was again attributed to the use of a 54.2 MPa block instead of the 20 to 25 MPa block used in prototype testing. An analytical model developed by Priestly (1986) was used to relate the compressive strength of the third-scale units to full-scale prototypes. The mathematical model showed reasonable correlation indicating that if the model block strength had been more representative of the full-scale prototype block, the third-scale grouted assemblages would be produced comparable strengths to full-scale assemblages.

As the ungrouted shear triplet specimens were tested it was found that as the mortar strength was decreased by 48%, the corresponding shear strength of the assemblage was reduced by 44%. As mentioned previously with the compression prisms, the importance of masonry strength and mortar joint consistency is of significant importance when considering ungrouted model assemblages. This fact once again related well to the findings of Hamid et al. (1985).

The grouted shear triplet specimens were tested to compare the impact of grout splitting shear strength on the shear strength of the assemblages. As the splitting shear strength of grout increased by 9.5%, the shear strength of the

assemblages increased by 8.1%. The trend of increasing shear strength with respect to grout splitting strength was compared to previous reduced-scale testing by Abboud and Hamid (1987) and to full-scale prototype testing by Drysdale and Hamid (1979) with excellent correlation.

6.1.3 Shear Walls

The two model shear walls tested as part of this thesis replicated the ultimate capacity of the full-scale prototype walls quite well. The displacements measured for the third-scale model were higher than both the theoretical prediction based on simple flexural theory and the displacement results of the full-scale specimens tested by Shedid (2006). There were some difficulties comparing the stiffness at yield and loading conditions that were attributed to the use of monotonic loading technique in place of the cyclic loading used during the testing of the full-scale prototype shear walls. This finding was consistent with that observed by Heine (1997) and Jamison (1997) through the comparison of monotonic and cyclic testing procedures applied to shear walls.

The displacement ductility of the third-scale shear walls, defined using the ratio of ulimate displacement and yield displacement, was $\mu_\Delta = 4.16$ for Wall 1 and $\mu_\Delta = 2.74$ for Wall 2. As the amount of vertical steel increased, the ductility decreased. This trend was consistent with that found by Shing (1989) and Shedid (2006). The displacement ductility of the full-scale protoype walls tested by Shedid were $\mu_\Delta = 2.2$ and $\mu_\Delta = 2.0$ for the corresponding full-scale protoypes of Walls 1 and 2, respectively. Based on these experimentally determined results the third-scale model shear walls would appear to have experienced greater ductility than their full-scale prototype equivalents. This result was somewhat unexpected due to the lack of strength plateau within the model wall specimens.

An idealization technique defined by Tomazevic (1999) and Paulay & Priestley (1992) was used to relate compare the experimental third-scale model results to full-scale specimens. The experimentally measured ductility was then

redefined using the idealization technique. The idealization produced third-scale model displacement ductility values of $\mu_\Delta = 1.84$ and $\mu_\Delta = 3.15$ for Walls 1 and 2, respectively. The idealization produced full-scale prototype displacement ductility values of $\mu_\Delta = 2.95$ and $\mu_\Delta = 4.17$ for full-scale equivalents of Walls 1 and 2, respectively. The idealized displacement ductilty values had a better correlation to the load-displacement backbone curves and also remained consistent with the notion that the third-scale model specimens were limited to a less ductile behaviour due to the rupture of steel reinforcing prior to the full development of compressive strength of masonry.

6.2 Conclusions

The following conclusions are drawn from the preceding thesis project:

1. Excellent geometric similarity was found between the individual material properties and full-scale properties. This was largely due to the fact that the third-scale model blocks were created from a custom mould designed to be a perfect third-scale model of a typical 190 mm concrete block.

2. Even though the compressive strength of the third-scale model block used during this testing program was much higher than the prototype block, third-scale model prisms showed good correlation to analytical models developed by Priestley (1986) and Koksal et al. (2005) designed to predict the compressive strength of masonry using individual material properties of the assemblage. This fact suggested that a third-scale model block of similar strength to a full-scale prototype would have a comparable compressive strength.

3. The ability of the third-scale compression and shear assemblages to achieve similar strength characteristics as the prototype assemblages

tested by others clearly demonstrates the ability of third-scale masonry to act as a direct model for full-scale masonry testing.

4. The general behaviour of the flexural third-scale model shear walls including crack pattern, in-plane lateral displacements, strain profile, wall curvature, and load-deformation relationships showed good correlation with the full-scale prototypes until premature failure of the vertical reinforcement within the third-scale specimens.

5. The impact of testing the shear wall specimens under monotonic loading in place of the typical cyclic loading technique was that the model walls seemed to experience greater lateral displacements under comparable loading to the full-scale model.

6. Typically the small size effect of a structural model will allow for a detailed examination of the post-peak deformation of the load-displacement response (Long, 2006); however, in this case the premature rupturing of the vertical reinforcing steel prevented the model wall specimens from experiencing much strength degradation.

6.3 Recommendations for Future Research

The following areas are suggestions for future research to improve the use of third-scale model masonry to represent full-scale prototype structures:

1. A detailed sensitivity analysis should be performed on the concrete block mix used to produce third-scale masonry units in order to relate parameters such as cement content and type to overall compressive strength.

2. A thorough investigation of the impact of the ultimate strength of tensile steel on the ductility of shear walls should be performed in order to relate wall performance to material properties of reinforcing steel.

3. The monotonic push-over, described in this thesis to test model shear walls, should be compared to the fully reversed cyclic loading technique used by Shedid (2006) in order to verify the impact on the load-displacement backbone curve.

4. Now that the individual components of a reinforced masonry wall have been examined, the logical next step is to attempt to model more complex walls such as: shear walls with openings, walls with end confinement, etc. It would also be interesting to attempt to model the behaviour of a complete wall system in the form of a reduced-scale building.

REFERENCES

Abboud, B. E., Hamid, A. A., & Harris, H. G. (1990). Small-Scale Modeling of Concrete Block Masonry Structures. *ACI Structural Journal* , 145-155.

Assis, G., Hamid, A. A., & Harris, H. G. (1989). Material Models for Grouted Block Masonry . *Report No. 1.2 (a)-2, U.S.-Japan Coordinated Program on Masonry Building Research* .

ASTM International. (2007). *ASTM C404-07 - Standard Specification for Aggregates for Masonry Grout.* West Conshohocken, PA.

ASTM International. (2007). *ASTM C33-07 - Standard Specification for Concrete Aggregates.* West Conshohocken, PA.

ASTM International. (2008). *ASTM C109-08 - Standard Test Method for Compressive Strength of Hydraulic Cement Mortars.* West Conshohocken, PA.

ASTM International. (2008). *ASTM C1019-08 - Standard Test Method for Sampling and Testing Grout.* West Conshohocken, PA.

ASTM International. (2007). *ASTM C1006-07 - Standard Test Method for Splitting Tensile Strength of Masonry Units.* West Conshohocken, PA.

ASTM International. (2005). *ASTM E111-04 - Standard Test Method for Young's Modulus, Tangent Modulus, and Chord Modulus.* West Conshohocken, PA.

ASTM International. (2008). *ASTM C140-08 - Standard Test Methods for Sampling and Testing Concrete Masonry Units and Related Units.* West Conshohocken, PA.

Banting, B. R., Shedid, M. T., El-Dakhakhni, W. W., & Drysdale, R. G. (2009). Seismic Responce of End-confined Reinforced Concrete Block Shear Walls. *11th Canadian Masonry Symposium Proceedings.* Toronto, ON.

Banting, B., Heerema, P., & El-Dakhakhni, W. W. (2010). Production and Testing of ⅓ Scale Concrete Blocks. Submitted to the *8th International Masonry Conference Proceeding.* Dresden, Germany.

Bazant, Z. (1983). Crack band theory for fracture of concrete. *Materials and Structures,* Vol. 16 , 155-177.

Bazant, Z. P., & Chen, E.-P. (1996). Scaling of Structural Failure. *Sandia Report (SAND96-2948)* , 1-103.

Chopra, A. K. (2001). *Dynamics of Structures - Theory and Applications to Earthquake Engineering.* New Jersey: Pearson Education Inc.

Canadian Standards Association (CSA). (2009). *CSA G30.18-09 - Carbon steel bars for concrete reinforcement.* Toronto, ON.

Canadian Standards Association (CSA). (2004). *CSA S304.1-04 - Design of Masonry Structures.* Mississauga, ON.

Canadian Standards Association (CSA). (2009). *CSA 179-05 (R2009) - Mortar and Grout for Masonry Units.* Mississauga, ON.

Drysdale, R. G., & Hamid, A. A. (1979). Behaviour of Concrete Block Masonry Under Axial Compression. *American Concrete Institute Journal, Proceedings, Vol. 76, No.6* , 707-772.

Drysdale, R. G., & Hamid, A. A. (2005). *Masonry Structures - Behaviour and Design.* Canada: Canada Masonry Design Centre.

Elshafie, H., Hamid, A., & Nasr, E.-s. (2002). Strength and Stiffness of Masonry Shear Walls with Openings. *TMS Journal* , December 2002, 49-60.

Grimo, D. (2008, September 16). Personal communication at Niagara Block. (K. Hughes, Interviewer)

Hamid, A. A., & Abboud, B. E. (1986). Direct Modeling of Concrete Block Masonry Under Shear and In-Plane Tension. *ASTM Journal of Testing and Evaluation, Vol. 14, No. 2* , 112-121.

Hamid, A. A., Abboud, B. E., & Harris, H. G. (1985). Direct Modeling of Concrete Block Masonry Under Axial Compression. *ASTM STP 871 - Masonry: Research, Application and Problems* , 151-166.

Hamid, A. A., Drysdale, R. G., & Heidebrecht, A. C. (1979). Shear Strength of Concrete Masonry Joints. *Proc. 10th Int. Brick and Block Masonry Conference.* ASCE 105 (ST7), 1227-1240.

Hamid, A. A., El-Dakhakhni, W. W., Hakam, Z. H., & Mohamed, E. (2005). Behaviour of Composite Unreinforced Masonry-Fiber-Reinforced Polymer Wall Assemblages Under In-Plane Loading. *ASCE Journal of Composites for Construction* , 73-84.

Harris, H. G., & Sabnis, G. M. (1999). *Structural Modeling and Experimental Techniques, Second Edition.* Boca Raton: CRC Press LLC.

Heine, C. P. (1997). *Effect of Overturning Restraint on the Performance of Fully Sheathed and Perforated Timber Framed Shear Walls.* M.S. thesis, Blacksburg, Virginia: Virginia Polytechnic Institute and State University.

Jamison, J. B. (1997). *Monotonic and Cyclic Performance of Structurally Insulated Panel Shear Walls.* M.S. thesis, Blacksburg, Virginia: Virginia Polytechnic Institute and State University.

Janney, J. R., Breen, J. E., & Geymayer, H. (1970). Use of Models in Structural Engineering. *Models for Concrete Structures* , ACI SP-24, 1-18.

Johansen, V. C., Taylor, P. C., & Tennis, P. D. (2006). *Effect of Cement Characteristics on Concrete Properties.* Skokie, Illinois: Portland Cement Association.

Khalaf, F. M. (1989). The Performance of Concrete Blocks Loaded Parallel to the Bed Face. *The Masonry Society* , 20-25.

Koksal, H. O., Karakoc, C., & Yildrim, H. (2005). Compression Behaviour and Failure Mechanisms of Concrete Masonry Prisms. *ASCE Journal of Materials in Civil Engineering* , 107-115.

Langhaar, H. L. (1983). *Dimensional Analysis and Theory of Models.* Malabar, Florida, USA: Robert E. Krieger Publishing Company Inc.

Lefas, I. D., Kotsovos, M. D., & Ambraseys, N. (1990). Behaviour of Reinforced Concrete Structural Walls: Strength, Deformaton Characteristics, and Failure Mechansim. *ACI Structural Journal* , 23-31.

Long, L. (2006). *Behaviour of Half-Scale Reinforced Concrete Masonry Shear Walls.* M.A.Sc. thesis, Hamilton, Ontario: McMaster University.

Long, L., Hamid, A. A., & Drysdale, R. G. (2005). Small-scale Modelling of Concrete Masonry Using 1/2-scale units: A preliminary study. *10th Canadian Masonry Symposium Proceedings*, Banff, Alberta.

Mac, C. (2009). *Instruction Manual for Model 21 Block Plant.* Vancouver, Washinton: Columbia Machine, Inc.

Mitchell, D., Tremblay, R., Karacabeyli, E., Paultre, P., Saatcioglu, M., & Anderson, D. (2003). Seismic force modification factors for the proposed 2005 edition of the National Building Code of Canada. *Can. J. Civ. Eng. 30* , 308-327.

National Research Council of Canada (NRCC). (2005). *National Building Code of Canada, NBCC 2010.* Ottawa, ON.

Paulay, T., & Priestley, M. J. (1992). *Seismic Design of Reinforced Concrete and Masonry Buildings.* Toronto, ON: John Wiley & Sons, Inc.

Priestly, M. J. (1986). Seismic Design of Concrete Masonry Shear Walls. *ACI Journal* , 58-69.

Sasani, M., & Kiureghian, A. (February 2001). Seismic Fragility of RC Structural Wall: Displacement Approach. *ASCE Journal of Structural Engineering*, February 2001, 219-228.

Shedid, M. T., Drysdale, R. G., & El-Dakhakhni, W. (2009). Article in press: Behaviour of Fully Grouted Reinforced Masonry Shear Walls Failing in Flexure: Analysis. *Engineering Structures* (doi:10.1016/j.eng struct.2009.03.006).

Shedid, M. (2006). Ductility of Reinforced Concrete Masonry Shear Walls. *M.A.Sc. Thesis.* Hamilton, Ontario: McMaster University.

Shedid, M. T. (2009). Ductility of Concrete Block Shear Wall Structures. Ph.D. thesis, Hamilton, ON: McMaster Univsersity.

Shedid, M. T., Drysdale, R. G., & El-Dakhakhni, W. (2008). Behaviour of Fully Grouted Reinforced Concrete Masonry Shear Walls Failing in Flexure: Experimental Results. *Journal of Structural Engineering* , 1754-1767.

Shing, P. B., Noland, J. L., Klamerus, E., & Spaeh, H. (1989). Inelastic Behaviour of Concrete Masonry Shear Walls. *ASCE Journal of Structural Engineering* , 2204-2224.

Shing, P. B., Schuller, M., Hoskere, V. S., & Carter, E. (1990). Flexural and Shear Responce of Reinforced Masonry Walls. *ACI Structural Journal* , 647-656.

Szucs, E. (1980). *Similtude and Modelling.* New York: Elsevier Scientific Publishing Company.

Tomazevic, M. (1999). *Earthquake-Resistant Design of Masonry Buildings.* London, England: Imperial College Press.

Voon, K. C., & Ingham, J. M. (2006). Experimental In-Plane Shear Strength Investigation of Reinforced Concrete Masonry Walls. *ASCE Journal of Structural Engineering* , 400-409.

Wierzbicki, J. (2010). Behaviour of Reduced-scale Fully-grouted Concrete Block Shear Walls. Draft of M.A.Sc. thesis, Hamilton, ON: McMaster University.

APPENDIX A – Curvature and Strain Analysis

The following equations describe how average curvature values were measured during testing. As mentioned in Chapter 4 of this thesis, each shear wall was divided into segments. Each segment had a corresponding gauge length. The average strain was recorded for gauge length at increments of yield throughout testing on both the compression and tension ends of the wall specimens, as shown in figure below.

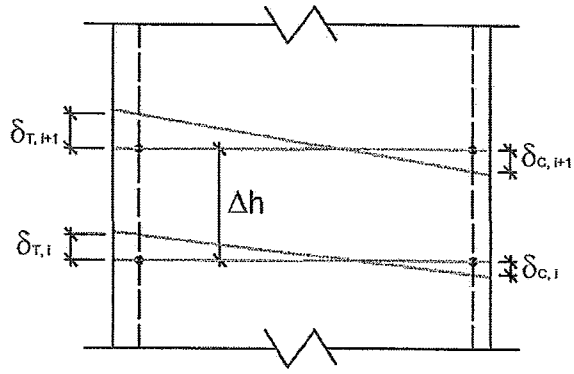

Net Compression and Tensile Strain Measurement over Gauge Length (Long, 2006)

$$\varepsilon_c = (\delta_{c,\,i+1} - \delta_{c,\,i}) / (\Delta_h); \qquad \text{and}$$

$$\varepsilon_t = (\delta_{t,\,i+1} - \delta_{t,\,i}) / (\Delta_h)$$

where;

δ_c = net displacement on compression end of wall

δ_t = net displacement on tension end of wall

ε_c = average compressive strain over gauge length

ε_t = average tensile strain over gauge length

Δ_h = gauge length (segment height)

The average curvature was then determined as shown in the following equation.

$$\varphi_i = (\varepsilon_{t,i} + \varepsilon_{c,i}) / l_w$$

where;

φ_i = average curvature over gauge length

$\varepsilon_{t,i}$ = net tensile strain over gauge length

$\varepsilon_{c,i}$ = net compressive strain over gauge length

The relationship between average curvature and net strain over various gauge lengths has been summarized in the following figure.

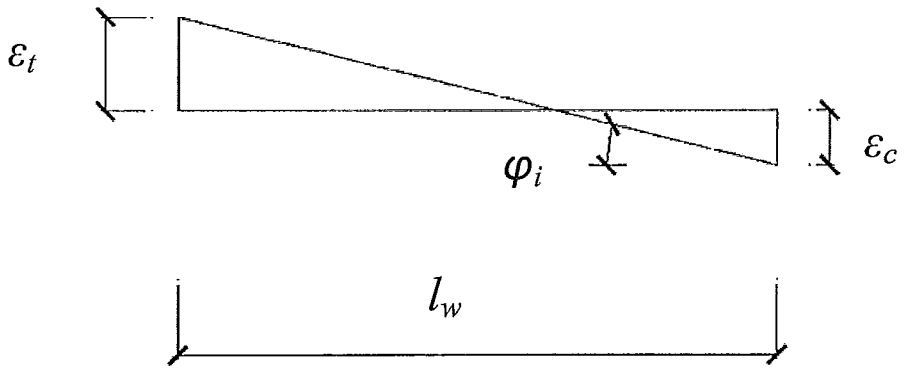

Curvature Calculation based on Strain Profile

APPENDIX B – Theoretical Wall Stiffness

The following equations were used to predict the theoretical stiffness value of the shear wall specimens discussed in Chapter 5.

$$K = \left\{ 1 \Big/ \left(\frac{h^3}{3 \cdot E_m \cdot I} + \frac{1.2 \cdot h}{G_m \cdot A} \right) \right\}$$

where;

K = elastic stiffness (N/mm)

h = height of wall (mm)

E_m = Elastic modulus of masonry (MPa)

I = Moment of inertia (mm^4)

G_m = 0.4 E_m for rectangular sections

The equation uses the elastic material properties of the wall cross-section to provide stiffness predictions. This elastic stiffness equation worked well in the prediction of the stiffness values for the full-scale wall specimens tested by Shedid (2006).

Wall 1 – Theoretical Stiffness Calculations

	ucracked			*cracked*	
	full-scale	1/3-scale		full-scale	1/3-scale
t (mm) =	190	63.3	t (mm) =	190	63.3
l_w (mm) =	1800	600	l_w (mm) =	1800	600
h (mm) =	3600	1200	h (mm) =	3600	1200
E_m (MPa) =	1.21E+04	1.91E+04	E_m (MPa) =	1.21E+04	1.91E+04
ybar (mm) =	900	300	Z (neutral axis, mm) =	493.72	124.94
f'_m (MPa) =	14.2	22.5	f'_m (MPa) =	14.2	22.5
A_b (mm^2) =	500	45	A_b (mm^2) =	500	45
I_g (neg steel, mm^4) =	92340000000	1.14E+09	n =	16.57	10.46
I_g (inc steel, mm^4) =	1.04796E+11	1.22E+09	I_{cr} (mm^4) =	2.76E+10	1.97E+08
G_m (MPa) =	4828	7650	G_m (MPa) =	4828	7650
A_m (mm^2) =	380925	40108.5	A_{cr} (mm^4) =	93806.93195	2848.5
K_G (N/mm) =	68287	33921	K_{cr} (N/mm) =	17807	4559

Wall 2 – Theoretical Stiffness Calculations

	ucracked			*cracked*	
	full-scale	1/3-scale		full-scale	1/3-scale
t (mm) =	190	63.3	t (mm) =	190	63.3
l_w (mm) =	1800	600	l_w (mm) =	1800	600
h (mm) =	3600	1200	h (mm) =	3600	1200
E_m (MPa) =	1.21E+04	1.91E+04	E_m (MPa) =	1.21E+04	1.91E+04
ybar (mm) =	900	300	Z (neutral axis, mm) =	618.52	156.05
f'_m (MPa) =	14.2	22.5	f'_m (MPa) =	14.2	22.5
A_b (mm^2) =	16.57	10.46	A_b (mm^2) =	500	45
I_g (neg steel, mm^4) =	92340000000	1.14E+09	n =	16.57	10.46
I_g (inc steel, mm^4) =	1.11024E+11	1.25E+09	I_{cr} (mm^4) =	4.06E+10	2.93E+08
G_m (MPa) =	4828	7650	G_m (MPa) =	4828	7650
A_m (mm^2) =	412065	41811.3	A_{cr} (mm^4) =	117519.5149	2848.5
K_G (N/mm) =	72585	35041	K_{cr} (N/mm) =	25406	5922

APPENDIX C – Predicted Experimental Results

All equations presented in this section are identical to those used by Shedid (2006) to predict the behaviour of the full-scale prototype shear walls that have been used to compare third-scale model behaviour throughout this experimental program. A summary of the predictions for each model shear wall specimen can be found in this section of the appendices.

The following equations, based on bending beam theory were used to predict the ultimate flexural strength of the test walls. Units (N and mm) are used for all of the following equations.

$$P = C_m + C_s - T_s$$

$$C_m = 0.85 f'_m \, t \, (0.8 \, c)$$

$$C_s = \sum A_s f'_s \quad ; \text{where } 0 \leq f'_s \leq f_y$$

$$\text{and} \quad f'_s = \frac{c - d_i}{c} \, 0.003 \, E_s < f_y$$

$$T_s = \sum A_s f_s \quad ; \text{where } 0 \leq f_s \leq f_y$$

$$\text{and} \quad f_s = \frac{d_i - c}{c} \, 0.003 \, E_s < f_y$$

$$M_u = C_m \left(\frac{l_w}{2} - 0.4c \right) + \sum A_s f_s \left(d_i - \frac{l_w}{2} \right)$$

where:

- d_i = Distance from the compression fibre to the centre of vertical steel reinforcement
- c = Distance from extreme compression fibre to neutral axis
- t = Thickness of wall
- l_w = Wall length
- P = Applied axial load (P = 0 N for both wall specimens)
- C_m = Compression force within masonry
- T_s = Tensile force in steel reinforcement

C_s = Compression force in steel reinforcement

f_y = Yield strength of vertical reinforcement

f_s = Tensile stress in vertical reinforcement

f'_s = Compressive stress in vertical reinforcement

f'_m = Average compressive strength of masonry

E_s = Modulus of elasticity for steel reinforcement

M_u = Moment resistance at maximum strain in masonry

A_s = Area of vertical reinforcement in the wall.

The lateral load and corresponding moment at theoretical yield point were determined using the following equations.

$$P = C_m + C_s - T_s$$

$$C_m = 0.5\, \varepsilon_m\, E_m\, t\, c$$

$$C_s = \sum A_s f'_s \quad ; \text{where } 0 \le f'_s \le f_y$$

$$T_s = \sum A_s f_s \quad ; \text{where } 0 \le f_s \le f_y$$

$$T_i = A_s \frac{d_i - c}{d_1 - c} f_y$$

$$\varepsilon_m = \varepsilon_y\, c\, /\, (d\text{-}c)$$

$$M_y = C_m\left(\frac{l_w}{2} - 0.33c\right) + \sum A_s f_s\left(d_i - \frac{l_w}{2}\right) + \sum A_s f'_s\left(\frac{l_w}{2} - d_i\right)$$

where:

ε_m = Compressive strain in the extreme masonry fibre

E_m = Modulus of elasticity of masonry

ε_y = Yield strain of the outermost reinforcing bar in tension

d_1 = distance from extreme compression fibre to first bar

The following equations were used to verify the shear capacity of the shear wall specimens. The shear resistance of the wall specimens was required to exceed the maximum applied lateral shear so as to ensure flexural behaviour. The following equations are from CSA S304.1-04.

$$V_u^S = V_{steel} + V_{masonry}$$

$$V_{steel} = 0.6 f_y A_h \left(\frac{0.8\, l_w}{S_h}\right)$$

$$V_{masonry} = \left(0.16\sqrt{f'm} + 0.25\frac{P}{A_g}\right) t\,(0.8 l_w)$$

where:

V_u^S	=	Shear strength of masonry wall
V_{steel}	=	Shear strength of wall provided by horizontal steel
V_{mas}	=	Shear strength of wall provided by the masonry
P	=	Applied axial load on the wall
f'_m	=	Average compressive strengths of four-course prism
A_g	=	Horizontal cross section area of wall
S_h	=	Vertical spacing between horizontal reinforcement
A_h	=	Area of horizontal reinforcement in cross-section
f_y	=	Yield strength of horizontal reinforcement
t	=	Thickness of wall
l_w	=	Wall length

The following equations were used to predict the theoretical displacements, curvatures and ductility of the model masonry shear walls (Drysdale and Hamid, 2005). Predictions related to each wall specimen can be found later in the appendices.

$$V_y = \frac{M_y}{h_w}$$

$$\varphi_y = \frac{d_1 - c_y}{\varepsilon_y}$$

$$\theta_y = \varphi_y \frac{h_w}{2}$$

$$\Delta_y = \varphi_y \frac{h_w^2}{3} = \theta_y \frac{2}{3} h_w \quad ; \quad \text{then \% Drift}_y = \frac{\Delta_y}{h_w} \text{ x } 100$$

$$V_u = \frac{M_u}{h_w}$$

$$\varphi_u = \frac{c_u}{\varepsilon_m}$$

$$\theta_p = \varphi_p \, l_p \; ; \quad \text{where } \varphi_p = \varphi_u - \varphi_y$$

$$\Delta_p = \theta_p \, (h_w - 0.5 \, l_p)$$

$$\Delta_u = \Delta_y + \Delta_p \quad , \text{ then \% Drift}_u = \frac{\Delta_u}{h_w} \text{ x } 100$$

$$\mu_\varphi = \frac{\varphi_u}{\varphi_y}$$

$$\mu_\Delta = \frac{\Delta_u}{\Delta_y} = 1 + \frac{\Delta_p}{\Delta_y} = 1 + 3(\mu_\varphi - 1)\frac{l_p}{h_w}\left(1 - 0.5\frac{l_p}{h_w}\right)$$

$$R_d = \frac{\Delta_u}{\Delta_y}$$

where:

d_1 = distance from extreme compression fibre to first bar

ε_y = yield strain of steel reinforcement

ε_m = Maximum compressive strain in masonry

c_y = Length of compression zone at first yield of reinforcement

c_u = Length of compression zone at maximum load

M_y = Moment resistance at first yield of reinforcement

V_y = Lateral load resistance at first yield of reinforcement

M_u = Moment resistance at maximum strain in masonry

V_u = Lateral load resistance at maximum strain in masonry

φ_y = Curvature at wall base at first yield of reinforcement

φ_u = Curvature at wall base at maximum strain in masonry

θ_y = Rotation of the wall at first yield of reinforcement

θ_p = Plastic rotation of the wall

Δ_y = Lateral displacement of wall at first yield of reinforcement

Δ_p = Plastic displacement of wall

Δ_u = Maximum Lateral displacement of wall

μ_φ = Curvature ductility

μ_Δ = Displacement ductility

l_w = Wall length

l_p = Equivalent plastic hinge length

R_d = Ductility Related Force Modification Factor

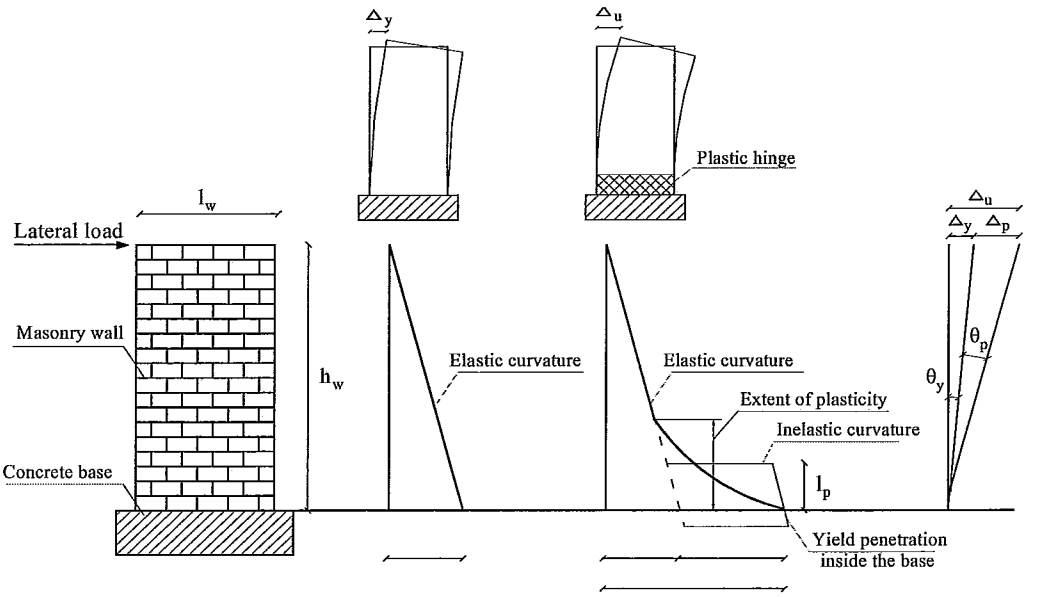

Elastic and Inelastic Displacements and Curvatures from (Shedid, 2006)

The following tables present a summary of the theoretical predictions of the model shear wall experimental results. There are two sets of predictions for each shear wall depending on the assumed plastic hinge (h_p) length. CSA S304.1 currently recognizes two ductility levels of masonry shear walls: the limited ductility shear wall assumes $h_p = l_w/2$ and a moderately ductile shear wall assumes a plastic hinge length $h_p = l_w$. The predictions from both ductility levels have been presented for comparison purposes.

Summary of Expected Experimental Results for Wall 1 - Ltd. Ductilty				
		W1	W1**	
Percentage Vertical Steel	ρ_v	0.60	0.60	%
Ultimate Moment Resistance	M_u	32.42	31.40	kN*m
Lateral Load at Ultimate Moment	V_u	27.02	26.17	kN
Shear Resistance (S304.1-04)	V_r	40.04	35.62	kN
SHEAR CAPACITY CHECK		OK	OK	
Seismic (ult.) Moment Resistance	$M_{u,s}$	32.15	31.09	kN*m
Lateral Load at Seis (ult.) Moment	$V_{u,s}$	26.79	25.91	kN
Yield Moment Resistance*	M_y	22.23	23.38	kN*m
Lateral Load at Yield Moment*	V_y	18.53	19.49	kN
Limited Ductility ($h_p = l_w/2$) [Rd = 1.5], masonry strain = 0.0025				
Assumed Plastic Hinge Location	h_p	295	295	mm
Yield Curvature*	ϕ_y	6.09E-06	6.16E-06	
Ultimate Curvature	ϕ_u	2.99E-05	2.73E-05	
Lateral Displacement at first yield*	Δ_y	2.92	2.96	mm
Plastic Displacement of Wall	Δ_p	7.39	6.55	mm
Maximum Lateral Displacement	Δ_u	10.32	9.50	mm
Curvature Ductility	μ_ϕ	4.91	4.43	
Displacement Ductility	μ_Δ	3.53	3.22	
Percent Drift at first yield*	D_y%	0.244	0.246	%
Percent Drift at Ultimate	D_u%	0.860	0.792	%
Force Modification Factor	R_d	3.529	3.216	
Limited Ductility ($h_p = l_w/2$) [Rd = 1.5], masonry strain = 0.003				
Assumed Plastic Hinge Location	h_p	295	295	mm
Yield Curvature*	ϕ_y	6.09E-06	6.16E-06	
Ultimate Curvature	ϕ_u	3.63E-05	3.15E-05	
Lateral Displacement at first yield*	Δ_y	2.92	2.96	mm
Plastic Displacement of Wall	Δ_p	9.38	7.88	mm
Maximum Lateral Displacement	Δ_u	12.30	10.83	mm
Curvature Ductility	μ_ϕ	5.96	5.12	
Displacement Ductility	μ_Δ	4.21	3.67	
Percent Drift at first yield*	D_y%	0.244	0.246	%
Percent Drift at Ultimate	D_u%	1.025	0.903	%
Force Modification Factor	R_d	4.21	3.67	
**always includes compression steel*				
***excluding compression steel in calculations*				

Summary of Expected Experimental Results for Wall 1 - Mod. Ductility				
		W1	W1**	
Percentage Vertical Steel	ρ_v	0.60	0.60	%
Ultimate Moment Resistance	M_u	32.42	31.40	kN*m
Lateral Load at Ultimate Moment	V_u	27.02	26.17	kN
Shear Resistance (S304.1-04)	V_r	40.04	35.62	kN
SHEAR CAPACITY CHECK		OK	OK	
Seismic (ult.) Moment Resistance	$M_{u,s}$	32.15	31.09	kN*m
Lateral Load at Seis (ult.) Moment	$V_{u,s}$	26.79	25.91	kN
Yield Moment Resistance*	M_y	22.23	23.38	kN*m
Lateral Load at Yield Moment*	V_y	18.53	19.49	kN
Moderate Ductility ($h_p = l_w$) [Rd = 2.0], masonry strain = 0.0025				
Assumed Plastic Hinge Location	h_p	590	590	mm
Yield Curvature*	ϕ_y	6.09E-06	6.16E-06	
Ultimate Curvature	ϕ_u	2.99E-05	2.73E-05	
Lateral Displacement at first yield*	Δ_y	2.92	2.96	mm
Plastic Displacement of Wall	Δ_p	12.71	11.26	mm
Maximum Lateral Displacement	Δ_u	15.64	14.22	mm
Curvature Ductility	μ_ϕ	4.91	4.43	
Displacement Ductility	μ_Δ	5.35	4.81	
Percent Drift at first yield*	$D_y\%$	0.244	0.246	%
Percent Drift at Ultimate	$D_u\%$	1.303	1.185	%
Force Modification Factor	R_d	5.349	4.811	
Moderate Ductility ($h_p = l_w$) [Rd = 2.0], masonry strain = 0.003				
Assumed Plastic Hinge Location	h_p	590	590	mm
Yield Curvature*	ϕ_y	6.09E-06	6.16E-06	
Ultimate Curvature	ϕ_u	3.63E-05	3.15E-05	
Lateral Displacement at first yield*	Δ_y	2.92	2.96	mm
Plastic Displacement of Wall	Δ_p	16.13	13.55	mm
Maximum Lateral Displacement	Δ_u	19.05	16.50	mm
Curvature Ductility	μ_ϕ	5.96	5.12	
Displacement Ductility	μ_Δ	6.52	5.58	
Percent Drift at first yield*	$D_y\%$	0.244	0.246	%
Percent Drift at Ultimate	$D_u\%$	1.587	1.375	%
Force Modification Factor	R_d	6.52	5.58	
always includes compression steel				
****excluding compression steel in calculations***				

Summary of Expected Experimental Results for Wall 2 - Ltd. Ductility				
		W2	W2**	
Percentage Vertical Steel	ρ_v	1.08	1.08	%
Ultimate Moment Resistance	M_u	51.54	49.06	kN*m
Lateral Load at Ultimate Moment	V_u	42.95	40.88	kN
Shear Resistance (S304.1-04)	V_r	47.92	47.92	kN
SHEAR CAPACITY CHECK		OK	OK	
Seismic (ult.) Moment Resistance	$M_{u,s}$	48.71	48.60	kN*m
Lateral Load at Seis (ult.) Moment	$V_{u,s}$	40.59	40.50	kN
Yield Moment Resistance*	M_y	37.83	38.91	kN*m
Lateral Load at Yield Moment*	V_y	31.52	32.42	kN
Limited Ductility ($h_p = l_w/2$) [Rd = 1.5], Masonry strain = 0.0025				
Assumed Plastic Hinge Location	h_p	295	295	mm
Yield Curvature*	ϕ_y	5.92E-06	5.94E-06	
Ultimate Curvature	ϕ_u	1.96E-05	1.77E-05	
Lateral Displacement at first yield*	Δ_y	2.84	2.85	mm
Plastic Displacement of Wall	Δ_p	4.25	3.65	mm
Maximum Lateral Displacement	Δ_u	7.09	6.51	mm
Curvature Ductility	μ_ϕ	3.32	2.98	
Displacement Ductility	μ_Δ	2.50	2.28	
Percent Drift at first yield*	D_y%	0.237	0.238	%
Percent Drift at Ultimate	D_u%	0.591	0.542	%
Force Modification Factor	R_d	2.498	2.281	
Limited Ductility ($h_p = l_w/2$) [Rd = 1.5], Masonry strain = 0.003				
Assumed Plastic Hinge Location	h_p	295	295	mm
Yield Curvature*	ϕ_y	5.92E-06	5.94E-06	
Ultimate Curvature	ϕ_u	2.34E-05	2.07E-05	
Lateral Displacement at first yield*	Δ_y	2.84	2.85	mm
Plastic Displacement of Wall	Δ_p	5.44	4.58	mm
Maximum Lateral Displacement	Δ_u	8.28	7.43	mm
Curvature Ductility	μ_ϕ	3.96	3.48	
Displacement Ductility	μ_Δ	2.92	2.60	
Percent Drift at first yield*	D_y%	0.237	0.238	%
Percent Drift at Ultimate	D_u%	0.690	0.619	%
Force Modification Factor	R_d	2.916	2.605	
always includes compression steel				
****excluding compression steel in calculations***				

Summary of Expected Experimental Results for Wall 2 - Mod. Ductility				
		W2	W2**	
Percentage Vertical Steel	ρ_v	1.08	1.08	%
Ultimate Moment Resistance	M_u	51.54	49.06	kN*m
Lateral Load at Ultimate Moment	V_u	42.95	40.88	kN
Shear Resistance (S304.1-04)	V_r	47.92	47.92	kN
SHEAR CAPACITY CHECK		OK	OK	
Seismic (ult.) Moment Resistance	$M_{u,s}$	48.71	48.60	kN*m
Lateral Load at Seis (ult.) Moment	$V_{u,s}$	40.59	40.50	kN
Yield Moment Resistance*	M_y	37.83	38.91	kN*m
Lateral Load at Yield Moment*	V_y	31.52	32.42	kN
Moderate Ductility ($h_p = l_w$) [Rd = 2.0], Masonry strain = 0.0025				
Assumed Plastic Hinge Location	h_p	590	590	mm
Yield Curvature*	ϕ_y	5.92E-06	5.94E-06	
Ultimate Curvature	ϕ_u	1.96E-05	1.77E-05	
Lateral Displacement at first yield*	Δ_y	2.84	2.85	mm
Plastic Displacement of Wall	Δ_p	7.32	6.28	mm
Maximum Lateral Displacement	Δ_u	10.16	9.14	mm
Curvature Ductility	μ_ϕ	3.32	2.98	
Displacement Ductility	μ_Δ	3.58	3.20	
Percent Drift at first yield*	D_y%	0.237	0.238	%
Percent Drift at Ultimate	D_u%	0.846	0.761	%
Force Modification Factor	R_d	3.577	3.203	
Moderate Ductility ($h_p = l_w$) [Rd = 2.0], Masonry strain = 0.003				
Assumed Plastic Hinge Location	h_p	590	590	mm
Yield Curvature*	ϕ_y	5.92E-06	5.94E-06	
Ultimate Curvature	ϕ_u	2.34E-05	2.07E-05	
Lateral Displacement at first yield*	Δ_y	2.84	2.85	mm
Plastic Displacement of Wall	Δ_p	9.36	7.87	mm
Maximum Lateral Displacement	Δ_u	12.20	10.72	mm
Curvature Ductility	μ_ϕ	3.96	3.48	
Displacement Ductility	μ_Δ	4.29	3.76	
Percent Drift at first yield*	D_y%	0.237	0.238	%
Percent Drift at Ultimate	D_u%	1.016	0.894	%
Force Modification Factor	R_d	4.295	3.760	
always includes compression steel				
****excluding compression steel in calculations***				

APPENDIX D – Shear Wall Material Properties

The following appendix presents a summary of all the testing results for the mortar cubes, grout cylinder and prisms used to establish the material properties of the third-scale model shear wall specimens. As mentioned previously in Chapter 4, the construction of the shear wall specimens was completed over a total of three days. All specimens listed in this section of the appendices have been labelled with a 1, 2, or 3 to indicate the day of construction.

Results from Mortar Cubes Testing

	Date	Date	Age	Load at Failure					
Specimen	Created	Tested	at Test	(kN)	(N)	Area (mm^2)	Stress (MPa)		
1-1-1	18-Nov-08	30-Jan-09	73	68.2	68200	2580	26.43		
1-1-2	18-Nov-08	30-Jan-09	73	68.4	68400	2580	26.51		
1-1-3	18-Nov-08	30-Jan-09	73	64	64000	2580	24.81	25.92	
1-2-1	18-Nov-08	30-Jan-09	73	83.7	83700	2580	32.44		
1-2-2	18-Nov-08	30-Jan-09	73	72.7	72700	2580	28.18		28.65
1-2-3	18-Nov-08	28-Jan-09	71	79	79000	2580	30.62	30.41	
1-3-1	18-Nov-08	28-Jan-09	71	75.1	75100	2580	29.11		
1-3-2	18-Nov-08	28-Jan-09	71	78.8	78800	2580	30.54		
1-3-3	18-Nov-08	28-Jan-09	71	75.4	75400	2580	29.22	29.62	
2-1-1	19-Nov-08	28-Jan-09	70	66.4	66400	2580	25.74		
2-1-2	19-Nov-08	28-Jan-09	70	66.2	66200	2580	25.66		
2-1-3	19-Nov-08	28-Jan-09	70	69.4	69400	2580	26.9	26.1	
2-2-1	19-Nov-08	30-Jan-09	72	75.7	75700	2580	29.3		
2-2-2	19-Nov-08	28-Jan-09	70	68.3	68300	2580	26.47		26.98
2-2-3	19-Nov-08	28-Jan-09	70	72.4	72400	2580	28.06	27.94	
2-3-1	19-Nov-08	30-Jan-09	72	73.7	73700	2580	28.57		
2-3-2	19-Nov-08	28-Jan-09	70	62.5	62500	2580	24.22		
2-3-3	19-Nov-08	28-Jan-09	70	72.1	72100	2580	27.95	26.91	
3-1-1	20-Nov-08	20-Jan-09	61	86.3	86300	2580	33.45		
3-1-2	20-Nov-08	28-Jan-09	69	87.3	87300	2580	33.84		
3-1-3	20-Nov-08	28-Jan-09	69	92.4	92400	2580	35.81	34.37	
3-2-1	20-Nov-08	28-Jan-09	69	78.4	78400	2580	30.39		
3-2-2	20-Nov-08	28-Jan-09	69	74.3	74300	2580	28.8		32.07
3-2-3	20-Nov-08	28-Jan-09	69	78.7	78700	2580	30.5	29.9	
3-3-1	20-Nov-08	28-Jan-09	69	82.6	82600	2580	32.02		
3-3-2	20-Nov-08	28-Jan-09	69	81.2	81200	2580	31.47		
3-3-3	20-Nov-08	28-Jan-09	69	83.4	83400	2580	32.33	31.94	

Results from Grout Cylinder Testing

	Load at Failure				
Specimen	(kip)	(N)	Area (mm^2)	Stress (MPa)	Average (MPa)
G1-1	40	177928	7854	22.65	
G1-2	35.25	156799.05	7854	19.96	
G1-3	38	169031.6	7854	21.52	21.4
G2-1	29	128997.8	7854	16.42	
G2-2	29.5	131221.9	7854	16.71	
G2-3	30	133446	7854	16.99	16.7
G3-1	30.75	136782.15	7854	17.42	
G3-2	27.5	122325.5	7854	15.57	
G3-3	28.75	127885.75	7854	16.28	16.4

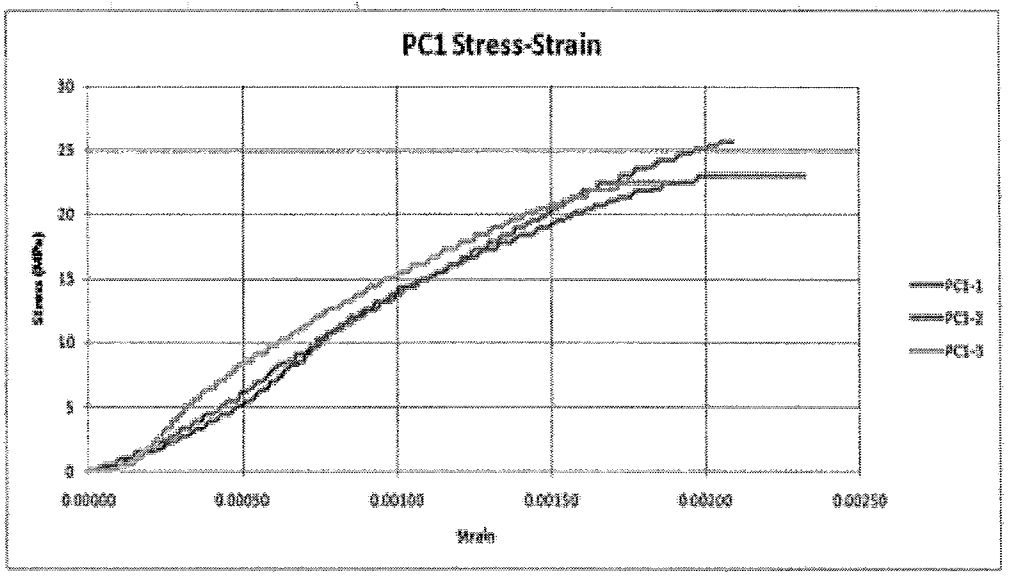

			measured	code	
	f'm (MPa)	$\varepsilon_{m,max}$	Em (MPa)	Em (MPa)	% difference
PC1-1	25.72	0.00209	15640	21862	28.46%
PC1-2	23.1	0.00232	17313	19635	11.83%
PC1-3	22.51	0.00188	17884	19133.5	6.53%
average	**23.78**	**0.00210**	**16946**	**20210**	**15.61%**
C.O.V. (%)	**7.19%**	**10.48%**	**6.88%**	**7.19%**	--

Stress-strain summary of construction prisms from day 1

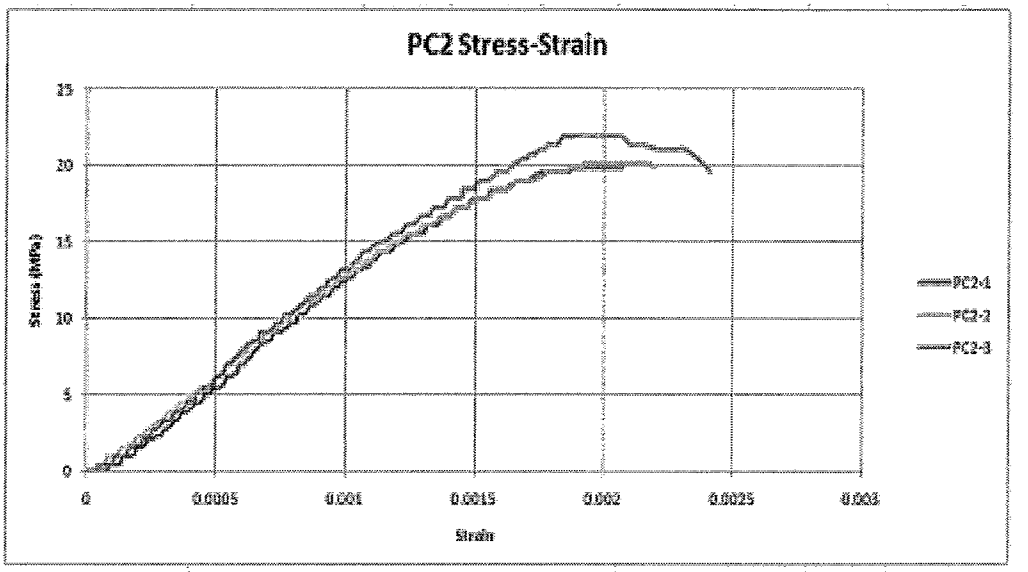

			measured	code	
	f'm (MPa)	$\varepsilon_{m,max}$	Em (MPa)	Em (MPa)	% difference
PC2-1	19.9	0.00207	14474	16915	14.43%
PC2-2	20.18	0.00219	13609	17153	20.66%
PC2-3	21.97	0.00241	15258	18674.5	18.30%
average	**20.68**	**0.00222**	**14447**	**17581**	**17.80%**
C.O.V. (%)	**5.43%**	**7.77%**	**5.71%**	**5.43%**	--

Stress-strain summary of construction prisms from day 2

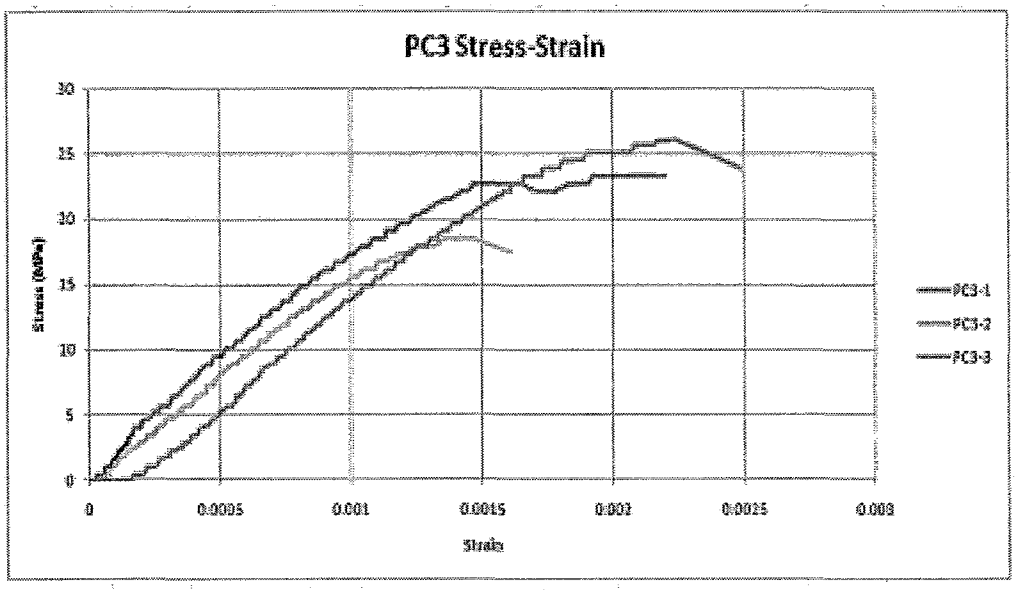

			measured	code	
	f'm (MPa)	$\varepsilon_{m,max}$	Em (MPa)	Em (MPa)	% difference
PC3-1	23.34	0.0022	18027	19839	9.13%
PC3-2	18.54	0.00161	16505	15759	4.73%
PC3-3	26.05	0.00249	18168	22142.5	17.95%
average	**22.64**	**0.0021**	**17567**	**19247**	**10.61%**
C.O.V. (%)	**16.80%**	**21.35%**	**5.25%**	**16.80%**	--

Stress-strain summary of construction prism from day 3